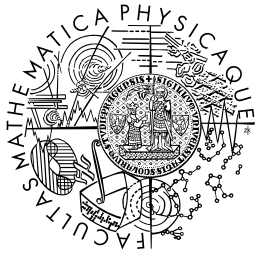

FACULTY
OF MATHEMATICS
AND PHYSICS
Charles University

DOCTORAL THESIS

Tomáš Kosek

Analysis of data from heavy-ion collisions at the ATLAS experiment

Institute of Particle and Nuclear Physics

Supervisor of the doctoral thesis:	doc. RNDr. Jiří Dolejší, CSc.
Study programme:	Subnuclear Physics
Study branch:	Physics

Prague 2018

I declare that I carried out this doctoral thesis independently, and only with the cited sources, literature and other professional sources.

I understand that my work relates to the rights and obligations under the Act No. 121/2000 Sb., the Copyright Act, as amended, in particular the fact that the Charles University has the right to conclude a license agreement on the use of this work as a school work pursuant to Section 60 subsection 1 of the Copyright Act.

In Prague 1st of August 2018 signature of the author

Title: Analysis of data from heavy-ion collisions at the ATLAS experiment

Author: Tomáš Kosek

Department: Institute of Particle and Nuclear Physics

Supervisor: doc. RNDr. Jiří Dolejší, CSc., Institute of Particle and Nuclear Physics

Abstract: Experimental study of high energy heavy-ion collisions is of great interest because of the possible formation of the new form of matter, quark gluon plasma (QGP). The QGP formation is difficult to prove due to the very short timescales at which heavy-ion collisions take place but there are several phenomena that suggest the QGP is created in HI collisions. One of these is the so called jet quenching which in general describes the set of modifications that jets produced in heavy-ion collisions undergo due to the interaction with medium created in the collision. The measurement of jets and their properties in heavy-ion collisions is difficult due to the large underlying event background and fluctuations present in Pb+Pb collisions. This thesis presents the reconstruction steps that allow ATLAS experiment at the LHC to publish high precision measurements of jet properties in Pb+Pb collisions. One of these is the measurement of jet fragmentation in pp and Pb+Pb collisions at $\sqrt{s_{\mathrm{NN}}} = 2.76\,\mathrm{TeV}$. Significant modifications of jet fragmentation in Pb+Pb collisions are observed.

Keywords: QGP, heavy-ion, jet quenching

I would like to thank my supervisor doc. RNDr. Jiří Dolejší, CSc. for his patient guidance and encouragement during my master and doctoral studies. I am also very grateful to my consultant doc. Mgr. Martin Spousta, Ph.D. for his advisory, support and assistance during the years I spent working at the ATLAS experiment. I would also like to extend my thanks to my classmates and collaborators, namely to Radim Slovák, Martin Rybář and Petr Balek and to the colleagues from my home institute for the friendly and inspiring environment they created.

Finally, I wish to thank my family for their support and encouragement throughout my study.

Contents

1. Introduction

Sixteen years ago, when the Relativistic Heavy Ion Collider (RHIC) started it's operation, the new era of the heavy-ion physics has begun. Experiments at RHIC were first that published observations of the exciting phenomena like jet quenching, elliptic flow and others. The supply of new experimental results was then accelerated with the start of the operation of the Large Hadron Collider (LHC) that, apart from it's main *pp* physics program, started colliding lead nuclei in November 2010 at the before unseen TeV scale.[1] The flood of new experimental observations naturally stimulated the development of the theoretical ideas and models that attempt to describe the underlying physics.

The main goal of the heavy-ion community is to study properties of the new form of matter created in HI collisions called quark gluon plasma (QGP). QGP is thought of as a state of matter, where quarks and gluons are deconfined from hadrons making it a matter analogous to the plasma that we know for example from lightnings, tokamaks or solar corona. The fundamental difference from standard electromagnetic plasma is that the behavior of quarks and gluons in QGP is determined entirely by the strong interaction that in usual conditions governs quarks and gluons to be confined in hadrons. The fundamental theory that attempts to describe the strong interaction is the quantum chromodynamics (QCD) which is a quantum field theory invariant under SU(3) gauge group. By studying the properties of the QGP we are able to study properties of the QCD at finite temperature which is of great interest from the theoretical point of view. Last but not least, it is supposed that the Universe was in the state of QGP shortly after Big Bang and so the results of heavy-ion physics program may have astrophysical implications.

It is supposed that QGP is created in ultrarelativistic heavy-ion collisions, where an extreme energy density and temperature are reached in the microscopical volume where two nuclei collide. It is in fact the only possibility how to create and access the QGP in the laboratory. Prove the existence of QGP and study its properties is however not a straightforward task since the QGP created in heavy-ion collisions is not accessible directly because of the very short timescales (at the level of femtometre/c) at which it exists. There are however signatures and probes, suggested by theorists and phenomenologists, that confirm the existence of QGP and enable to study it experimentally.

One of the signatures of QGP is the so called jet quenching, a phenomenon first indirectly observed in production of highest p_{T} particles by experiments at RHIC that was later confirmed by experiments at LHC by the observation of the production of asymmetric dijet pairs that have highly imbalanced transverse momentum. The nowadays picture of the jet quenching is that highly energetic partons, that are created in the hard scattering in heavy-ion collision, has to traverse through the hot and dense medium (QGP). This causes them to lose energy by medium-induced gluon radiation and elastic scatterings. Since the jets we measure in the detector in fact originate from these partons, the reconstructed jet energy and the other properties of jets are modified. To gain as much information

[1] The gold nuclei at RHIC were collided at the center of mass energy $\sqrt{s_{\mathrm{AuAu}}} = 200\,\mathrm{GeV}$, the lead nuclei at the LHC were collided at $\sqrt{s_{\mathrm{PbPb}}} = 2.76\,\mathrm{TeV}$.

about jet quenching as possible, the dijet asymmetry measurement was followed by several other measurements that helped to improve the understanding of the jet quenching. One of these measurements is a measurement of jet fragmentation functions in Pb+Pb collisions that will be one of the main subjects of this thesis.

In the first chapter of this thesis, general aspects and basic terms connected with the heavy-ion collisions will be described. In the second chapter, the basics of QCD are briefly summarized, then the properties of the QGP and its experimental signatures will be reviewed and some of the experimental observations of these signatures will be shown. Technical details of the ATLAS experiment and the jet reconstruction in heavy-ion collisions will be briefly described in two following chapters. Last chapters are devoted to the details of the measurement of the jet fragmentation functions and to the summary.

Statement of the author about his contributions

Every paper or the conference contribution presented by the LHC experiments is the result of the collaborative work of hundreds of people. The following text is aimed to clarify the author's contributions to the results presented in this thesis.

The results of the author's own work are presented in chapters related to the jet reconstruction in heavy-ion collisions and the measurement of jet fragmentation functions (chapters 5 and 6). With regard to the jet reconstruction author's main contribution was the derivation of the MC based jet calibration for heavy-ion jets. This was a long and tedious work that required tens of iterations to reach the sufficient performance. This calibration was derived in four versions depending on the collision system and centre-of-mass energy – *pp* and Pb+Pb data at 2.76 TeV, *p*+Pb data at 5.02 TeV and *pp* data at 8 TeV. It was important component of approximately eight published jet analyses that utilized these data.

Author's work connected to the jet reconstruction and performance continued with the study of Z+jet events in *pp* collisions at 8 TeV where the transverse momentum balance and the differences between heavy-ion and *pp* algorithm reconstructed jets were studied. This analysis was aimed to check the robustness of the cross-calibration procedure that is also briefly described in chapter 5. This procedure allowed heavy-ion group at ATLAS experiment to reach very good precision of the jet measurements and to derive reliable and robust jet energy scale uncertainties. Not to impersonate someone else's work the parts of the jet reconstruction and cross-calibration procedure that are not author's work are described rather minimalistically and are correctly cited.

The main physical result of the author is the analysis of the jet fragmentation functions in Pb+Pb and *pp* collisions which was done in fruitful collaboration with Dr. Radim Slovák. Author's work was to implement things related to the unfolding into the main analysis framework, tune and check the performance of the unfolding and do the offline processing of the data that Dr. Slovak produced. This included the unfolding procedure, checking the performance of the whole analysis chain and at the very end production of the final plots (except the plots in Figure 6.16 that Dr. Slovak made). When deriving systematic uncertainties author's work was again to repeat the offline processing, calculate the size of the various systematic uncertainty components and to combine them into the final systematic uncertainty. As for the jet reconstruction, to clarify which parts of the

analysis are not author's work (i.e. are Dr. Slovak's work) they are only briefly described and Dr. Slovak's phd thesis is cited.

The conference note (public document with preliminary results) about the performance of jet reconstruction using the ATLAS heavy ion jet algorithm was made available online in April 2015. The preliminary results of the analysis of the jet fragmentation functions were presented by the author of this thesis at the Quark Matter Conference in October 2015 in Kobe, Japan and in June 2016 at the LHCP Conference in Lund, Sweden. The final results were published as a paper in the European Physical Journal C in February 2017 [1].

2. Heavy-Ion Collisions

In this chapter, we will briefly describe the general aspects of ultra-relativistic heavy-ion collisions.

2.1 Geometry of collision and Glauber model

When two nuclei collide, the size and shape of the overlap region is of great importance as it determines the size and shape of the initial stage of the hot and dense medium created in the collision. The variable that determines the geometry of the collision is the so called impact parameter, usually denoted b, that expresses the distance between the centres of the nuclei in the transverse plane which is the plane perpendicular to the momentum vector of the nuclei before collision, see Figure 2.1 (in the right part of this Figure, the transverse plane is defined by x and y axis). The nucleons that undergo at least one inelastic interaction with the counterparts from the other nuclei are called participants, the nucleons that do not interact are called spectators. The plane defined by the impact parameter and the z axis is called the reaction plane. The number of participating nucleons, N_{part}, and spectating nucleons is of course dependent on the impact parameter of the collision so that knowing b one can evaluate the number of nucleons that participate in the collision N_{part} or the number of binary nucleon-nucleon collisions N_{coll}. Unfortunately neither the impact parameter nor N_{part} and N_{coll} is directly accessible experimentally and so the nowadays experiments use the concept of centrality classes that will be described in the next subsection.

The N_{coll} and N_{part} dependence on b can be calculated using the Glauber model as well as the average values of N_{coll} and N_{part} can be evaluated for given centrality classes and so the mapping between centrality and impact parameter can be extracted. This is important because theoretical models may use impact parameter as a measure of the overlap whereas experiments, as already stated, divide events into centrality classes.

The Glauber model assumes that nucleons (with sufficiently high energy) are not deflected as they interact with their counterparts from colliding nucleus. It is also assumed that the size of the nucleus is large compared to the range of the

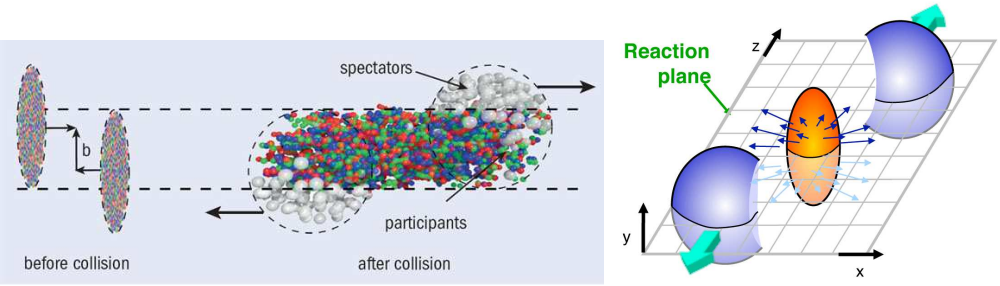

Figure 2.1: Left: Cartoon showing the longitudinal view of the peripheral heavy-ion collision with impact parameter b. Figure adopted from [2]. Right: 3-dimensional view of the peripheral heavy-ion collision with transverse plane depicted. Figure adopted from [3].

nucleon-nucleon force and that the nucleons move independently of each other [4]. These assumptions are usually called optical approximation. The inputs into the Glauber model are the nucleon density and the inelastic nucleon-nucleon cross section. For the nucleon density the three parameter Fermi distribution is usually used

$$\rho(r) = \rho_0 \frac{1 + w(r/R)^2}{1 + \exp\left(\frac{r-R}{a}\right)} \tag{2.1}$$

where R corresponds to the nuclear radius, a is the "skin depth" and w is parameter needed to describe nuclei with maximum density at $r > 0$ (for lead nucleus $w = 0$). ρ_0 is the nucleon saturation density. These parameters are extracted from the low energy electron-nucleus scattering [5].

Now as the two nuclei A (target) and B (projectile) collide we are interested in the probability that a given nucleon is in the tube located at displacement $\vec{s}$ with respect to the centre of the target nucleon (see Figure 2.2). The probability per unit transverse area is

$$\hat{T}_{\mathrm{A}}(\vec{s}) = \int \hat{\rho}_{\mathrm{A}}(\vec{s}, z_A)\mathrm{d}z_{\mathrm{A}} \tag{2.2}$$

where $\hat{\rho}_{\mathrm{A}}$ is the probability per unit volume normalized to unity for finding the nucleon at location $(\vec{s}, z_{\mathrm{A}})$. The analogous formula holds for the tube in the nuclei B at location $\vec{s} - \vec{b}$. Per unit transverse area probability that nucleons are located in the two overlapping tubes of differential area $\mathrm{d}s^2$ is $\hat{T}_{\mathrm{A}}(\vec{s})\hat{T}_{\mathrm{B}}(\vec{s}-\vec{b})\mathrm{d}s^2$. Integrating this probability over all values of $\vec{s}$ gives the so called nuclear overlap function

$$\hat{T}_{\mathrm{AB}}(\vec{b}) = \int \hat{T}_{\mathrm{A}}(\vec{s})\hat{T}_{\mathrm{B}}(\vec{s}-\vec{b})\mathrm{d}s^2. \tag{2.3}$$

Given the value of the inelastic nucleon-nucleon cross section $\sigma_{\mathrm{inel}}^{\mathrm{NN}}$ the probability for the interaction then is $\hat{T}\sigma_{\mathrm{inel}}^{\mathrm{NN}}$. If we know this we can easily calculate the probability that exactly n nucleon-nucleon interactions happen between nuclei A and B which will be determined by binomial distribution

$$P(n, \vec{b}) = \binom{AB}{n} \left[\hat{T}_{\mathrm{AB}}(\vec{b})\sigma_{\mathrm{inel}}^{\mathrm{NN}}\right]^n \left[1 - \hat{T}_{\mathrm{AB}}(\vec{b})\sigma_{\mathrm{inel}}^{\mathrm{NN}}\right]^{AB-n} \tag{2.4}$$

The total probability of an interaction between A and B is then

$$\frac{\mathrm{d}^2\sigma^{\mathrm{A+B}}}{\mathrm{d}b^2} \equiv p_{\mathrm{inel}}^{\mathrm{A+B}}(b) = \sum_{n=1}^{AB} P(n, \vec{b}) = 1 - \left[1 - \hat{T}_{AB}(\vec{b})\sigma_{\mathrm{inel}}^{\mathrm{NN}}\right]^{AB}. \tag{2.5}$$

In most cases nuclei are not polarized and we are interested only in the scalar value of $\vec{b}$. The total cross section for inelastic interaction between A and B is then

$$\sigma_{\mathrm{inel}}^{\mathrm{A+B}} = \int_0^\infty 2\pi b\mathrm{d}b \left\{1 - \left[1 - \hat{T}_{\mathrm{AB}}(b)\sigma_{\mathrm{inel}}^{\mathrm{NN}}\right]^{AB}\right\} \tag{2.6}$$

The total number of nucleon-nucleon collisions and the number of participating nucleons for the given impact parameter is

$$N_{\mathrm{coll}}(b) = \sum_{n=1}^{AB} nP(n, b) = AB\hat{T}_{\mathrm{AB}}(b)\sigma_{\mathrm{inel}}^{\mathrm{NN}} \tag{2.7}$$

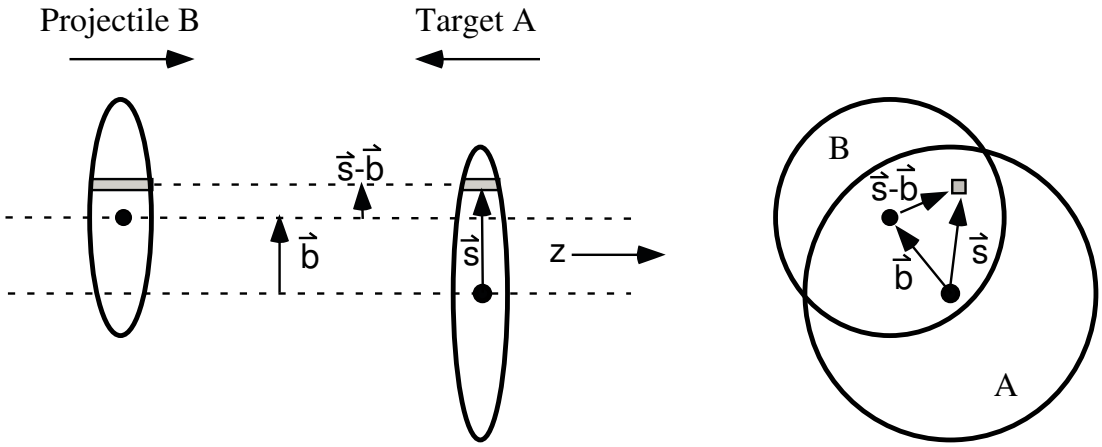

Figure 2.2: Representation of the geometry variables of the Glauber model used in the text. Figure adopted from [4].

$$
\begin{aligned}
N_{\mathrm{part}}(\vec{b}) = A \int \hat{T}_{\mathrm{A}}(\vec{s}) \left\{ 1 - \left[1 - \hat{T}_{\mathrm{B}}(\vec{s} - \vec{b}) \sigma_{\mathrm{inel}}^{\mathrm{NN}} \right]^{B} \right\} \mathrm{d}^2 s \\
+ B \int \hat{T}_{\mathrm{A}}(\vec{s} - \vec{b}) \left\{ 1 - \left[1 - \hat{T}_{\mathrm{A}}(\vec{s}) \sigma_{\mathrm{inel}}^{\mathrm{NN}} \right]^{A} \right\} \mathrm{d}^2 s
\end{aligned}
\tag{2.8}
$$

where the terms in brackets are in fact total inelastic nucleon-nucleus cross sections

$$
\sigma_{\mathrm{inel}}^{\mathrm{A(B)}} = \int \mathrm{d}^2 s \left\{ 1 - \left[1 - \hat{T}_{\mathrm{A(B)}}(\vec{s}) \sigma_{\mathrm{inel}}^{\mathrm{NN}} \right]^{A(B)} \right\}. \tag{2.9}
$$

A different approach to the Glauber model is to use Monte Carlo simulation to calculate quantities and variables discussed above. The positions of the nucleons within the nuclei are generated according to the nucleon density and the nucleus-nucleus collision for the given (or generated) impact parameter b is then treated as a sequence of independent binary nucleon-nucleon collisions. The classical and Monte Carlo approaches give consistent results for N_{col} and N_{part} [4].

2.2 Centrality

The centrality is the key concept in heavy-ion collisions that allows to select collisions with various geometries (i.e. various impact parameters) when analyzing experimental data. The basic idea is to select events with the least restrictive trigger and divide them into successive percentiles of the total inelastic non-Coulomb nucleus-nucleus cross section. In the ATLAS experiment [6], this division is based on the sum of the total transverse energy at the EM scale deposited in the forward calorimeter (FCal) $\Sigma E_{\mathrm{T}}^{\mathrm{FCal}}$ [7]. Measured $\Sigma E_{\mathrm{T}}^{\mathrm{FCal}}$ distribution divided into 10% centrality intervals along with the Monte Carlo Glauber calculation is depicted in Figure 2.3. Knowing $\Sigma E_{\mathrm{T}}^{\mathrm{FCal}}$ for a given event one can easily determine into which centrality class the event belongs. The basic idea behind this procedure is that the total amount of transverse energy deposited in FCal (and also N_{col} and N_{part}) monotonically increases when going from peripheral ("large" impact parameter) to central collisions ("small" impact parameter). Having this distribution and good agreement between data and simulation one can calculate b and the average numbers of participating nucleons $\langle N_{\mathrm{part}} \rangle$ and binary collisions $\langle N_{\mathrm{coll}} \rangle$ in given centrality selection as shown in Figure 2.4 [8].

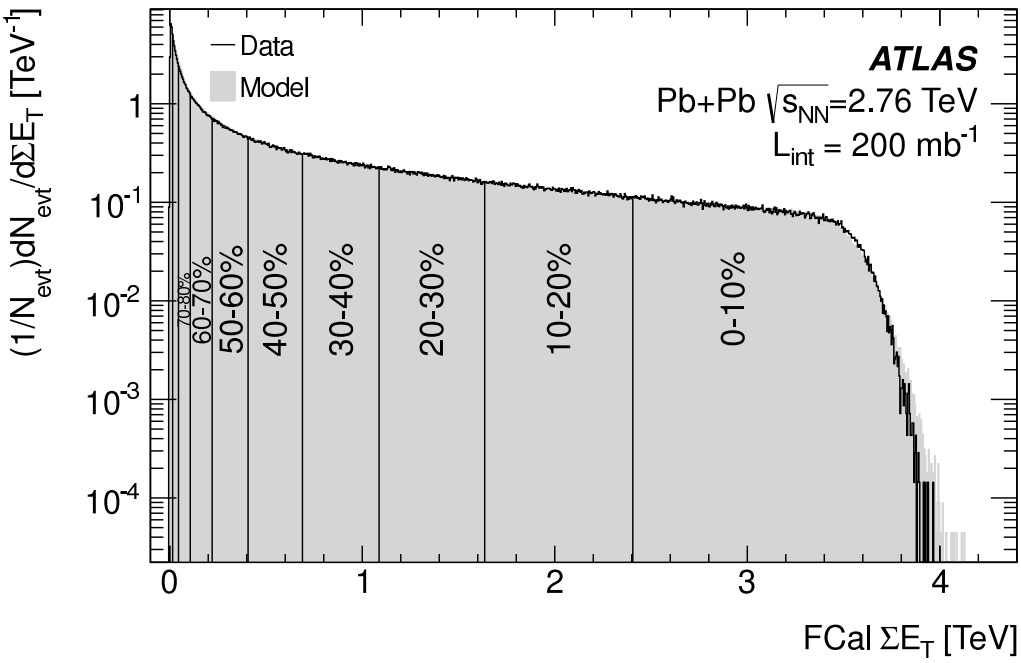

Figure 2.3: Measured FCal $\sum E_{\mathrm{T}}$ distribution divided into 10% centrality intervals [7].

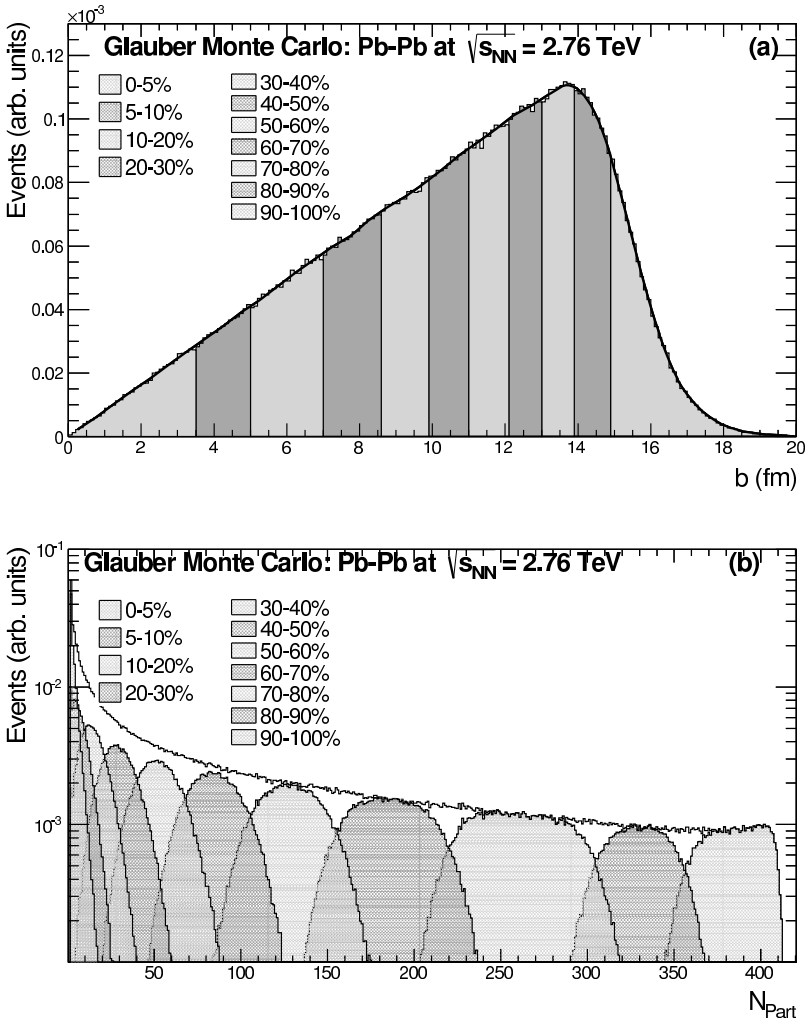

Figure 2.4: Geometric properties of Pb-Pb collisions at $\sqrt{s_{\mathrm{NN}}} = 2.76$ TeV obtained from a Glauber Monte Carlo calculation: Impact parameter distribution (top), sliced for percentiles of the hadronic cross section, and distributions of the number of participants (bottom) for the corresponding centrality classes [8].

Table 2.1 shows the number of participants for different centrality bins as calculated by ATLAS. These numbers are common for all heavy ion analyses at given $\sqrt{s_{\mathrm{NN}}}$.

Centrality	N_{part}
0-10%	356
10-20%	261
20-30%	186
30-40%	129
40-50%	86
50-60%	53
60-80%	23

Table 2.1: The relation between centrality and the number of participants.

3. Quantum Chromodynamics, Quark Gluon Plasma and Jet Quenching

3.1 Quantum Chromodynamics

The theory that describes strong interaction is the so called quantum chromodynamics (QCD). QCD was established in 1973 when David Gross and Frank Wilczek and independently David Politzer discovered that non-abelian gauge theories can exhibit a property called asymptotic freedom [9, 10].

QCD is the quantum field theory with non-abelian gauge symmetry group SU(3) that attempts to describe the strong interaction. Basic constituents are fermions called quarks plus their antiparticles (anti-quarks) that come in six different flavors (each flavor has different mass). Apart from the common electric charge, which is irrelevant in QCD, each quark carries strong charge that is called color. There are three types of color - red, green and blue. The interaction between quarks is mediated by the gluons that come in eight different color-anticolor states. The theory is described by the Lagrange density [11, 12]

$$\mathcal{L}^{\mathrm{QCD}} = \sum_{f=1}^{6} \bar{\Psi}_f \left(i\gamma^\mu D_\mu - m_f \right) \Psi_f - \frac{1}{4} F_{\mu\nu,a} F^{\mu\nu,a}, \tag{3.1}$$

where Ψ is the spinor with quark fields, D_μ is the covariant derivative and $F_{\mu\nu,a}$ is the non-abelian field strength. Covariant derivative takes the form

$$D_\mu \equiv \partial_\mu + igA_{\mu a}T_a, \tag{3.2}$$

where g is the strong interaction coupling constant, A_a are the gluon fields and T_a are the generators of the SU(3) group. The expression of the field tensor in terms of gluon fields is

$$F_{\mu\nu,a} \equiv \partial_\mu A_{\nu a} - \partial_\nu A_{\mu a} - gC_{abc}A_{\mu b}A_{\nu c}, \tag{3.3}$$

where C_{abc} are the real numbers called structure constants that satisfy

$$[T_a, T_b] = iC_{abc}T_c. \tag{3.4}$$

In principle one can derive the Feynman rules from above formulas and use them for the calculations of cross sections. The problem arises if one needs to include the diagrams with the loops because of logarithmic divergences that appear in the calculations. The renormalization procedure solves this problem but it introduces the new parameter μ called renormalization scale, that is not present in the original Lagrange density $\mathcal{L}^{\mathrm{QCD}}$ and is not fundamental parameter of the theory. Results of the perturbative calculations, if calculated up to finite order, then depend on the choice of the renormalization scale μ. This dependency can be translated into the dependence of the coupling constant g on the scale μ which is

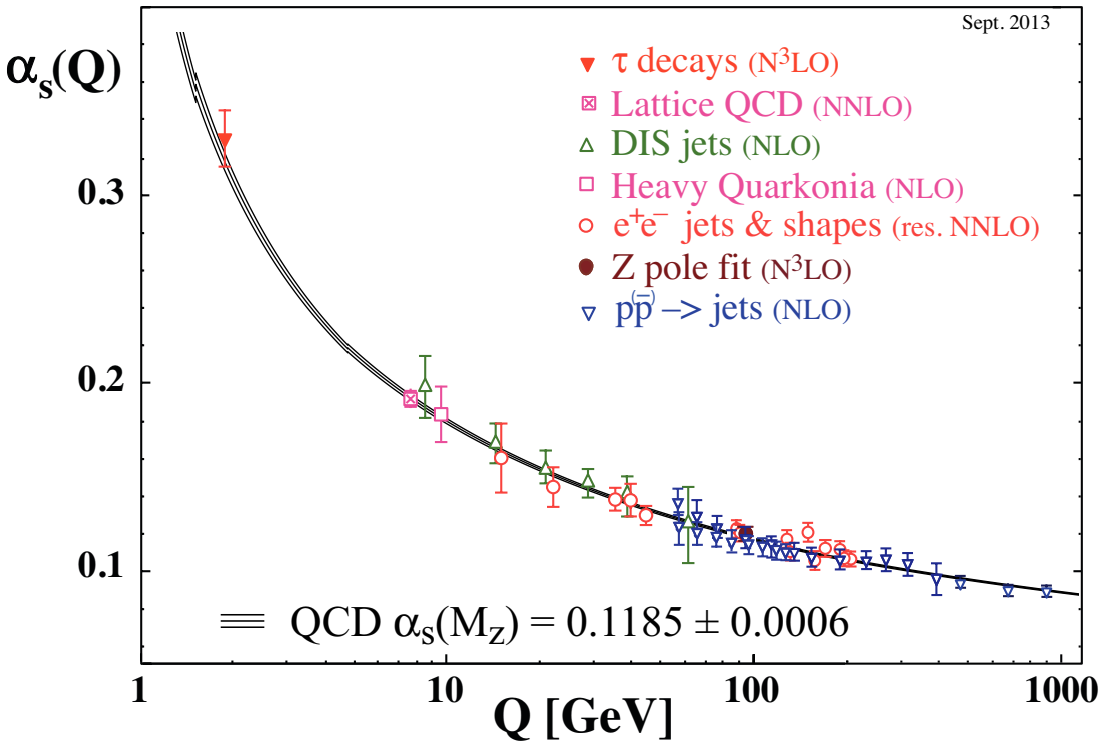

Figure 3.1: Summary of measurements of running coupling constant α_S as a function of the energy scale Q [12].

expressed in the renormalization group equation

$$\mu \frac{\mathrm{d}g(\mu)}{\mathrm{d}\mu} = \beta(g(\mu)) \tag{3.5}$$

which allows us to calculate the coupling constant $g(\mu)$ at given scale μ if we know $g(\mu_0)$ at some different scale μ_0. Function β is the power series in g

$$\beta(g) = -g\left(\frac{\alpha_S}{4\pi}\beta_1 + \left(\frac{\alpha_S}{4\pi}\right)^2 \beta_2 + \dots\right) \tag{3.6}$$

where $\alpha_S = \sqrt{g/4\pi}$. β function can be computed in perturbation theory. In QCD the result for the lowest order approximation is

$$\beta_1 = (11N_c - 3n_f)/3 \tag{3.7}$$

which is always positive for six quark flavors. That is caused by the non-abelian nature of the theory (as opposed to the QED). The solution of the differential equation 3.5 in the lowest order in terms of α_S is

$$\alpha_S(\mu^2) = \frac{4\pi}{\beta_1 \ln \mu^2/\Lambda^2} \tag{3.8}$$

where Λ sets the scale for the running coupling. This is the famous formula showing dependence of the strong coupling constant on the scale of the process μ. Because β_1 is positive the strong coupling logarithmically weakens with increasing μ. This dependence of the α_S on the scale μ is subject to many measurements - summary of some of them along with theoretical prediction is in Figure 3.1.

3.2 QGP and QCD Phase Diagram

QCD is a well defined theory at arbitrary distance and so one can in principle study the properties of a QCD matter - matter composed of quarks and gluons. In practice the situation is difficult due to the non-perturbative nature of the problem. Nevertheless, it's possible to deduce at least qualitatively various properties and phases of the strongly interacting matter and deduce how does the phase diagram of QCD, or at least parts of it, looks like. It is also possible to study reachable parts of the phase diagram experimentally.

The phase diagram of the QCD matter is usually described in terms of the state variables temperature T and baryon chemical potential μ_{B}. The best known phase of the strongly interacting matter is a nucleus of arbitrary atom. This is in fact liquid made out of nucleons. With increasing temperature nucleons can 'evaporate' from the liquid to become gas. This is a phase transition of the first order up to a certain critical temperature from which the transition becomes crossover and one is not able to distinguish between the two phases.

When the temperature becomes so high that the momentum of the hadrons is of the order of Λ_{QCD}, hadrons stop existing anymore and the new state of matter called quark gluon plasma (QGP) is created. The interesting question is whether there is a thermodynamical phase transition between hadron gas and QGP and what type of phase transition it is. This question is at least partially answered by the lattice QCD (LQCD) which is a non-perturbative approach to solve QCD. LQCD is widely used and gives reliable results at non-zero temperatures T and zero baryon chemical potential μ_{B}. These results show that there is an analytic crossover between hadron gas and QGP at $T_{\mathrm{C}} \approx 155\,\mathrm{MeV}$ and $\mu_{\mathrm{B}} = 0$ [13, 14]. However, at non-zero chemical potential there is a so called sign problem [15, 16] and LQCD cannot be directly used despite a lot of effort that has been put into the solution of this problem. There are some methods that attempt to describe this region but the results are not reliable and the question whether or not there is a critical point and a phase transition between hadronic matter and QGP at non-zero μ_{B} remains opened [17]. At very large values of chemical potential it is expected that there is a transition into a color superconducting phase [18]. The sketch of how the QCD phase diagram can look like is in Figure 3.2. Some parts of the phase diagram are speculative.

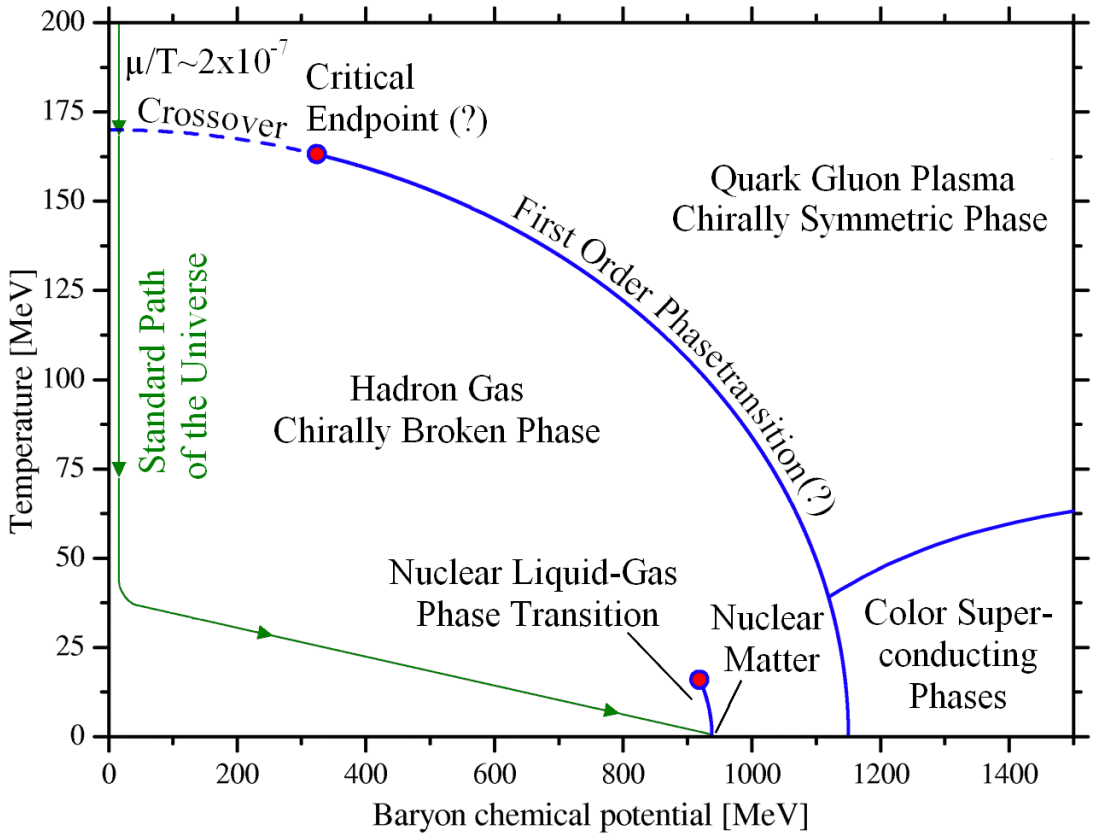

Figure 3.2: The QCD phase diagram. Some parts of this phase diagram are speculative. Figure adopted from [19].

3.3 Experimental signatures of QGP formation

There are several phenomena observed at RHIC and LHC experiments that suggest the formation of the QGP in heavy-ion collisions. There are even some phenomena that suggest the possibility of the formation of the QGP-like matter in collisions of the so called small systems, i.e. proton-nucleus and proton-proton collisions. Not to make this section too long, the following list of experimental results is not attempting to be complete.

3.3.1 Soft Probes

The first measurement that will be reviewed is the measurement that utilizes soft probes, i.e. particles with the low transverse momentum $p_{\mathrm{T}}^{\mathrm{particle}} \ll 10\,\mathrm{GeV}$. These particles are created in the latter stage of the HI collision by the hadronization of the bulk of QCD matter. Studying this type of particles one can reveal collective properties of the medium created in the collision.

Azimuthal correlations

Initial stage of the non-central heavy-ion collisions does not posses azimuthal symmetry as can be seen in Figures 2.1 and 2.2. If the medium created in the collision behaves collectively, i.e. if HI collision does not behave like a superposition of nucleon-nucleon collisions, this initial spatial asymmetry may be translated into the azimuthal anisotropy of the produced particle's momentum. Momentum anisotropy is usually expressed as a Fourier series in azimuthal angle ϕ [20]

$$E\frac{\mathrm{d}^3N}{\mathrm{d}p^3} = \frac{\mathrm{d}^2N}{2\pi p_{\mathrm{T}}\mathrm{d}p_{\mathrm{T}}\mathrm{d}\eta}\left(1 + 2\sum_{n=1}^{\infty} v_n(p_{\mathrm{T}},\eta)\cos n(\phi - \Phi_n)\right) \tag{3.9}$$

where p_{T} is the transverse momentum, η is the pseudorapidity and v_n and Φ_n are the magnitude and direction of the n^{th}-order harmonic respectively. Specifically, the second coefficient v_2 represents the magnitude of the so called elliptic flow which may be caused by the difference of the pressure gradients induced by the asymmetry of the collision. Agreement of the measured values of v_2 at low p_{T} with hydrodynamic calculations was one of the main arguments for RHIC experiments to claim that the medium created in the HI collisions is the 'liquid QGP' [21, 22]. At the LHC measurements of the v_n coefficients was extended up to $n = 6$ and to higher momenta [23, 24, 25]. ATLAS measurements of the p_{T} dependence of the v_n coefficients is in Figure 3.3. The size of the v_2 is largest for semi-central collisions (30-40% centrality bin) where the spatial anisotropy of the overlapping area of two nuclei is largest. Presence of the elliptic flow at relatively large p_{T} can be explained as a consequence of the path-length dependence of the parton energy loss, i.e. it is not collective effect. Non-zero values of the higher order coefficients and their independence on the centrality is thought to be due to the fluctuations in the initial geometry.

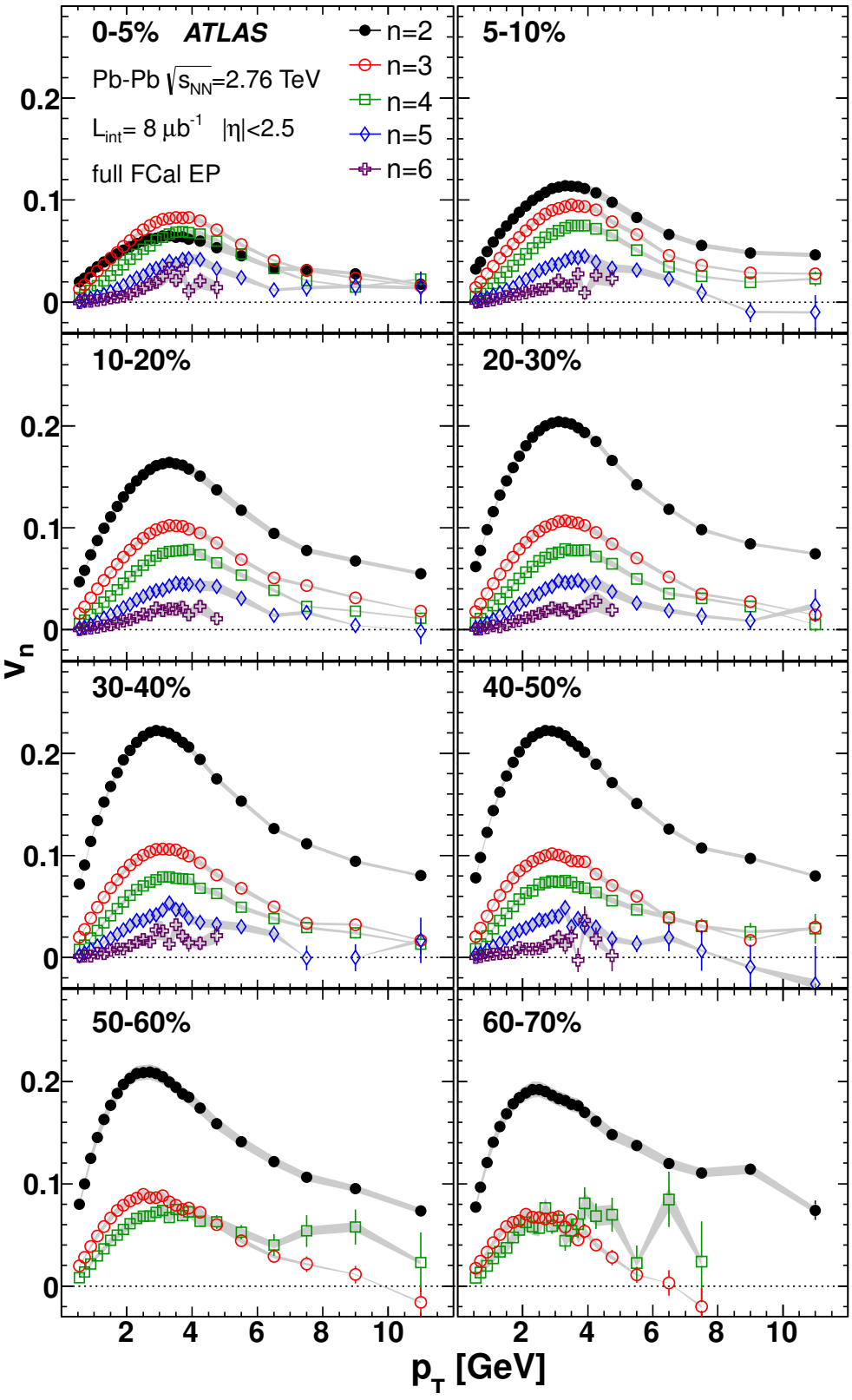

Figure 3.3: v_n vs. p_{T} for several centrality intervals. Figure adopted from [23].

3.3.2 Hard Probes

The measurements of so called Hard Probes use particles with momenta or mass of the order of at least several GeV. These particles are created in the early stages of the collision before the thermalization of the medium, and in subsequent stages of the HI collision they can either probe the created medium by interacting with it or serve as a control probe for the hard processes and its scaling with the number of binary collisions in the case they do not interact strongly.

Single particle spectra

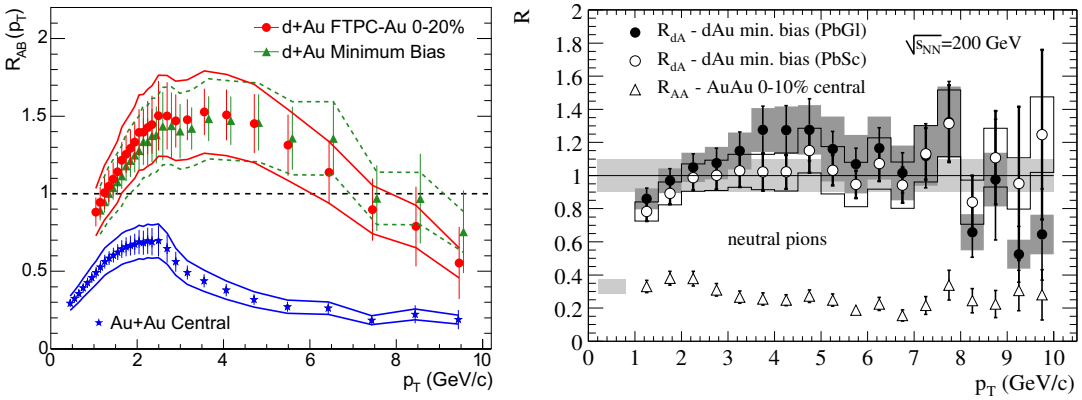

Figure 3.4: Charged particle R_{AA} as a function of p_{T} as measured by STAR (left) and PHENIX(right) [26, 27] in deuteron-gold and gold-gold collisions.

One of the conceptually most straightforward measurements is the measurement of the single particle spectra. The idea is to compare the production of particles at given momenta in HI and pp collisions. The variable that expresses the level of reduction or enhancement of the particle production in HI collisions is the R_{AA} which is defined as

$$R_{\mathrm{AA}} = \frac{1}{\langle T_{\mathrm{AA}} \rangle} \frac{1/N_{\mathrm{evt}} \mathrm{d}^2 N_{\mathrm{PbPb}}/\mathrm{d}\eta \mathrm{d}p_{\mathrm{T}}}{\mathrm{d}^2\sigma_{pp}/\mathrm{d}\eta \mathrm{d}p_{\mathrm{T}}}. \tag{3.10}$$

R_{AA} is the ratio between the density of the particles in the p_{T} and η phase space produced in HI collisions (in given centrality bin) to the same particle density in the pp collisions scaled by the average nuclear overlap function for given centrality bin. In other words it is a variable that takes into account different parton flux in the HI collisions so if there is no modification of the particle production mechanism in the HI collisions the R_{AA} is equal to one. If the R_{AA} is smaller the production of particles is suppressed and the production is enhanced if R_{AA} is larger than one. R_{AA} can be defined in analogical way also for different probes like for example jets.

R_{AA} for hard particles was measured at RHIC [27, 26] where the strong suppression was observed for the first time as shown in Figure 3.4. In Figure 3.5 the ATLAS measurement of R_{AA} for charged particles in central collisions as a function of p_{T} is shown [28, 29]. Comparison with other LHC experiments is also included. The p_{T} dependence has an interesting shape with minimum at $\approx 7\,\mathrm{GeV}$

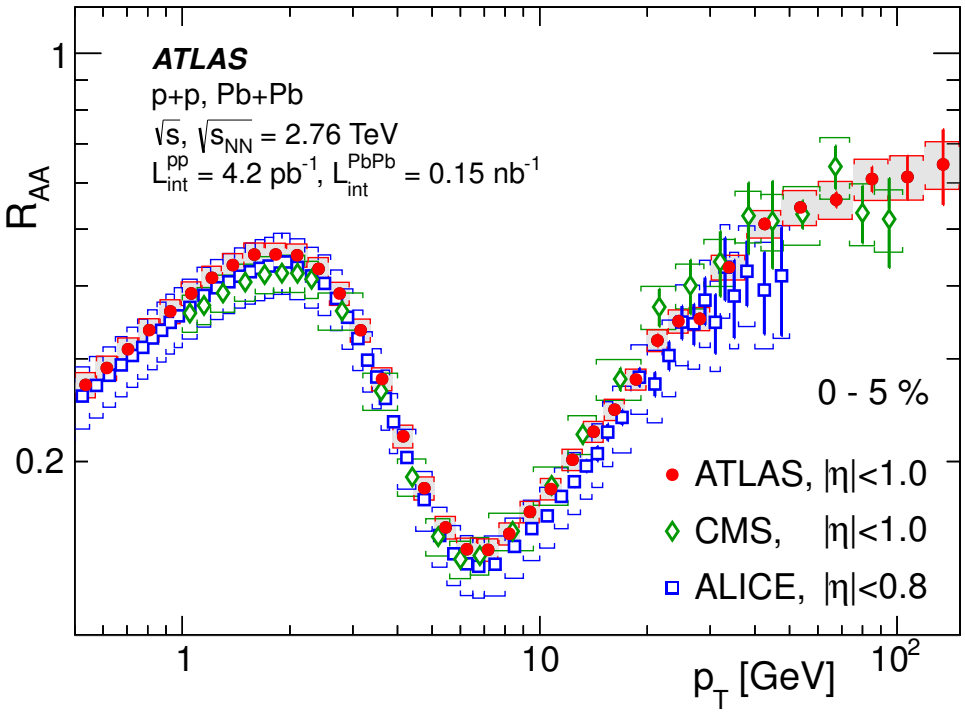

Figure 3.5: Charged particle R_{AA} as a function of p_{T}. Figure adopted from [28].

where R_{AA} is about 0.2 which means suppression by a factor of five. At high p_{T} the R_{AA} reaches a value of ≈ 0.6 which is consistent with the value of R_{AA} for jets at the same p_{T} (see below).

Quarkonia

Measurement of the J/ψ production was first proposed in 1986 in famous paper by Matsui and Satz [31]. The authors suggest that the color screening in the created QGP will cause the deconfinement of the $c\bar{c}$ bound state and subsequently the suppression of the J/ψ production.

The J/ψ production in HI collisions has been first measured already at the CERN SPS [32] and since then also at RHIC and LHC. The results from RHIC show a strong suppression of the J/ψ production [33, 34]. The experiments at the LHC reported significantly weaker suppression at low p_{T} which can be explained as a consequence of the regeneration of the J/ψ's due to the large abundance of the c ($\bar{c}$) quarks in the created fireball and their possible recombination [35]. This effect should be negligible at higher p_{T}. Results from the ALICE experiment (which include also PHENIX results) confirm this expectations as shown in Figure 3.6 .

The high luminosity and center of mass energy reached at the LHC made it possible to measure bottomonia production in HI collisions. Results published by CMS experiment [36] show suppression of all three $\Upsilon(1S, 2S, 3S)$ states, see Figure 3.7. While the suppression of the $\Upsilon(1S)$ state is at the level of ≈ 0.5 the $\Upsilon(2S, 3S)$ states are suppressed much stronger with 3S state basically invisible in the dimuon mass spectrum. This 'ordering' of the suppression is in agreement with ordering of the binding energies (loosely bound states are suppressed more).

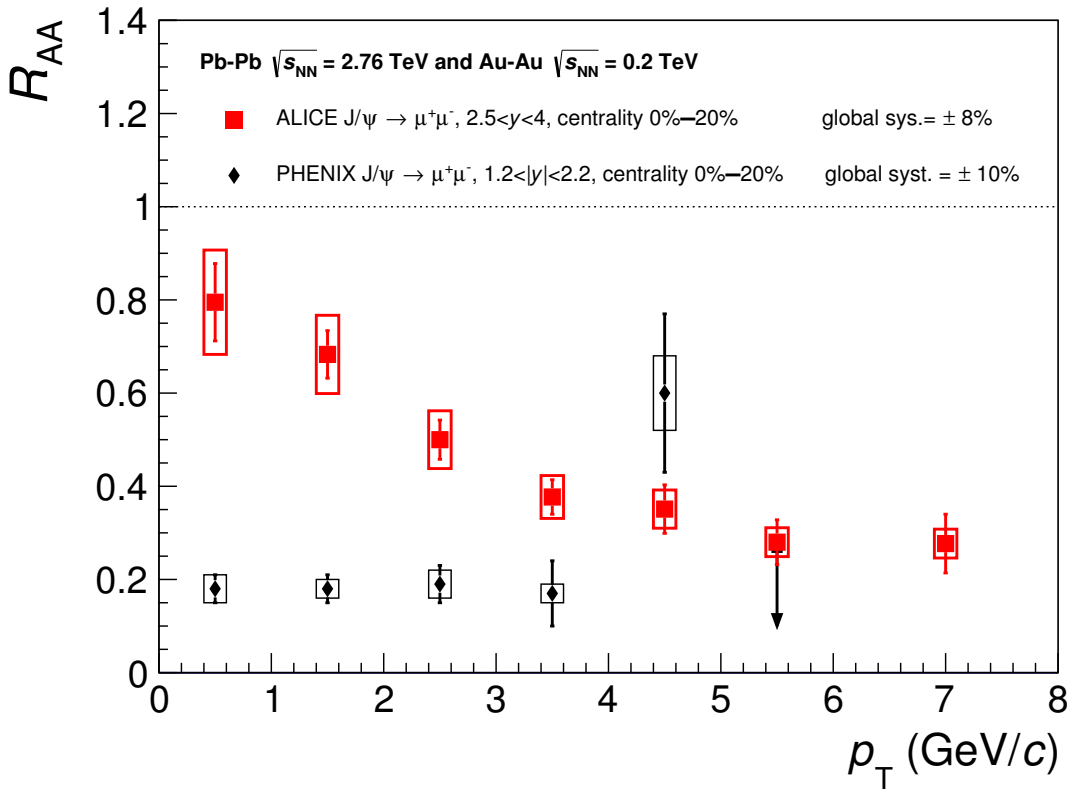

Figure 3.6: p_{T} dependence of J/ψ R_{AA} measured by ALICE (red squares) and PHENIX (black circles). Figure adopted from [30].

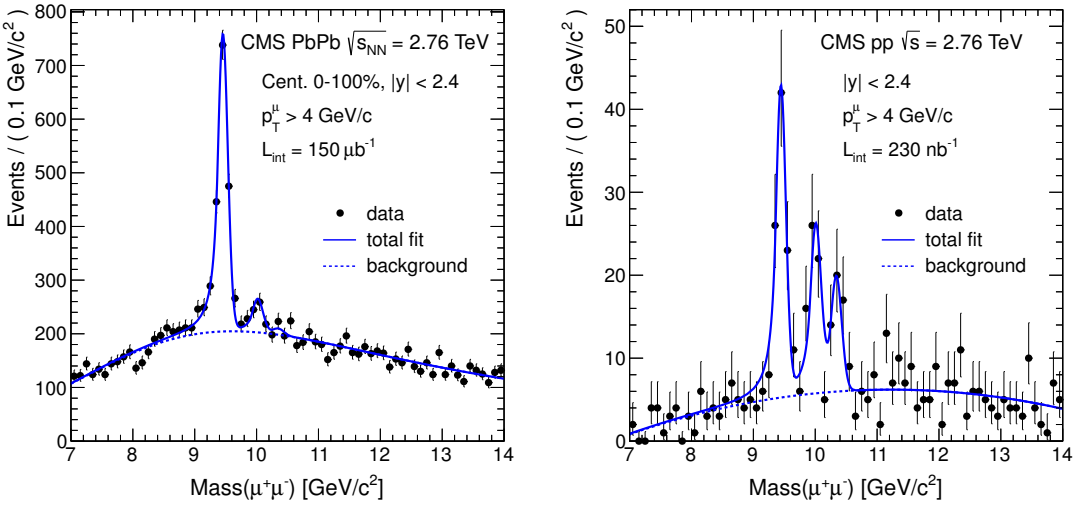

Figure 3.7: Dimuon invariant-mass distributions from the Pb+Pb (left) and pp (right) data at $\sqrt{s_{\mathrm{NN}}} = 2.76\,\mathrm{TeV}$. Figure adopted from [36].

To further investigate the centrality dependence of the Υ production the CMS showed N_{part} dependence of the R_{AA} for 1S and 2S states and $\Upsilon(2S)/\Upsilon(1S)$ double ratio (fig. 3.8). The R_{AA} for both states clearly decreases with the centrality while the double ratio seems to be independent of N_{part}.

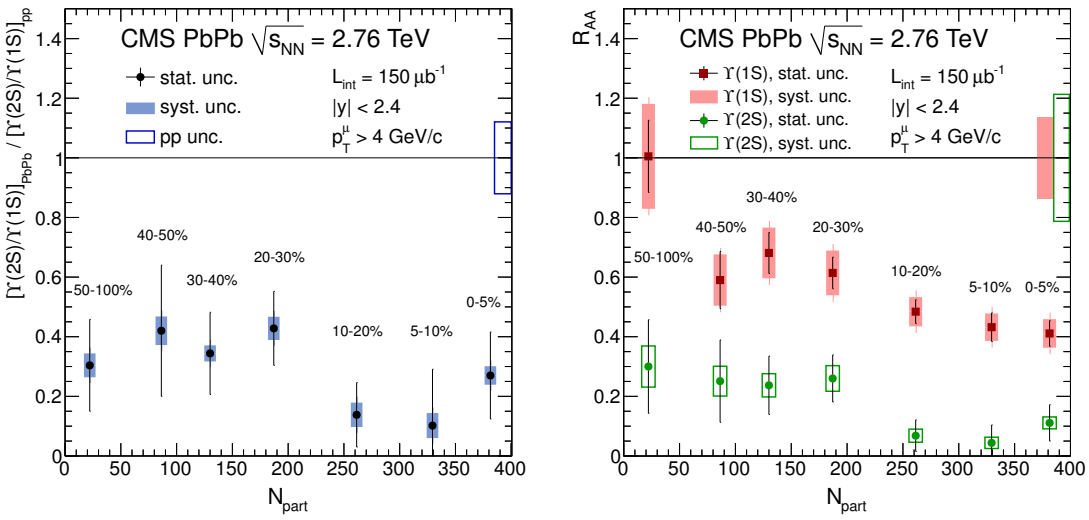

Figure 3.8: N_{part} dependence of the $\Upsilon(2S)/\Upsilon(1S)$ double ratio (left). N_{part} dependence of the R_{AA} for 1S and 2S states (right). Figure adopted from [36].

Electroweak probes

The particles that don't interact strongly, i.e. photons and massive Z and $\mathrm{W}^{\pm}$ bosons, are called electroweak probes. These particles are not influenced by the medium created in HI collisions so they can be used as a control probe for high-p_{T} or high-mass particle production rates. Low-p_{T} direct photons can also be used as a thermal probe of the created fireball.

ALICE experiment measured photons in Pb+Pb collisions for three centrality classes. The conclusion of the measurement is that in all centrality classes, the spectra at high-p_{T} follow the expectations based on the direct photon yields in pp collisions. In the low-p_{T} region the excess of the direct photons in semi-central and central collisions was observed by ALICE. Fitting the exponential function to the excess obtained by subtracting the pQCD contribution, the inverse slope parameter was extracted $T_{\mathrm{eff}} = (297 \pm 12^{\mathrm{stat}} \pm 41^{\mathrm{syst}})$ MeV [37].

ATLAS and CMS measured photon yields at high-p_{T} for isolated photons, i.e. photons that have little hadronic activity nearby [38, 39]. These photons are likely not to come from the hadronic decays. Results from both experiments are in Figure 3.9. The conclusion from both experiments is that photon yields at high-p_{T} are within statistical, systematical and theoretical uncertainties in agreement with yields in pp collisions (CMS) or in agreement with next-to-leading-order pQCD predictions (ATLAS) and consequently that photon production scales with mean nuclear thickness, i.e. their production and propagation is not influenced by the medium.

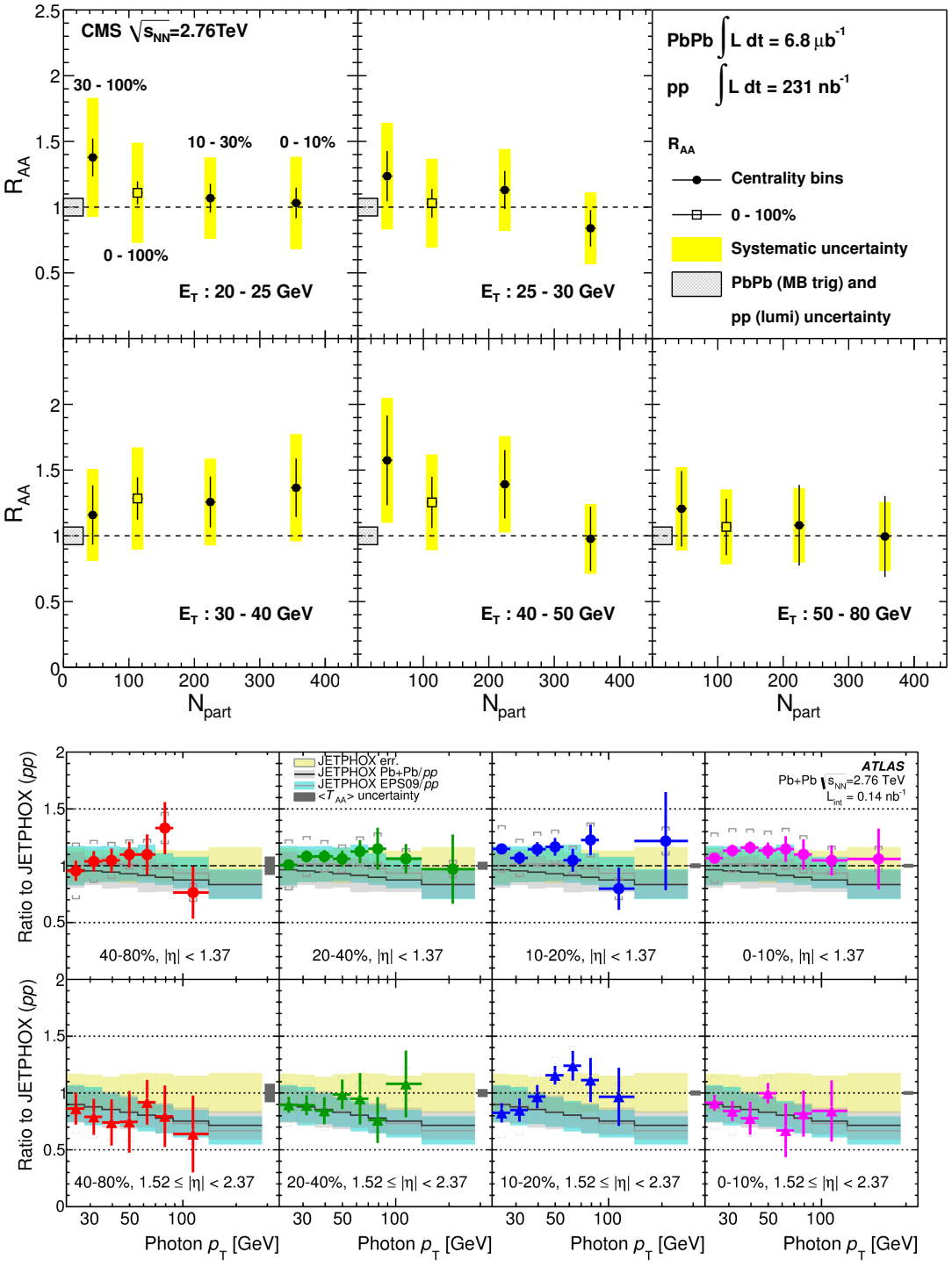

Figure 3.9: The measured nuclear modification factor R_{AA} as a function of Pb+Pb centrality for five different photon transverse energy intervals [39] (top). Fully corrected normalized yields of prompt photons as a function of p_{T} divided by JETPHOX predictions for pp collisions [38] (bottom).

All three LHC experiments measured also the production of the heavy electroweak bosons. Two results are depicted in Figure 3.10. The conclusion of the measurements is analogous to the study of photons, i.e. the production of massive electroweak bosons is not influenced by the medium in HI collisions.

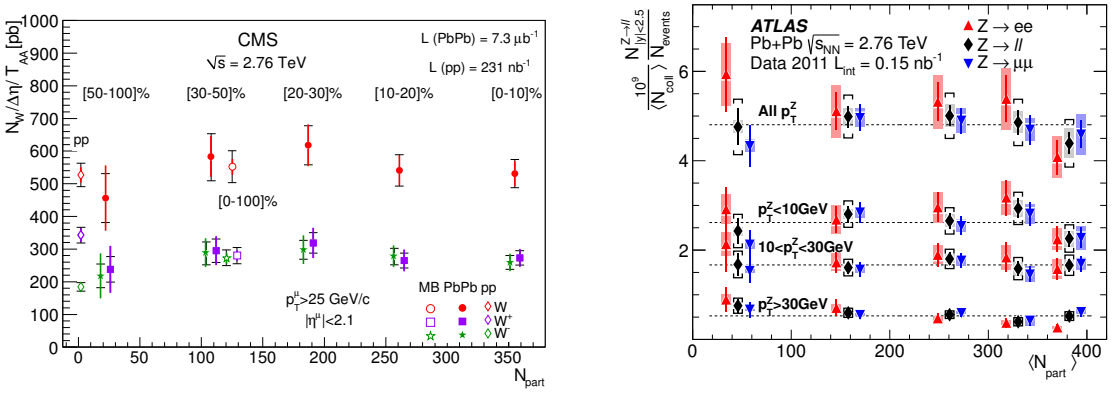

Figure 3.10: Left: Centrality dependence of the $W \to \mu\nu$ yields, in Pb+Pb collisions, separated by charge, W^+ (violet triangles) and W^- (green stars) and the sum of the two (red points). The open symbols are for minimum bias events. The W yields in pp data are also included (at $N_{\text{part}} = 2$). Figure adopted from [40] Right: Centrality dependence of Z boson yields divided by $\langle N_{\text{coll}} \rangle$ for ee (upward pointing triangles, shifted left), $\mu\mu$ (downward pointing triangles, shifted right) and their weighted average (diamonds) [41].

3.4 Jet Quenching

One of the most important experimental results suggesting creation of the deconfined matter in HI collisions is the so called jet quenching. It is the effect where high-p_{T} partons (that later fragment into jets) lose significant portion of their energy by interaction with the medium created in the HI collision. It was first predicted by Bjorken in 1982 [42], then this idea was further developed and modified in 90's by Gyulassy, Wang and others [43, 44, 45]. First indirect experimental observation was made by RHIC experiments [46, 47] confirmed in 2010 by the observation of dijet asymmetry in HI collisions [48, 49] which was one of the most important results of the LHC experiments during the first years of the LHC operation.

As stated above the first prediction of jet quenching was made by Bjorken. In work [42] author suggests that high-p_{T} partons lose energy by the elastic scattering with quarks and gluons in the QGP from the collision in a process analogical to the energy loss of the ionizing particle in QED. In [43], Gyulassy and Plümer estimated that collisional energy loss of a fast parton in QGP is of the order of $\approx 0.1\,\text{GeV}$. Since then there was a great progress in the understanding of the fast parton passage through the QGP. It turned out that high-energy partons lose energy in QGP predominantly by the medium-induced radiation and that the energy loss is much larger in QGP than in the cold nuclear matter [50, 45, 51, 52].

3.4.1 Experimental results

There are several jet observables that were predicted to be modified by the jet quenching and that can serve as a signature of the QGP formation in HI collisions. Some of them will be discussed in this section.

R_{AA} for single particles measured at RHIC (repeated by LHC experiments later) can be considered as the first indirect measurement of jet quenching in

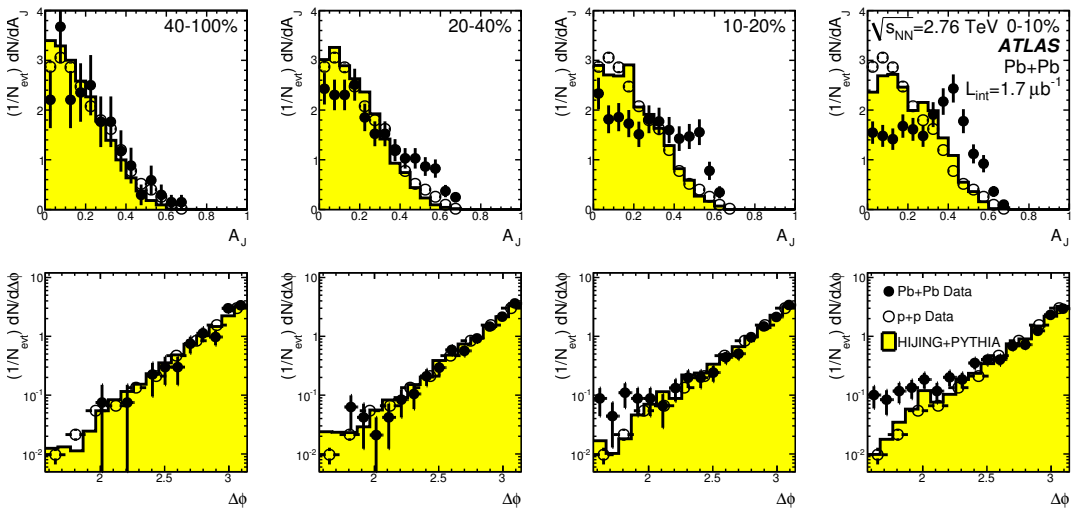

Figure 3.11: Dijet asymmetry distributions for Pb+Pb data (black points), HIJING with superimposed PYTHIA dijets (solid yellow histograms) and *pp* data at $\sqrt{s} = 7\,\text{TeV}$ (open circles) as a function of collision centrality (left to right from peripheral to central events) [48].

HI collisions, see section 3.3.2. The new era of HI jet physics has begun with the start of the LHC heavy-ion program due to the large increase of the jet production cross section at the LHC centre-of-mass energies and high precision and large acceptance of the LHC experiments.

Dijet asymmetry

Historically first direct measurement of jet quenching was the observation of events with large jet transverse momentum imbalance in central HI collisions by ATLAS and CMS [48, 49]. In Figure 3.11 the distribution of dijet asymmetry distribution, defined as:

$$A_J = \frac{E_{T1} - E_{T2}}{E_{T1} + E_{T2}} \tag{3.11}$$

is shown for jets in HI, *pp* collisions and Pythia simulation as it was measured by ATLAS. The asymmetry distribution in Pb+Pb collisions much differs from *pp* and simulation distributions in central collisions. The peak at $A_J = 0.5$ means that there is a lot of dijet pairs with one of the jet's energy reduced by a large fraction.

Jet R_{AA}

The natural question is how is the production of the jets at a given p_{T} influenced by the medium created in the collision. This can be answered through the p_{T} dependence of the R_{AA} of jets. ATLAS and CMS published their jet R_{AA} from 2.76 TeV Pb+Pb collisions in 2014 resp. 2017 [53, 54]. In Figure 3.12 the jet R_{AA} for jets as a function of p_{T} (left) and rapidity (top right) for three different centrality bins is shown. The jet production in central collisions is suppressed by a factor of ≈ 2. The R_{AA} is weakly dependent on jet p_{T}. The rapidity dependence of the jet R_{AA} is negligible in the measured interval. The gradual suppression of

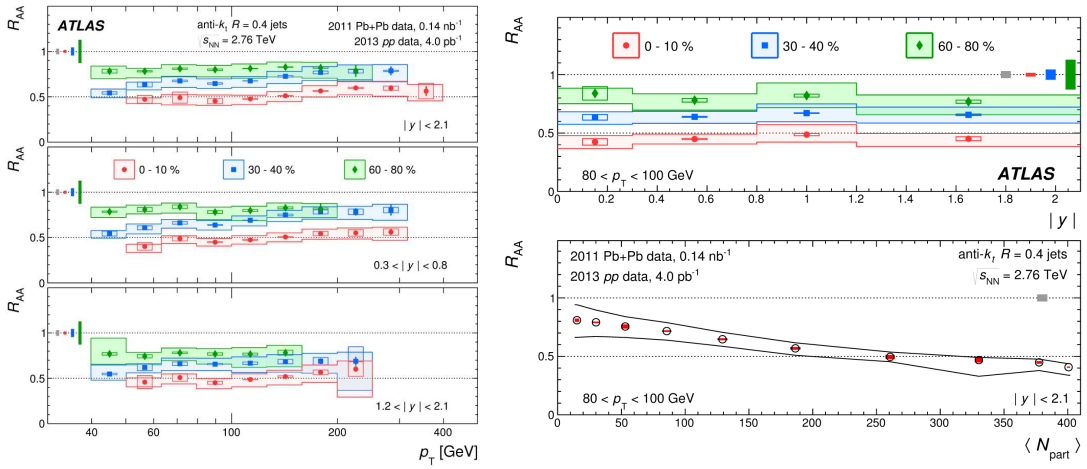

Figure 3.12: Left: Jet R_{AA} as a function of p_{T} in different centrality bins with each panel showing a different range in $|y|$. Right: The R_{AA} for jets with $80 < p_{\mathrm{T}} < 100\,\mathrm{GeV}$ as a function of $|y|$ for different centrality bins (top) and as a function of $\langle N_{\mathrm{part}} \rangle$ for the $|y| < 2.1$ range (bottom). Figures adopted from [53].

R_{AA} with increasing centrality can be seen in detail in the right bottom plot of Figure 3.12.

Production of neighbouring jets

Another interesting measurement that attempted to study the jet quenching from different perspective is the measurement of the production of neighbouring jets by ATLAS [55, 56]. The basic quantity this measurement studied was the rate of the neighbouring jets that accompany a test jet, $R_{\Delta R}$, defined as

$$R_{\Delta R} = \frac{1}{\mathrm{d}N_{\mathrm{jet}}^{\mathrm{test}}/\mathrm{d}{E_{\mathrm{T}}}^{\mathrm{test}}} \sum_{i=1}^{N_{\mathrm{jet}}^{\mathrm{test}}} \frac{\mathrm{d}N_{\mathrm{jet},i}^{\mathrm{nbr}}}{\mathrm{d}{E_{\mathrm{T}}}^{\mathrm{test}}}({E_{\mathrm{T}}}^{\mathrm{test}}, E_{\mathrm{T,min}}^{\mathrm{nbr}}, \Delta R) \tag{3.12}$$

where ΔR is the angular distance between test jet and neighbouring jet in the pseudorapidity-azimuthal angle plane. $R_{\Delta R}$ expresses how many jets accompany a test jet in the specific annulus in ΔR. The jets not coming from the same hard scattering were subtracted on the statistical basis. To quantify the centrality dependent modification of the production of neighbouring jets the ratios $\rho_{R_{\Delta R}} = R_{\Delta R|\mathrm{cent}}/R_{\Delta R|40-80}$ between the $R_{\Delta R}$ distributions for a given centrality and the $R_{\Delta R}$ from the peripheral collisions were calculated. In Figure 3.13 the dependence of the ratio on the $E_{\mathrm{T}}^{\mathrm{test}}$ (top) and the $E_{\mathrm{T}}^{\mathrm{nbr}}$ is depicted - the summary of the results is that the production of neighbouring jets in central collisions is suppressed by a factor of ≈ 2 which is consistent with the suppression factor of the inclusive jets. No significant dependence on the E_{T} of the test jet was observed however the $\rho_{R_{\Delta R}}$ dependence evaluated as a function of $E_{\mathrm{T}}^{\mathrm{nbr}}$ suggests a decrease of suppression with increasing $E_{\mathrm{T}}^{\mathrm{nbr}}$.

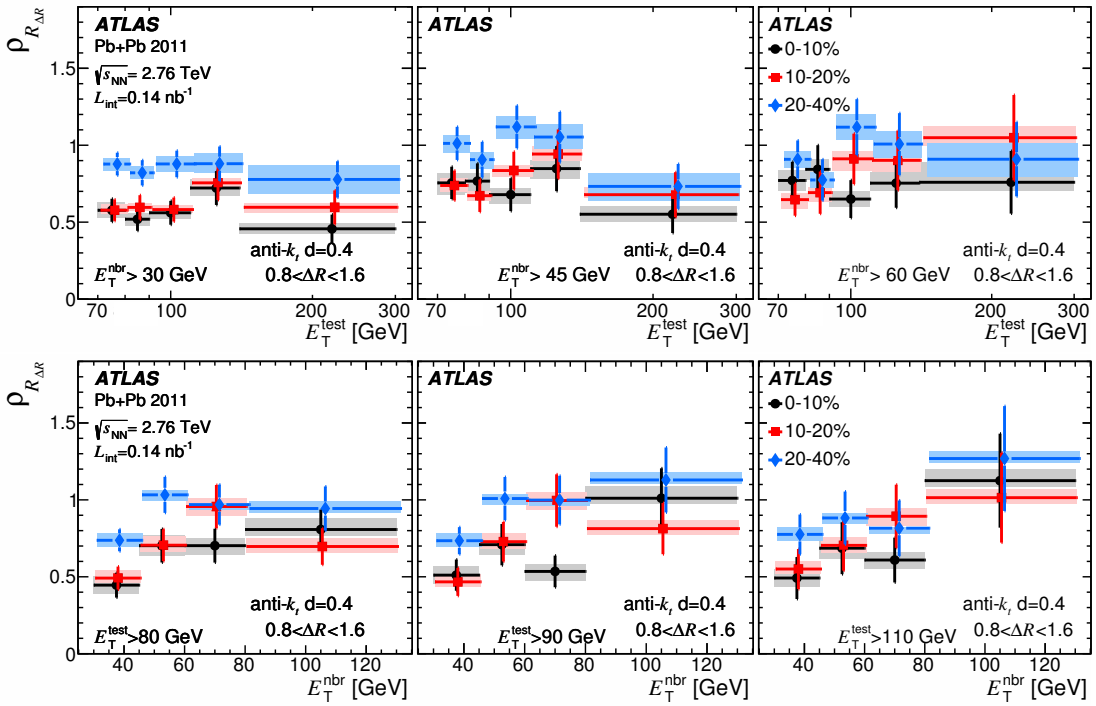

Figure 3.13: The ratio of $R_{\Delta R}$ for three bins of collision centrality to those in 40–80% collisions, $\rho_{R_{\Delta R}} = R_{\Delta R|\mathrm{cent}}/R_{\Delta R|40-80}$ for $d = 0.4$ jets (where d was chosen as a label for the radius parameter of jet clustering algorithm to avoid confusion with the central variable $R_{\Delta R}$ in this measurement). Top: the $\rho_{R_{\Delta R}}$ is evaluated as a function of $E_{\mathrm{T}}^{\mathrm{test}}$ for three different choices of lower bound on $E_{\mathrm{T}}^{\mathrm{nbr}}$. Bottom: the $\rho_{R_{\Delta R}}$ is evaluated as a function of $E_{\mathrm{T}}^{\mathrm{nbr}}$ for three different choices of lower bound on $E_{\mathrm{T}}^{\mathrm{test}}$. The data points and horizontal uncertainties for 10–20%, 20–40%, and 40–80% centrality bins are shifted along the horizontal axis with respect to 0–10% centrality bin for clarity.

4. The ATLAS Experiment at the LHC

4.1 Large Hadron Collider

The Large Hadron Collider is located at the border between Switzerland and France close to the town of Geneva. It is the proton-proton collider that is placed in the 26.7 km long tunnel that was previously built for the LEP collider and lies between 45 m and 170 m below the surface [57]. Being the particle-particle collider, there are two rings with counter rotating beams. It uses superconducting dipole magnets to bend the beam in eight arcs that are in the tunnel and radio-frequency cavities in the straight sections to accelerate the protons. The nominal magnetic field in dipole magnets is 8.33 T which corresponds to beam energy of 7 TeV. The superconducting quadrupole magnets are used to focus the beam. There are four interaction points at the LHC where beams intersect, see Figure 4.1. At these four points the experiments are located - these are ALICE, LHCb, CMS and ATLAS experiment which will be described in the next section.

The designed beam energy per proton in both beams is 7 TeV, however this energy was not reached yet. The first operational year with significant scientific program was 2010 when beams with energy 3.5 TeV each were collided. The energy of proton beams was increased to 4 TeV in 2012. After a long shutdown between 2013 and 2015 the new beam energy of 6.5 TeV was reached in 2015 which is so far the highest energy ever reached in collider. The nominal value of luminosity is $L = 1.0 \times 10^{34}\,\mathrm{cm}^{-2}\,\mathrm{s}^{-1}$. This was first reached in 2016, but was further improved to $L = 1.75 \times 10^{34}\,\mathrm{cm}^{-2}\,\mathrm{s}^{-1}$ in 2017 [58].

Heavy-ion collisions were included in the LHC design from an early stage. The plan was to collide fully stripped lead nuclei $^{208}\mathrm{Pb}^{82+}$ with the beam energy of 2.76 TeV per nucleon and nominal luminosity $1.0 \times 10^{27}\,\mathrm{cm}^{-2}\,\mathrm{s}^{-1}$. The first Pb+Pb collisions at the LHC were recorded in 2010 with $\sqrt{s_{\mathrm{NN}}} = 2.76$ TeV. Second Pb+Pb run with much higher luminosity was held at the end of 2011 and the heavy-ion physics program continued with p+Pb collisions at $\sqrt{s_{\mathrm{NN}}} = 5.02$ TeV and pp collisions at $\sqrt{s} = 2.76$ TeV early in 2013.

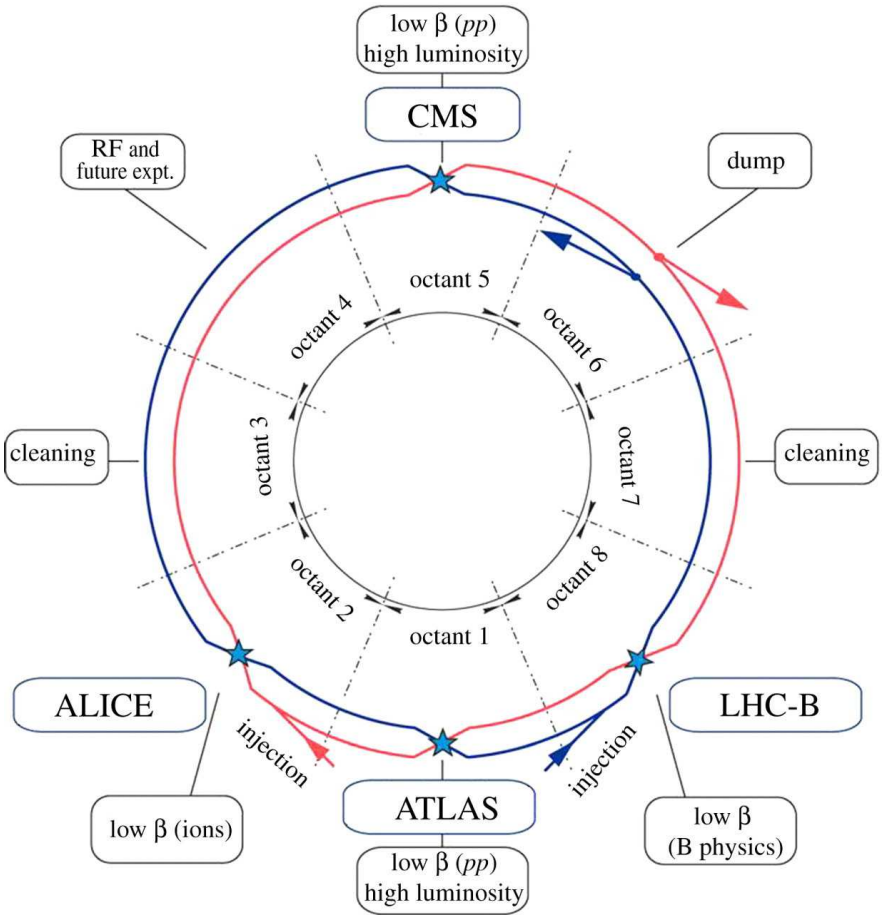

Figure 4.1: Schematic layout of the LHC. Figure adopted from [57].

4.2 ATLAS Experiment

In this section we will describe the ATLAS experiment at the LHC. Most of the information in this section is adopted from Ref. [6].

ATLAS experiment is one of the four main detectors installed at the LHC and one of the two multipurpose ones along with CMS. The main goals of the ATLAS are precise measurements and tests of the standard model and QCD, Higgs boson discovery and search for the new phenomena like supersymmetry and exotic particles in pp collisions. Despite the fact that ATLAS was designed to study physics in the pp collisions, it can measure properties of relativistic heavy-ion collisions very well [59]. The design of the detector, driven by the properties of collisions provided by the LHC and above mentioned goals, had to fulfill the following set of requirements:

- fast, radiation-hard electronics and sensors and high detector granularity
- large acceptance in pseudorapidity with full coverage in azimuth
- good momentum resolution of charged particles and high efficiency in the inner tracker, vertex detectors close to the interaction point for offline tagging of b-jets and τ-leptons
- precise electromagnetic calorimetry for electron and photon measurement

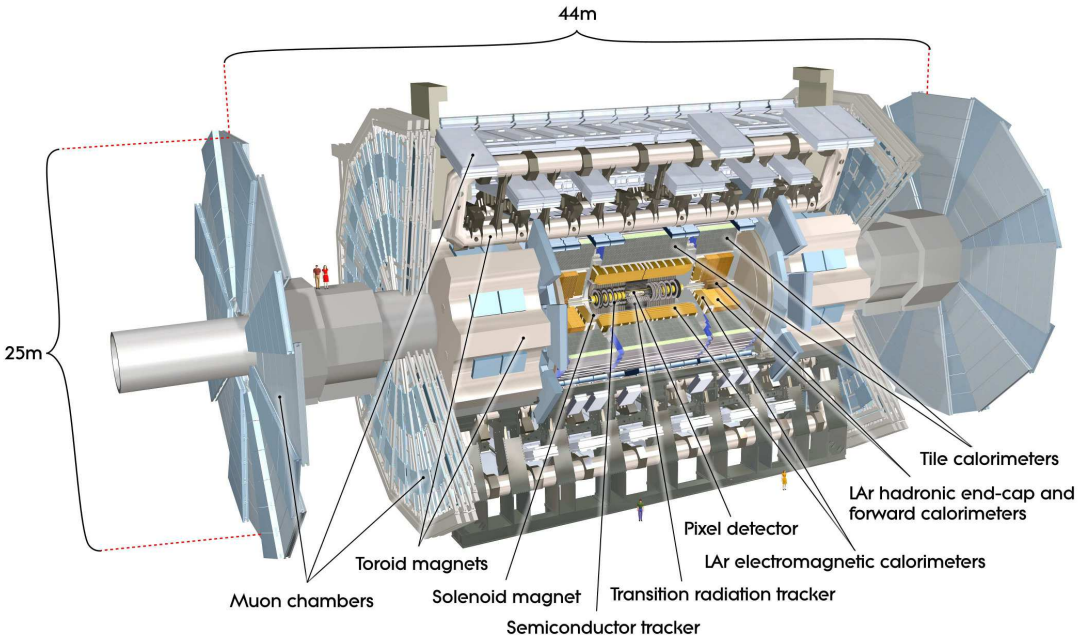

Figure 4.2: The overall view of the ATLAS detector. Figure adopted from [6].

and identification and large acceptance hadronic calorimetry for jet and missing transverse energy measurement

- good muon identification and momentum resolution
- highly efficient triggering to reduce the high collision rate from LHC

The design of the detector is forward-backward symmetric around the interaction point. The magnetic system consists of superconducting solenoid magnet in which inner tracker is immersed and three large superconducting toroids arranged with an eight-fold azimuthal symmetry around the calorimeters. The overall view of the ATLAS detector is in the fig. 4.2. The weight of the detector is approximately 7000 tonnes and the overall dimensions are 44 m in length and 25 m in height.

4.2.1 Tracking

The innermost part of the ATLAS is the inner tracker (or Inner Detector, ID) that measures tracks of the charged particles and consequently it provides information on their momentum as well as information on primary and secondary vertices. Since the density of tracks is very high on the LHC, the fine granularity of the tracking detectors is required. Inner tracker consist of three subdetectors: closest to the beampipe is the silicon pixel detector followed by the silicon microstrip tracker (SCT) backed by the Transition Radiation Tracker (TRT) that uses the technology of straw tubes. The whole ID is immersed in the 2 T magnetic field generated by the central solenoid which is 5.3 m long and has a diameter of 2.5 m. The view of the ID is in fig. 4.3.

The silicon detectors (pixel and SCT) cover the region $|\eta| < 2.5$. Both consist of barrel and end-cap parts, where in the barrel the detectors are composed of concentric cylinders around the beam axis while in end-cap it is composed of

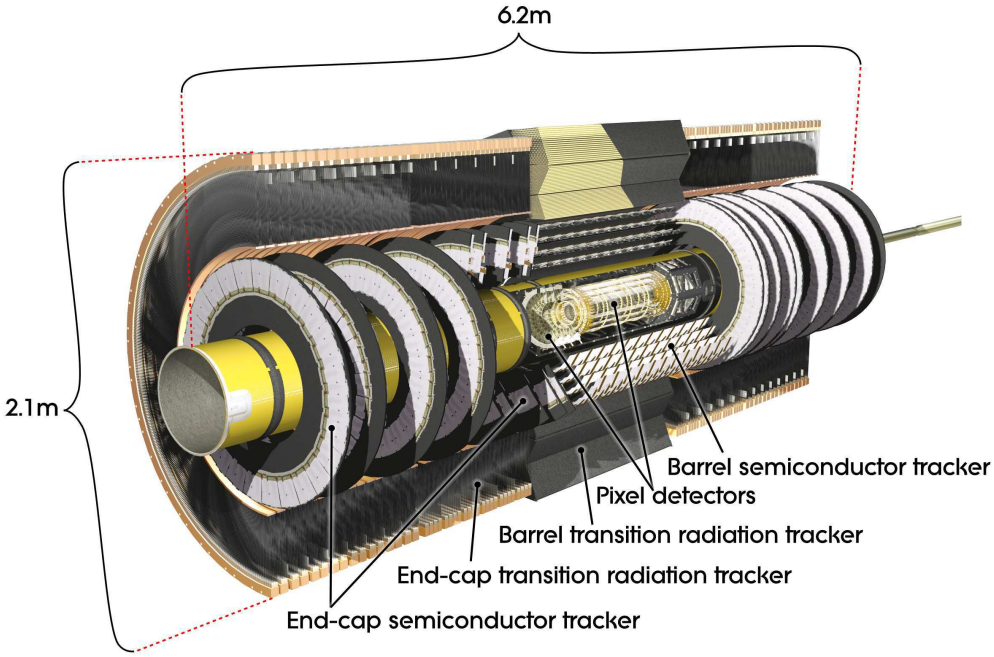

Figure 4.3: The view of the inner detector. Figure adopted from [6].

disks perpendicular to the beam axis. The pixel detector configuration is such that the particle emerging from interaction point typically crosses three layers, see fig. 4.4. All pixel modules are the same with segmentation in $R-\phi$ and z with minimum pixel size in $R-\phi \times z$ of $50 \times 400\,\mu\text{m}$ [2]. The total number of pixel readout channels is approximately 80.4 millions.

Eight active layers (four space points) of SCT is crossed by particles. In the barrel region the detector uses small-angle stereo strips to measure both coordinates with one set of strips parallel to the beam direction (measuring $R-\phi$). The pitch is $80\,\mu\text{m}$. In the end-cap region, the detectors have a set of strips running radially and a set of stereo strips at an angle of 40 mrad. Total number of readout channels of SCT is approximately 6.3 million. A large number of hits is provided by TRT, typically 36 hits per track. TRT covers region of four units of pseudorapidity $|\eta| < 2.0$.

The TRT provides information only on the $R-\phi$, in the barrel region the straws are parallel to the beam axis and in the end-cap region the straws are arranged radially in wheels. The number of TRT readout channels is 351,000. Because of the very high occupancy the TRT subdetector is usually not used in Pb+Pb collisions.

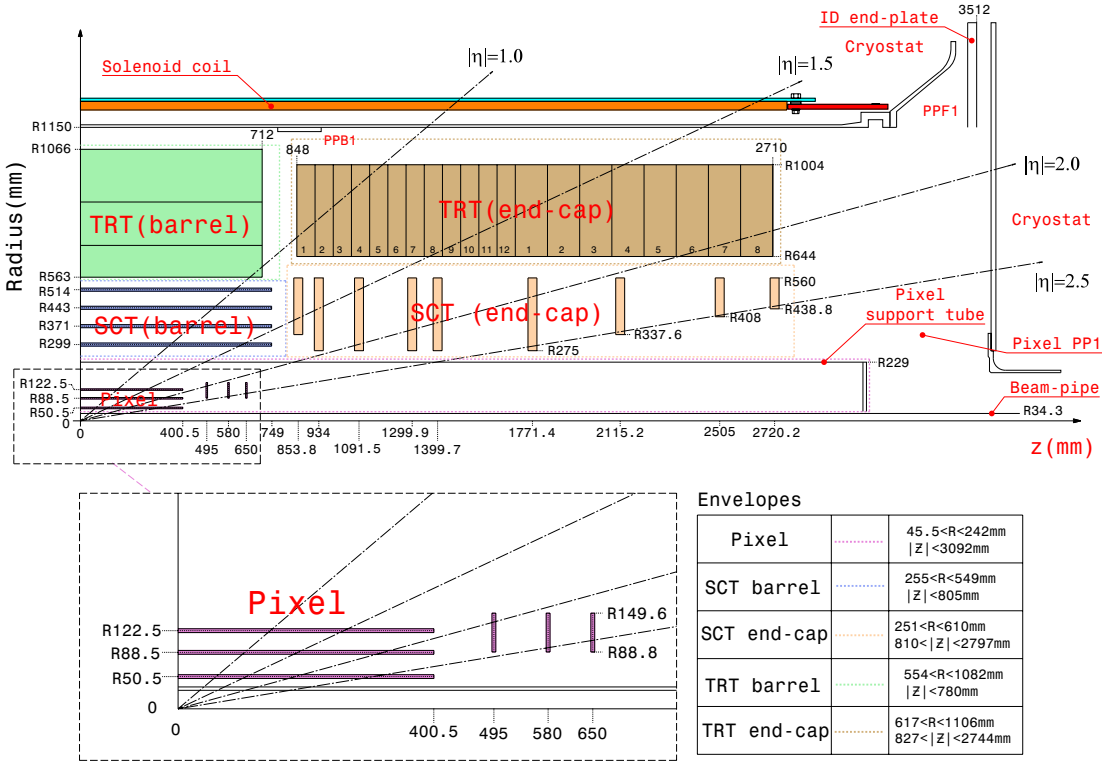

Figure 4.4: View of the quarter of the ATLAS inner detector showing the major detector elements. Figure adopted from [6].

4.2.2 Calorimetry

The calorimeter system of ATLAS detector consist of electromagnetic and hadronic calorimeters which cover almost ten units of pseudorapidity $|\eta| < 4.9$. The overall view of the calorimeter system is in Figure 4.5.

EM calorimeter is divided into barrel and end-cap parts covering $|\eta| < 1.475$ for barrel and $1.375 < |\eta| < 3.2$ for end-cap. The part of the EM calorimeter that matches the acceptance of the ID has fine granularity for the precise measurement of the photons and electrons while the rest of the calorimeter has somewhat coarser but sufficient granularity for the jet reconstruction and measurement of the missing energy $E_{\mathrm{T}}^{\mathrm{miss}}$. The EM calorimeter is a lead-LAr detector with kapton electrodes and lead absorber plates over its full coverage. The barrel part is divided into two half barrels at $z = 0$, end-caps are divided into two coaxial wheels covering $1.375 < |\eta| < 2.5$ and $2.5 < |\eta| < 3.2$. A presampler detector is in front of the calorimeter in $|\eta| < 1.8$ region to correct for the energy lost upstream of the calorimeter. In the region of precision measurement the calorimeter is segmented into three layers in depth with first two layers having fine granularity, while at larger rapidity ($|\eta| > 2.5$) there are two layers in depth. The total thickness of the Electromagnetic (EM) calorimeter is > 22 radiation lengths (X_0) in the barrel and > 24 in the end-caps.

The tile calorimeter is hadronic calorimeter using steel as the absorber and scintillating tiles as the active material. It consists of barrel ($|\eta| < 1.0$) and two extended barrels ($0.8 < |\eta| < 1.7$) which are placed directly outside the EM calorimeter. The tile calorimeter is divided into 64 segments azimuthally and into three layers radially. The total detector thickness at the outer edge is $9.7\,\lambda$

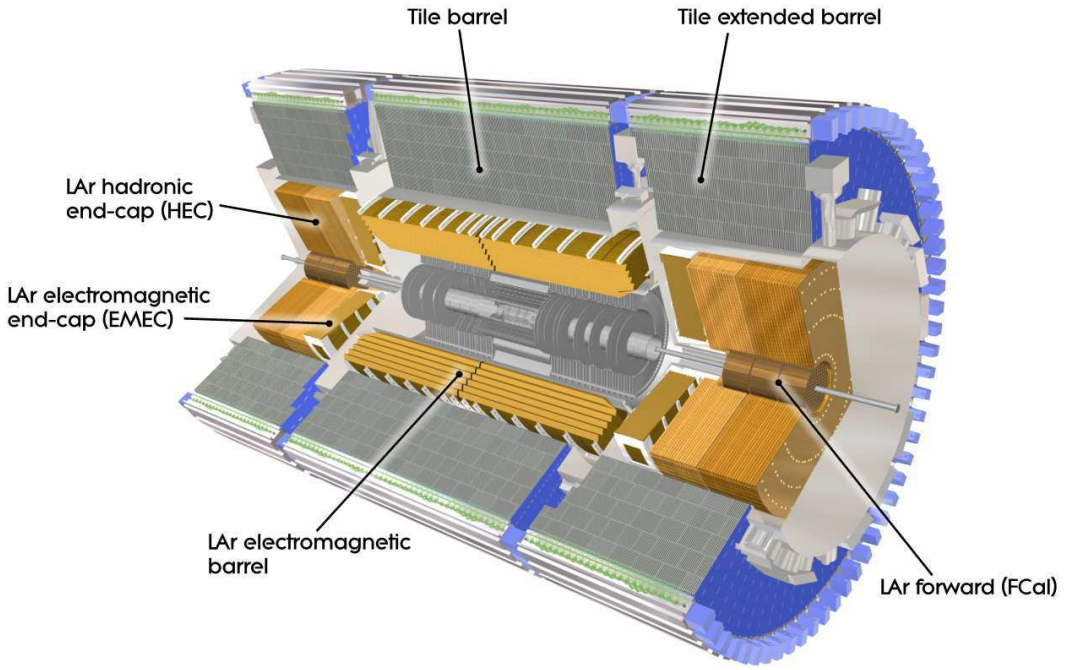

Figure 4.5: Cut-away view of the ATLAS calorimeter system. Figure adopted from [6].

at $\eta = 0.0$.

The Hadronic End-cap Calorimeter (HEC) uses copper as the absorber and liquid argon as active medium. It is located behind the end-cap electromagnetic calorimeter and it uses of two independent wheels per end-cap. The η range is $1.5 < |\eta| < 3.2$ so that it overlaps with part of the tile calorimeter on one side and the Forward Calorimeter (see below) on the other side. Each wheel is built from 32 identical wedge-shaped modules, each module divided into two segments in depth.

The Forward Calorimeter (FCal) is placed in the same cryostats as the end-cap calorimeters close to the beam pipe providing coverage $3.1 < |\eta| < 4.9$. The FCal is divided into three modules in each end-cap - first made of copper is optimised for electromagnetic measurements, the other two, made of tungsten, measure predominantly the energy of hadronic component. The high particle fluxes in this part of the detector require the solution with small liquid-argon gaps. In heavy-ion collisions energy depsited in FCal is used to determine the centrality of the collision as described in section 2.2.

4.2.3 Muon system

The overview of the muon system is in fig. 4.6. The important role in detection of the muons plays the magnetic field. In ATLAS muon system the magnetic deflection is provide by two magnet systems: for $|\eta| < 1.4$ magnetic bending is provided by the large barrel toroid, for $1.6 < |\eta| < 2.7$ muon tracks are bent by two smaller end-cap magnets. For tracks in $1.4 < |\eta| < 1.6$ magnetic deflection is provided by a combination of barrel and end-cap fields. This configuration

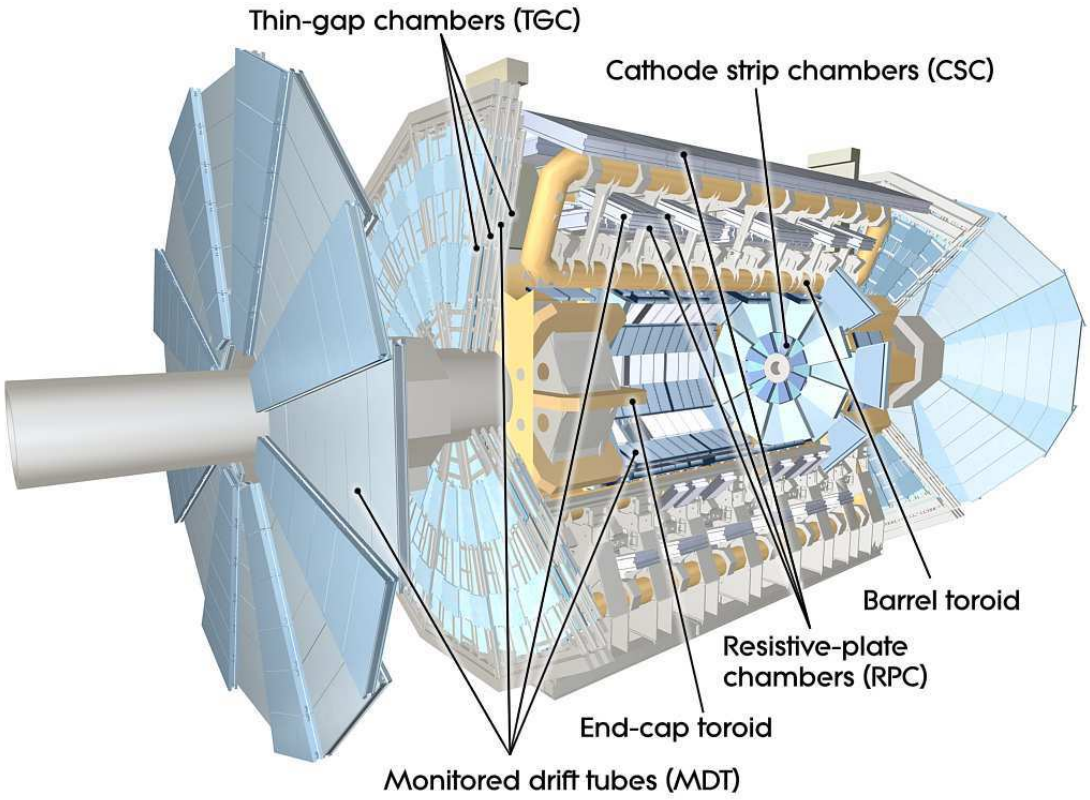

Figure 4.6: View of the ATLAS muon system. Figure adopted from [6].

provides a field that is mostly orthogonal to the muon trajectories.

The Monitored Drift Tubes (MDT's) are used over the $|\eta| < 2.7$ range to detect muon tracks (except the innermost layer which covers $|\eta| < 2.0$). For $2 < |\eta| < 2.7$ the Cathode Strip Chambers (CSC's), which are multiwire proportional chambers with cathodes segmented into strips, are used.

The trigger system for muons covers the pseudorapidity range $|\eta| < 2.4$. Resistive Plate Chambers (RPC's) are used in the barrel and Thin Gap Chambers (TGC's) in the end-cap regions. These detectors also measure the muon coordinate in the direction orthogonal to that determined by the MDT's and CSC's.

4.2.4 Forward Calorimeters

Apart from the detectors mentioned above there are another detectors in the very forward region. These are LUCID, ZDC, ALPHA and recently installed AFP. We will briefly mention only ZDC here because of it's importance for the heavy-ion collisions.

ZDC is a shortcut for the Zero Degree Calorimeters. They are located ± 140 m from the interaction point where the LHC beam-pipe is divided into two separate pipes in a configuration such that only the neutral particles produced at the interaction region can reach this calorimeter [60]. The pseudorapidity range they cover is $|\eta| > 8.3$. The ZDC uses tungsten as a absorber and quartz rods as a active media. The ZDC is both longitudinally and transversely segmented thus providing information on energy and position of the incident particles. Both arms of the ZDC are segmented into four layers - first one being designed and used

for electromagnetic calorimetry while the remaining three serve as a hadronic calorimeter. ZDC is very important for the heavy-ion collisions as it can measure the spectator neutrons dissociated from the colliding nuclei. This is crucial for ultra-peripheral collisions where usage of the ZDC is the only way how to trigger this type of collisions due to the very low activity in the mid-rapidity region.

5. Jet Reconstruction in HI collisions

In heavy-ion collisions, a large amount of energy is produced predominantly in the form of soft particles created in the soft scatterings and during the hadronization of QGP. When analyzing hard processes in HI collisions, this soft part of the collision is usually called underlying event (UE). Because of the large UE energy created in the collisions of two Pb nuclei, the jet reconstruction requires usage of specific algorithms to account for the UE energy deposited in the region of the jet. The heavy-ion group developed and implemented special subtraction procedure that subtracts the UE energy from all calorimeter cells on the event-by-event basis. Cells are clustered into the calorimeter towers which are then clustered with the anti-k_t algorithm. The MC derived calibration, called numerical inversion, is then applied to the reconstructed jets to account for the response of the calorimeter. Uncertainty of the jet energy scale (JES) was estimated by the procedure called cross-calibration that compares jets reconstructed by HI jet algorithms to the jets reconstructed by algorithms developed for *pp* collisions. The various stages of the reconstruction chain are briefly described below.

5.1 Subtraction

The input of the clustering algorithm used for HI jets are $\Delta\eta \times \Delta\phi = 0.1 \times \frac{\pi}{32}$ logical towers assembled from the energy deposits in the calorimeter cells. For each cell in the tower, the subtraction of the transverse energy is applied according to

$$E_{\mathrm{T}}^{\mathrm{subtr}} = E_{\mathrm{T}}^{\mathrm{cell}} - \rho(\eta^{\mathrm{cell}}, \phi^{\mathrm{cell}}) A^{\mathrm{cell}} \{1 + 2v_2 \cos[2(\phi - \Psi_2)]\} \tag{5.1}$$

where $E_{\mathrm{T}}^{\mathrm{cell}}$ is the transverse energy before the subtraction, $\rho(\eta^{\mathrm{cell}}, \phi^{\mathrm{cell}})$ is the average energy density in cells coordinates, A^{cell} is area of a cell and the expression in the braces accounts for the azimuthal modulation due to the elliptic flow. Because jets can influence the estimated transverse energy density, the iterative procedure is used to exclude jet areas from the ρ estimation.

5.2 Numerical Inversion for heavy ion jets

The subtraction of the underlying event and usage of calorimeter towers are significantly different from *pp* jet reconstruction algorithm where no subtraction of this type is used and calorimeter cells are clustered into topological clusters instead of calorimeter towers. Thus, it is necessary to derive HI specific numerical inversion (NI), a method that calibrates jets from the EM scale (explained below) to the final hadronic scale. Moreover, the NI should be derived independently for different centre-of-mass energies because the relative fraction of jets fragmenting from quarks to jets fragmenting from gluons differs between different centre-of-mass energies. Different quark-to-gluon ratio implies the change in calorimeter response to jets due to the difference in the structure of the jets. To suppress the contribution from the UE, the HI group uses small R jets (down to $R = 0.2$) in

many analyses that are not supported by the *pp* calibration. This makes another reason to implement NI procedure specifically for HI jets and derive HI specific NI constants. The method described in this chapter was used by HI group for *pp* and Pb+Pb data at 2.76 TeV, *p*+Pb data at 5.02 TeV and *pp* data at 8 TeV. Altogether four versions of NI constants were derived and tested depending on the centre-of-mass energy and collision system. These calibrations were used in some of the jet measurements mentioned in section 3.4 [53, 55], in jet fragmentation measurement presented in chapter 6 and in several more [61, 62, 63, 64].

5.2.1 Method

Numerical Inversion calibration derived to calibrate HI jets was inspired by the same procedure used in *pp* collisions. This calibration was derived for jets reconstructed at the so called EM scale. That means that the jets are clustered from calorimeter towers (or topological cluster in case of *pp* jets) which are calibrated to correctly measure energy from particles produced in electromagnetic showers. To correct to the final hadronic scale the calibration has to be applied due to the non-compensating character of the ATLAS calorimeters. The calibration is derived using Monte Carlo samples that are described in the next subsection. For Pb+Pb collisions, only peripheral events were used since the UE activity is significantly smaller in these. For *p*+Pb and *pp* events no selection on the centrality of events was made.

Response $\mathcal{R}$, is defined as the ratio of the transverse momentum of the jet reconstructed at the EM scale and corrected with additional corrections (see section 5.2.3) to truth transverse momentum $\mathcal{R} = p^{\mathrm{EM}}_{\mathrm{T,calo}}/p_{\mathrm{T,truth}}$. Response is evaluated for all calorimeter jets which match to truth jets within $\Delta R = \sqrt{\Delta\eta^2 + \Delta\phi^2} = 0.3$. Jets are required to be isolated, that means no other jet is present within $\Delta R < 2.5R$ for truth jets and within $\Delta R < 1.5R$ for reconstructed jets where R is the radius of clustering algorithm. For each bin in η_{det} and $p_{\mathrm{T,truth}}$ response distribution is fitted by a gaussian function. For details about fitting of these distributions see section 5.2.4. Mean Response $\langle\mathcal{R}\rangle$ is then defined as the mean of the Gaussian fit. Mean reconstructed energy is then $\langle p^{\mathrm{EM}}_{\mathrm{T,calo}}\rangle = \langle\mathcal{R}\rangle p_{\mathrm{T,truth}}$. Pairs $(\langle p^{\mathrm{EM}}_{\mathrm{T,calo}}\rangle, \langle\mathcal{R}\rangle)$ form points that are fitted for each η bin by function parametrized as

$$F_{\mathrm{calib}}(p^{\mathrm{EM}}_{\mathrm{T,calo}}) = \sum_{i=0}^{N_{\mathrm{max}}} a_i \left(\ln(p^{\mathrm{EM}}_{\mathrm{T,calo}})\right)^i, \tag{5.2}$$

where N_{max} is equal one or two. The N_{max} is chosen to provide best χ^2/NDF ratio. Having the fit of the response, the jets are calibrated via relation

$$p^{\mathrm{EM+NI}}_{\mathrm{T,calo}} = \frac{p^{\mathrm{EM}}_{\mathrm{T,calo}}}{F_{\mathrm{calib}}(p^{\mathrm{EM}}_{\mathrm{T,calo}})}. \tag{5.3}$$

The outcome of the NI procedure was the root file with histograms that store parameters a_i. When calibrating jets, these parameters were read out from the file and used for jet calibration according to formula (5.3).

collisions	dataset pattern
pp 2.76 TeV	mc12_2TeV*Pythia_AUET2BCTEQ6L1_jetjet_JZ*R04.merge. NTUP_HI.e2201_s1647_s1586_r4895_p1597
pp 8 TeV	mc12_8TeV*Pythia8_AU2CT10_jetjet*merge. NTUP_JETMETWZ.e1126_s1469_s1470_r3658_p1666
Pb+Pb 2.76 TeV	mc11_2TeV*pythia_jetjet.recon.NTUP_HI.e1296_d724_r4789
p+Pb 5.02 TeV	mc12_5TeV*Pythia_AUET2BCTEQ6L1_jetjet*.recon. NTUP_HI.e2166_d814_r5069
p+Pb 5.02 TeV*	mc12_5TeV*Pythia_AUET2BCTEQ6L1_jetjet*MaxEta_m3p0.recon. NTUP_HI.e2166_s1675_s1586_r4893

Table 5.1: Name patterns of the MC datasets for various types of collisions. In the last row the special forward enhanced samples for p+Pb collisions are listed.

5.2.2 MC samples

Because of the steeply falling jet spectrum the generation of jet samples would be extremely inefficient if done in one go. MC samples generated for jet studies thus have to be divided into several JX subsamples (with X between 0 and 5) each with a fixed range set on the $p_{\mathrm{T}}^{\mathrm{min}}$ and $p_{\mathrm{T}}^{\mathrm{max}}$ in the hard scattering. To get unbiased results these samples have to be later combined using cross-section (obtained from the MC generator) weighting. It was checked that the resulting spectra are smooth and have correct shape. Concrete MC samples used in the derivation of mentioned NI calibration constants are listed in Table 5.1.

The MC samples used for the derivation of the NI constants in Pb+Pb collisions at $\sqrt{s_{\mathrm{NN}}} = 2.76\,\mathrm{TeV}$ are PYTHIA6 [65] dijet events embedded into the real minimum bias (MB) Pb+Pb events. Pb+Pb MB data were collected during 2011 data taking period. Only peripheral events with centrality between 60-80% were used to avoid potential bias due to the worsening of the jet energy resolution (JER) in central collisions.

The MC samples used for derivation of the NI constants in p+Pb collisions at $\sqrt{s_{\mathrm{NN}}} = 5.02\,\mathrm{TeV}$ are PYTHIA6 dijet events. Since the samples of the PYTHIA6 events embedded into the real MB p+Pb events were broken with the software bug, we were forced to use signal only samples. Because in p+Pb collisions we are interested also in low p_{T} physics in the forward region we needed to have reliable NI constants for large η. Since usual MC samples do not have sufficient statistics in the forward region we used special samples where events were filtered to have at least one jet in the forward region.

The MC samples used for derivation of the NI constants in pp collisions at $\sqrt{s_{\mathrm{NN}}} = 2.76\,\mathrm{TeV}$ are PYTHIA6 dijet events with low pile-up contamination to simulate conditions in real collisions.

The MC samples used for derivation of the NI constants in pp collisions at $\sqrt{s_{\mathrm{NN}}} = 8\,\mathrm{TeV}$ are PYTHIA8 dijet events with low pile-up contamination to simulate conditions in real collisions. This calibration was used by HI group only for cross-calibration study, no physics results were obtained with this calibration.

5.2.3 Additional corrections

Some additional corrections were applied at the EM scale to correct for imperfections in the jet reconstruction. One of these is the so called Self Energy Bias (SEB) correction. At the time when subtraction procedure is performed, the algorithm cannot decide which jets are fakes and which correspond to the real jet signal coming from a hard process. The decision whether jet is a fake or not is in subtraction procedure based on the ratio between maximum and average tower E_{T} in the jet. This can be improved in the offline analysis where the discrimination can use the matching to track jets or EM clusters. Thus, it can happen that the jet that is fake and belongs to the UE is excluded from the UE density estimation during the online subtraction procedure and vice versa. This is corrected at the offline level by the SEB correction.

Second correction is the so called eta-phi correction that corrects for the non-uniformity of the jet reconstruction in the $\eta - \phi$ plane which is caused by the dead modules and non-uniformity in the calorimeter system. These corrections were applied on standard reconstructed jets that the HI jet group uses.

5.2.4 Gaussian fits

As already mentioned, distribution of response is fitted in each η and $p_{\mathrm{T,truth}}$ bin by Gaussian function. This distribution was fitted separately for each JX sample to suppress statistical fluctuations caused by poor statistics in samples with high weight. The fit range was truncated at the lower side to suppress bias due to finite jet reconstruction efficiency. The truncation was p_{T} dependent. Two examples of the fits are shown in Figure 5.1.

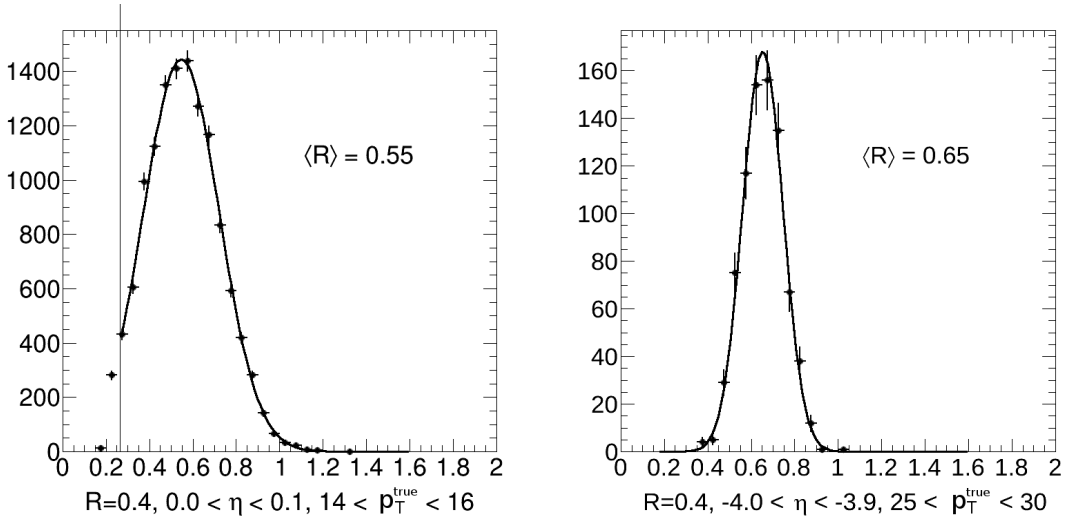

Figure 5.1: Two examples of the response distributions in given $p_{\mathrm{T,true}}$ bins along with gaussian fits and the resulting mean response. Left: an example of the fit from NI procedure for pp at 8 TeV, J1 sample, $R = 0.4$ jets in the midrapidity region. The truncation of the fit range is visible. Right: an example from NI procedure for p+Pb collisions at 5.02 TeV, J1 forward enhanced sample, $R = 0.4$ jets in the forward region.

5.2.5 Response fits

As was mentioned earlier, response dependence on the transverse momentum at the EM scale was fitted by the polynomial of logarithms. The best results were achieved if the maximal order of the polynomial was set to two. Higher order polynomials were prone to overfit the data - the fit functions accommodated to fluctuations and noise but were not catching the trend correctly. Response was thus fitted twice and the function that provided best χ^2/NDF ratio was chosen as a calibration function. Due to the efficiency bias, which is not fully eliminated by the gaussian fitting, we had to exclude few lowest p_{T} points from the fitting range. The fitting range was dependent on the type of collisions and η bin. Four examples of the fits are shown in Figure 5.2.

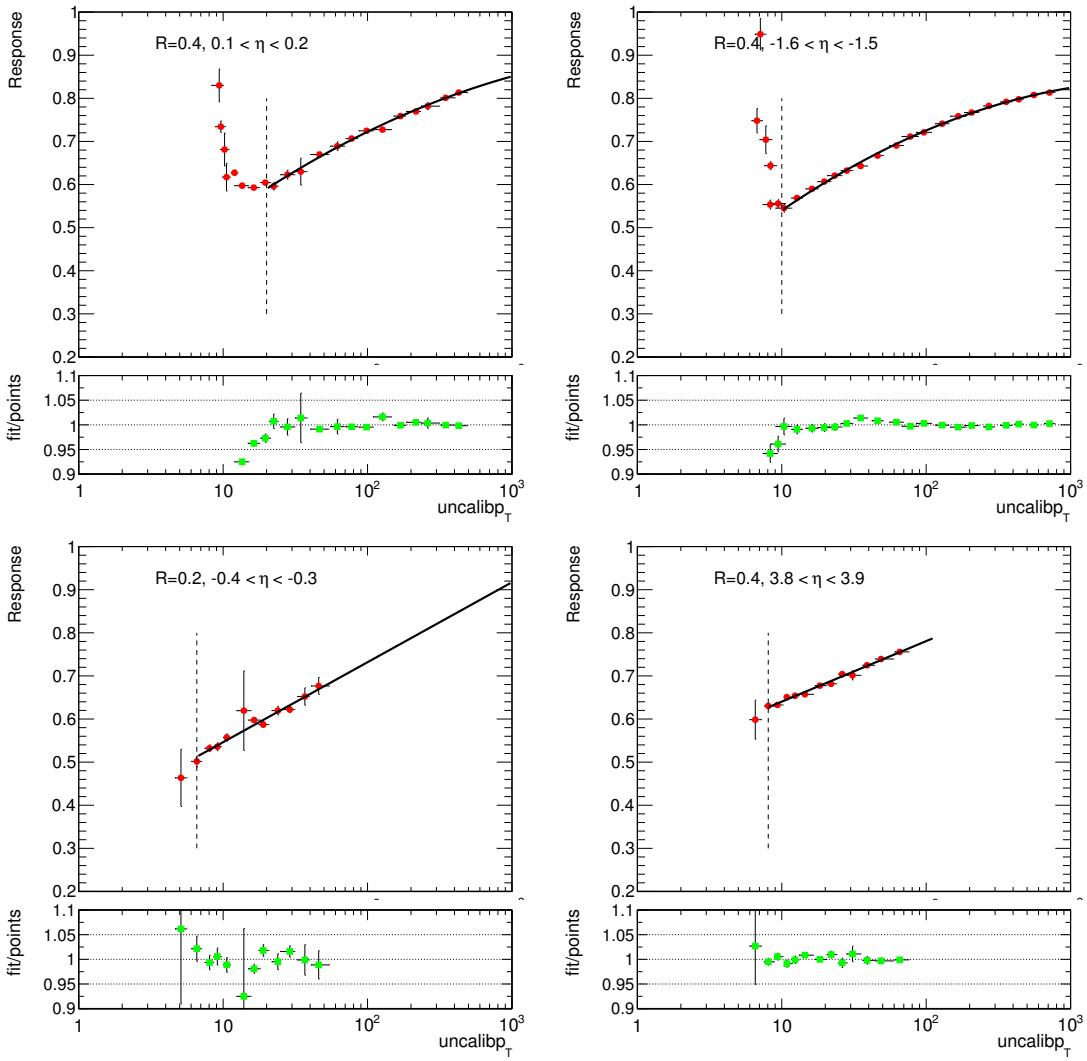

Figure 5.2: Four examples of the response fits. Upper left plot: $R = 0.4$ jets, Pb+Pb MC at $\sqrt{s_{\mathrm{NN}}} = 2.76\,\mathrm{TeV}$, midrapidity region. Upper right plot: $R = 0.4$ jets, pp MC at $\sqrt{s} = 8\,\mathrm{TeV}$, $-1.6 < \eta < -1.5$. Lower plots: both are from p+Pb MC at $\sqrt{s_{\mathrm{NN}}} = 5.02\,\mathrm{TeV}$, left one is midrapidity region, right one is from forward region.

5.2.6 Closure Tests

To check whether the NI works correctly, NI calibration constants were tested on the same MC sample they were derived from. This check is usually called closure test as it compares transverse momentum of reconstructed and fully calibrated jets to the transverse momentum of truth jets. The matching and selection criteria were the same as when deriving the NI constants. The variable that we use to quantify the closure is defined as $(p_{\mathrm{T}}^{\mathrm{reco}} - p_{\mathrm{T}}^{\mathrm{truth}})/p_{\mathrm{T}}^{\mathrm{truth}}$ and we call that jet energy scale (JES). We evaluated JES in the p_{T} bins by fitting truncated gaussians to the distribution which at low p_{T} is affected by the cut on the p_{T} of the reconstructed jets. We did closure test for each set of NI constants. An example of the results for $R = 0.4$ jets can be seen in Figure 5.3. The non-closure (deviation from zero) for higher p_{T} is less than 1%. At low p_{T} the efficiency bias plays an important role in deteriorating expected closure. Figure 5.4 shows the difference in JES between central and peripheral collisions in Pb+Pb collisions. The difference is negligible for majority of the kinematic region except for the lowest p_{T} bins which is due to the lower efficiency of the jet reconstruction in central collisions that amplifies the efficiency bias.

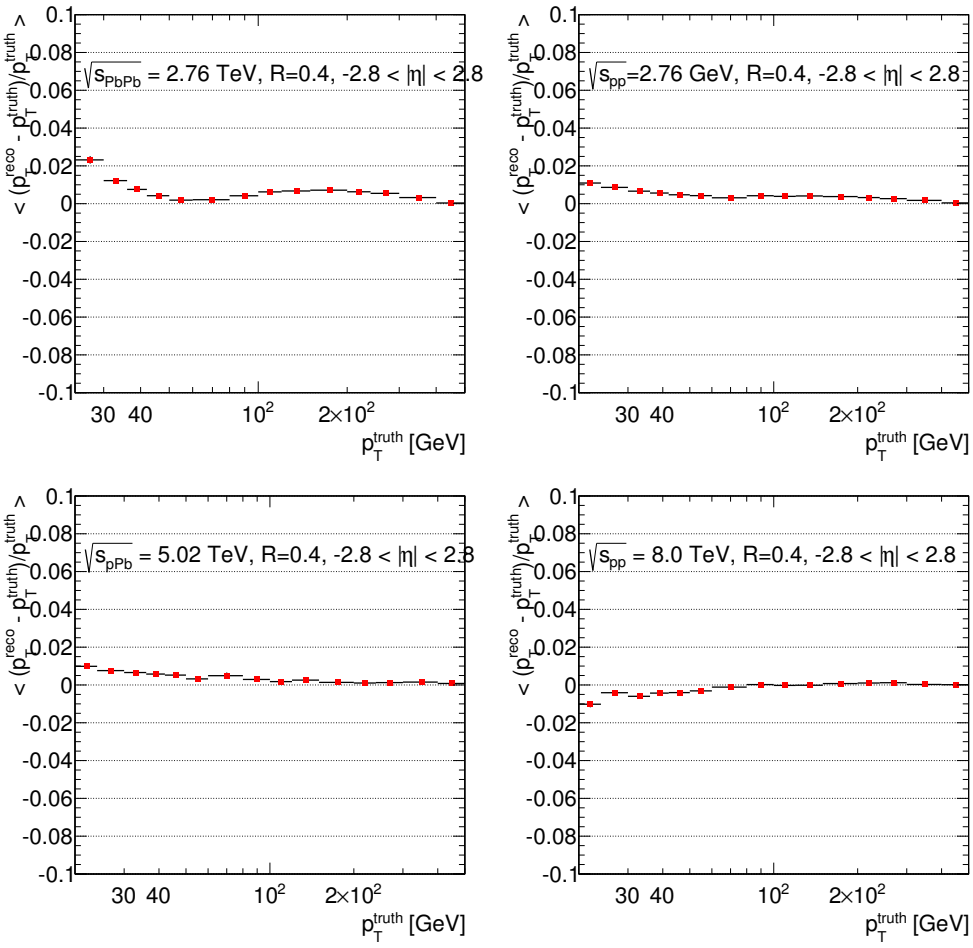

Figure 5.3: Plots showing the results of the closure test for various types of collisions.

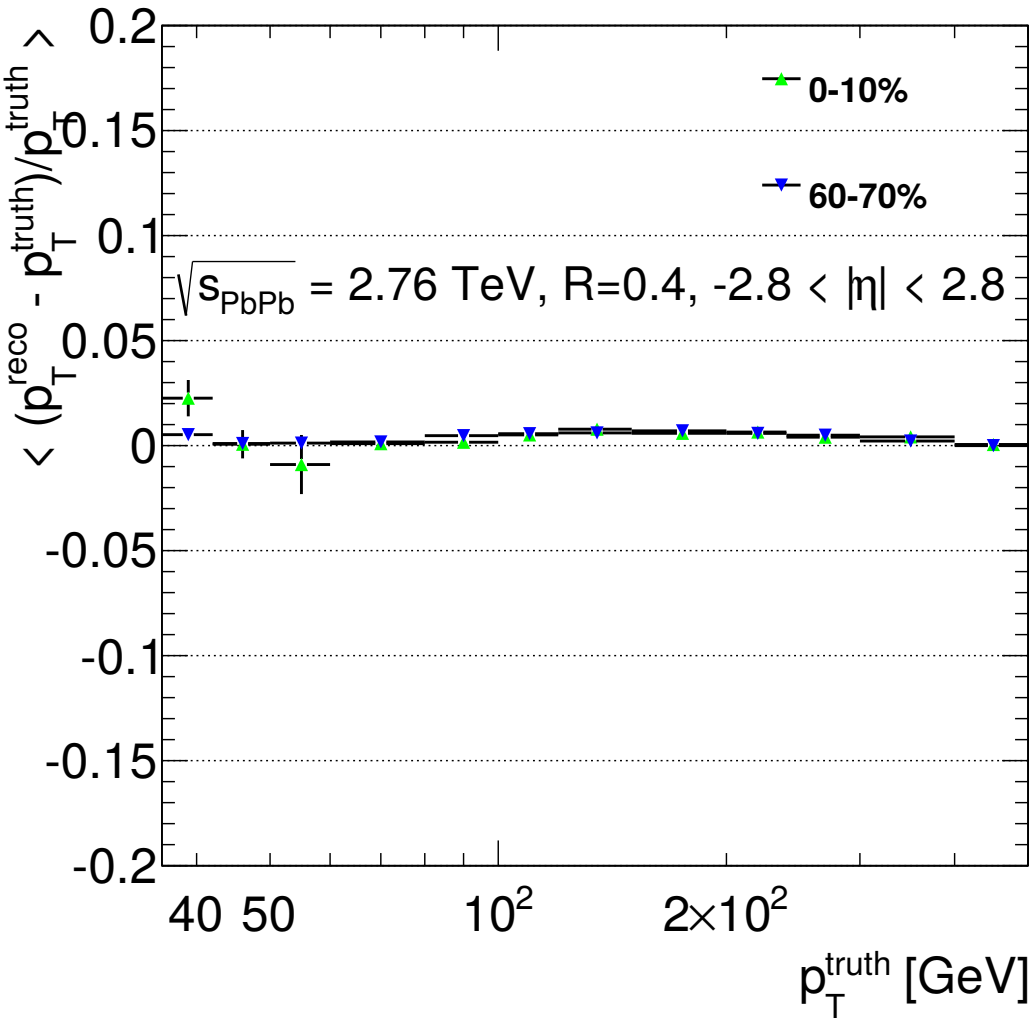

Figure 5.4: Results of the closure test for Pb+Pb collisions showing difference between central and peripheral collisions.

5.3 Cross-calibration

The performance of the jets used in *pp* collisions (EM+JES jets) is well understood and documented [66, 67]. The performance of the jet calibration is tested using independent objects like photons or Z bosons that are recoiling against the jets - the transverse momentum of the jet is compared to the transverse momentum of the recoiling object. The ratio of the two transverse momenta is called response (important notice: this means something fundamentally different than the calorimeter response that was estimated by the numerical inversion procedure). The so called in-situ correction factors are derived based on the difference of the response in data and MC and the uncertainty of the jet energy scale is estimated. In heavy-ion collisions this is not possible to do because of the limited statistics in HI data and quenching of the jets which significantly reduces their momentum and thus distorts the momentum balance between jets and independent object. To derive the JES uncertainty of the HI jets, the jets that were

reconstructed with the *pp* algorithm and whose performance is well understood were used as a baseline - the HI jets were cross-calibrated by the *pp* jets. This means that the transverse momentum of the HI jets was compared to the transverse momentum of the *pp* jets which were in this case used as an independent and well understood reference objects. Now it was of course not required that the *pp* jets are recoiling against the HI jets but quite oppositely *pp* and HI jets were required to match each other. The absolute JES uncertainty of the HI jets is then composed from the baseline component which is the absolute *pp* jets JES uncertainty plus the component due to the cross-calibration procedure and the uncertainty caused by the flavor composition and response uncertainties of the HI jets [68].

To derive the cross-calibration factors the average response ratio between HI and *pp* (p_{T} of the *pp* jets is from now on labeled as $p_{\mathrm{T}}^{\mathrm{EM+JES}}$) jets $\langle p_{\mathrm{T}}^{\mathrm{HI}}/p_{\mathrm{T}}^{\mathrm{EM+JES}}\rangle$ was evaluated as a function of $p_{\mathrm{T}}^{\mathrm{EM+JES}}$ in several η bins in 2012 8 TeV data and corresponding MC simulations. The reciprocal of the ratio of the response $\langle p_{\mathrm{T}}^{\mathrm{HI}}/p_{\mathrm{T}}^{\mathrm{EM+JES}}\rangle$ in data and MC is the correct cross-calibration factor that is applied to the HI jets by rescaling the jet four-vectors. Two examples of the size of the response ratios, its p_{T} dependence and its uncertainties are shown in Figure 5.5.

To test the sensitivity of the cross-calibration to the jet flavor the additional studies were done in Z+jet and γ+jet events where fraction of jets that are produced by fragmentation of quarks is much higher than in the inclusive jet sample. The author of this thesis was working on the Z+jet study which is described in detail in the next section. The γ+jet analysis was done in an analogical way. The plot summarizing the $\langle p_{\mathrm{T}}^{\mathrm{HI}}/p_{\mathrm{T}}^{\mathrm{EM+JES}}\rangle$ distributions in different jet samples and MC is shown in Figure 5.6. The difference in p_{T} between HI and *pp* jets is coming mostly from the additional in-situ correction factors applied to *pp* jets which has the largest effect at low-p_{T}. The results also suggest that the cross-calibration is not dependent on the jet flavor because samples contained in the Figure has very different jet flavor composition. This suggests that cross-calibration is applicable to data taken at different $\sqrt{s}$ (and so having different jet flavor composition).

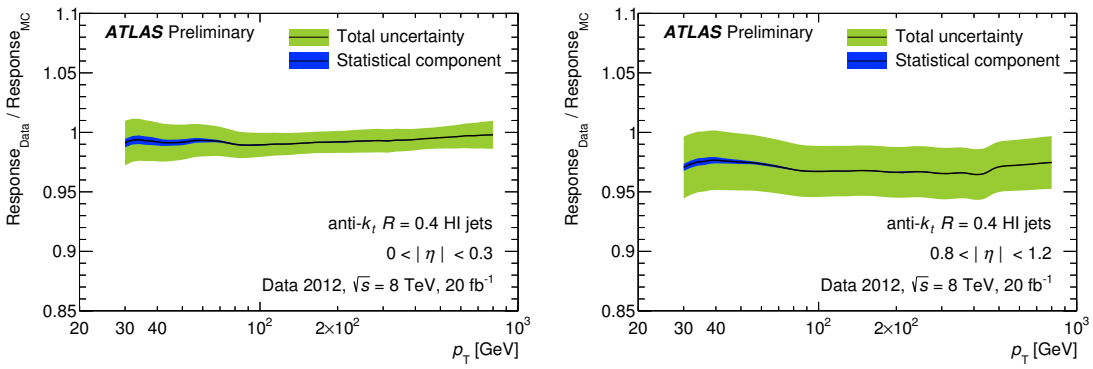

Figure 5.5: The cross-calibration factors as a function of p_{T} for various $|\eta|$ bins. The smoothed data-to-MC ratio is shown as a black line with the statistical and total uncertainties indicated by green and blue bands, respectively [68].

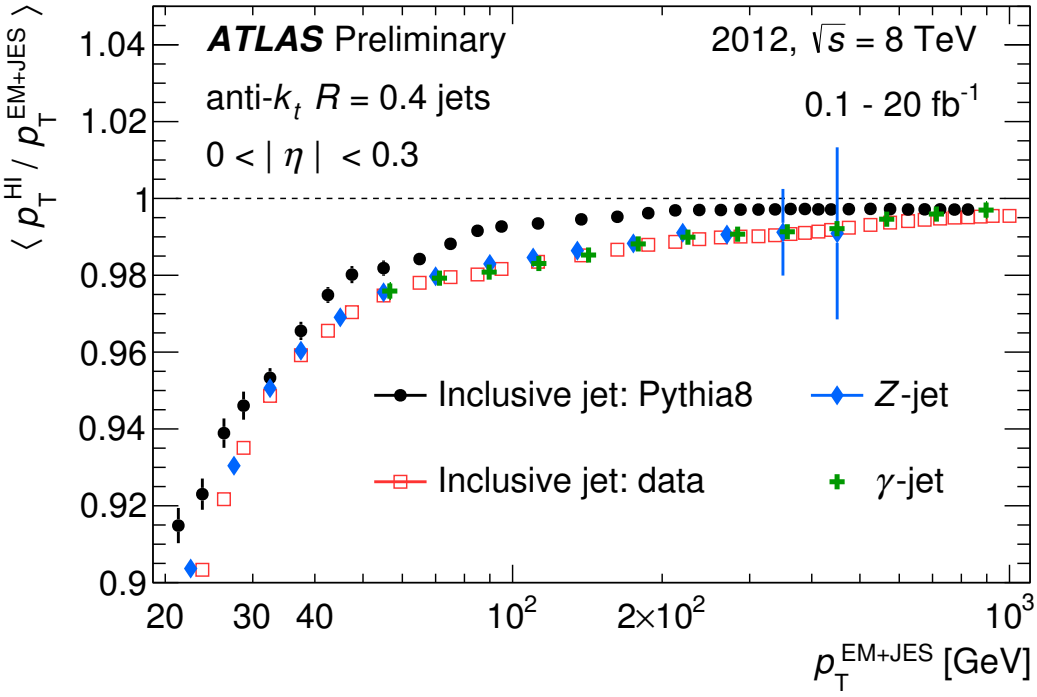

Figure 5.6: The $\langle p_{\mathrm{T}}^{\mathrm{HI}}/p_{\mathrm{T}}^{\mathrm{EM+JES}}\rangle$ as a function of $p_{\mathrm{T}}^{\mathrm{EM+JES}}$ for PYTHIA8 MC (black circles) and three separate data samples: inclusive jets (red squares), Z+jet (blue diamonds) and γ+jet (green crosses).

5.3.1 Z+jet study

In events with Z recoiling against (one) jet, the transverse momentum of the jet can be compared to the measured transverse momentum of Z, p_{T}^{Z}. The p_{T}^{Z} is reconstructed from the Z decay products, electrons or muons. The main goal of this study was to quantify differences between pp and HI jet reconstruction algorithms and subsequently to check the validity of the cross-calibration. The analysis was run over 2012 pp data taken at the center of mass energy $\sqrt{s_{NN}} = 8\,\mathrm{TeV}$, and integrated luminosity $\int \mathrm{L}\,\mathrm{dt} \approx 20\ \mathrm{fb}^{-1}$. Two samples containing $\mathrm{Z} \to ee$ and $\mathrm{Z} \to \mu\mu$ decays were analyzed separately.

Event Selection

The $Z \to ee$ events were selected using a dielectron trigger with a threshold of 12 GeV (`EF_2e12Tvh_loose1`). The $\mathrm{Z} \to \mu\mu$ sample was recorded using a single muon trigger with a threshold of 18 GeV (`EF_mu18_tight_mu8_EFFS`). After applying lepton cuts (see below) the invariant mass was calculated from the reconstructed pairs of leptons with opposite charge. If the reconstructed mass was in the required window $66 < m_{ll} < 106\,\mathrm{GeV}$ the Z boson four momentum was reconstructed by adding four momenta of the leptons.

To reject events in which direct balance between jet and Z is deteriorated by a presence of the other jet, the requirement on the next highest p_{T} jet is $p_{\mathrm{T}}/p_{\mathrm{T}}^{Z} < 0.2$ with minimal p_{T} of 12 GeV.

Leptons

The electrons were required to have $E_{\mathrm{T}}^{e} > 20\,\mathrm{GeV}$, $|\eta| < 2.47$ where the transition region between calorimeter sections $1.37 < |\eta| < 1.52$ has been excluded. The quality class of the electrons was medium.

Muons used in the analysis were combined muons [69] with $p_{\mathrm{T}}^{\mu} > 20\,\mathrm{GeV}$ in the pseudorapidity region of $|\eta| < 2.4$. The muons were required to have at least one Pixel hit, five SCT hits, number of Pixel and SCT holes less than three, succesful TRT extension where expected and good pointing to the reconstructed vertex. Muons were also required to pass isolation requirement.

Jets

Altogether three anti-k_t jet collections with $R = 0.4$ were used, two of them (LCTopo and topoEM) using pp jet reconstruction algorithms and one using HI jet reconstruction algorithm. The difference between pp jet collections is in the type of the calibration applied during reconstruction of topological clusters. The topoEM jet collection is reconstructed at the EM scale, described in section 5.2.1. LCTopo jets use the local cell signal weighting correction method that is based on cluster properties related to shower development [67]. Both jet collections are calibrated to the hadronic scale by the numerical inversion very similar to the HI specific numerical inversion described in section 5.2, though the size of the NI correction significantly differs between the two.

The p_{T} balance was calculated for all leading jets with $p_{\mathrm{T}} > 12\,\mathrm{GeV}$ in pseudorapidity region $|\eta| < 1.2$. To ensure that Z and recoiling jet were back to back they had to pass $\Delta\phi(\mathrm{jet}, \mathrm{Z}) > 2.9$ cut. pp jets had to fulfill jet quality criteria. To suppress pile-up contamination, pp jets were required to have jet vertex fraction (JVF) $|\mathrm{JVF}| > 0.25$. Since last two variables cannot be calculated for HI jets, they were required to match to pp jets. Furthermore the leading pp jets were required to be isolated from Z decay products, $\Delta R(\mathrm{jet}, \mathrm{electrons}) > 0.35$, $\Delta R(\mathrm{jet}, \mathrm{muons}) > 0.2$. The event entered analysis only if leading jets from all collections passed above mentioned cuts.

TopoEM and LCTopo jets were calibrated using standard pp JetCalibrationTool. In-situ correction was applied. The HI jets were calibrated using HI specific calibration tool with NI constants derived from PYTHIA8 MC events at $\sqrt{s_{NN}} = 8\,\mathrm{TeV}$.

Measurement of the p_{T} balance

To account for the additional parton radiation perependicular to the jet axis in the transverse plane, a new variable $p_{\mathrm{T}}^{\mathrm{ref}} = p_{\mathrm{T}}^{\mathrm{Z}} \times |\cos(\Delta\phi(\mathrm{jet}, \mathrm{Z}))|$ was constructed.

The mean response $\mathscr{R} = p_{\mathrm{T}}^{\mathrm{jet}}/p_{\mathrm{T}}^{\mathrm{ref}}$ and its error in given p_{T} and η bin were estimated by the truncated gaussian fit. This was done for every jet collection. Figure 5.7 shows the mean response $\mathscr{R}$ as a function of $p_{\mathrm{T}}^{\mathrm{ref}}$ from $\mathrm{Z} \to ee$ sample for both pp and HI jets in two η bins. Figure 5.8 shows the same but for $\mathrm{Z} \to \mu\mu$ events. In our study the in-situ corrections were applied to pp jets leading to the discrepancy between HI and pp jets which is more pronounced at low p_{T} where the relative size of the correction is largest. The discrepancy is observed also for jets with large $|\eta|$ where in-situ correction is larger as well.

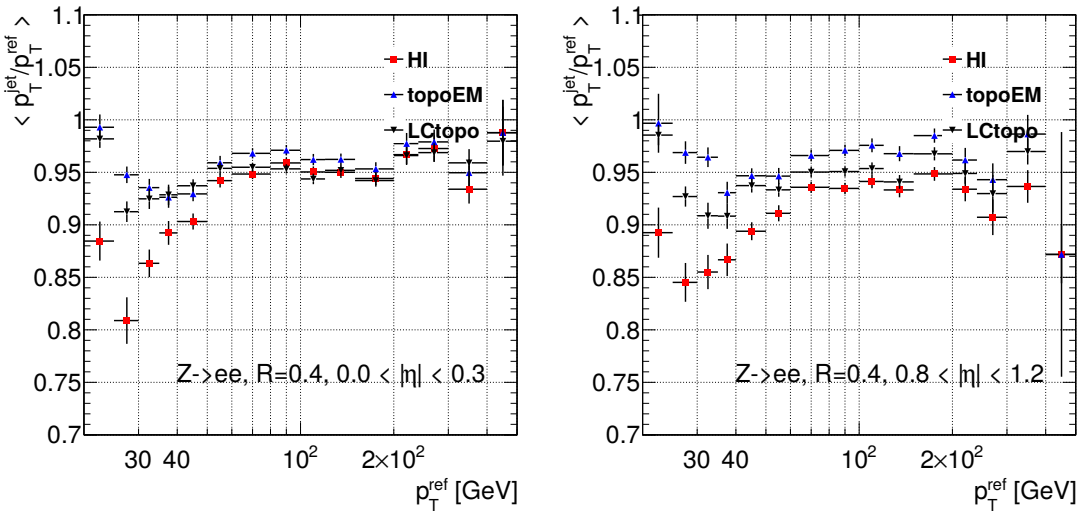

Figure 5.7: Mean response $\mathscr{R}$ as a function of $p_{\mathrm{T}}^{\mathrm{ref}}$ from Z $\rightarrow ee$ sample for two different η bins.

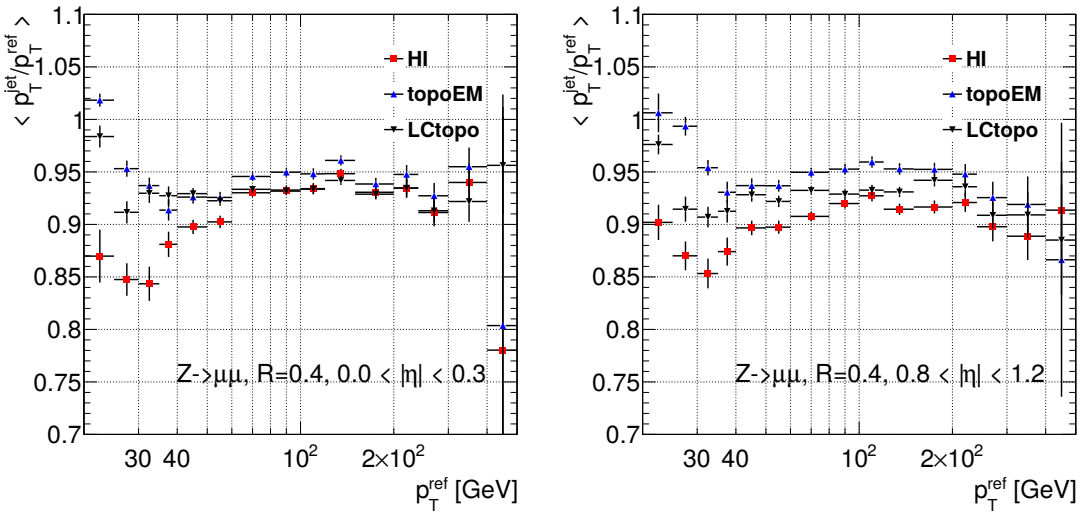

Figure 5.8: Mean response $\mathscr{R}$ as a function of $p_{\mathrm{T}}^{\mathrm{ref}}$ from Z $\rightarrow \mu\mu$ sample for two different η bins.

To better see the differences between HI and pp jets we compared directly the p_{T} of the jets. The mean response, now defined as $\mathscr{R}^{\mathrm{jet}} = p_{\mathrm{T}}^{\mathrm{HI}}/p_{\mathrm{T}}^{\mathrm{pp}}$ was again estimated by the truncated gaussian fit. Figures 5.9 and 5.10 show the mean response $\mathscr{R}^{\mathrm{jet}}$ as a function of $p_{\mathrm{T}}^{\mathrm{pp}}$ for topoEM and LCTopo $R = 0.4$ anti-k_t jets. The difference at low p_{T} and for most forward $|\eta|$ bin are most likely due to the in-situ correction applied to the pp jets. Also the differences in reconstruction and NI can make differences at low p_{T}. In midrapidity at higher p_{T} the HI jets are consistent with pp jets.

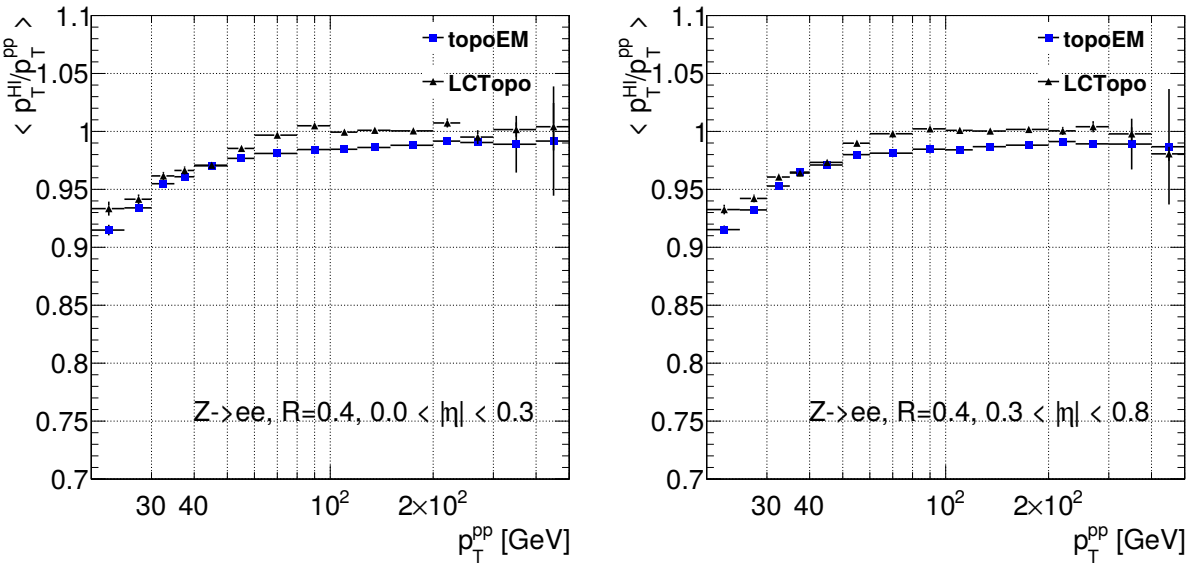

Figure 5.9: Mean response $\mathscr{R}^{\mathrm{jet}}$ as a function of $p_{\mathrm{T}}^{\mathrm{pp}}$ from Z $\rightarrow ee$ sample for two η bins.

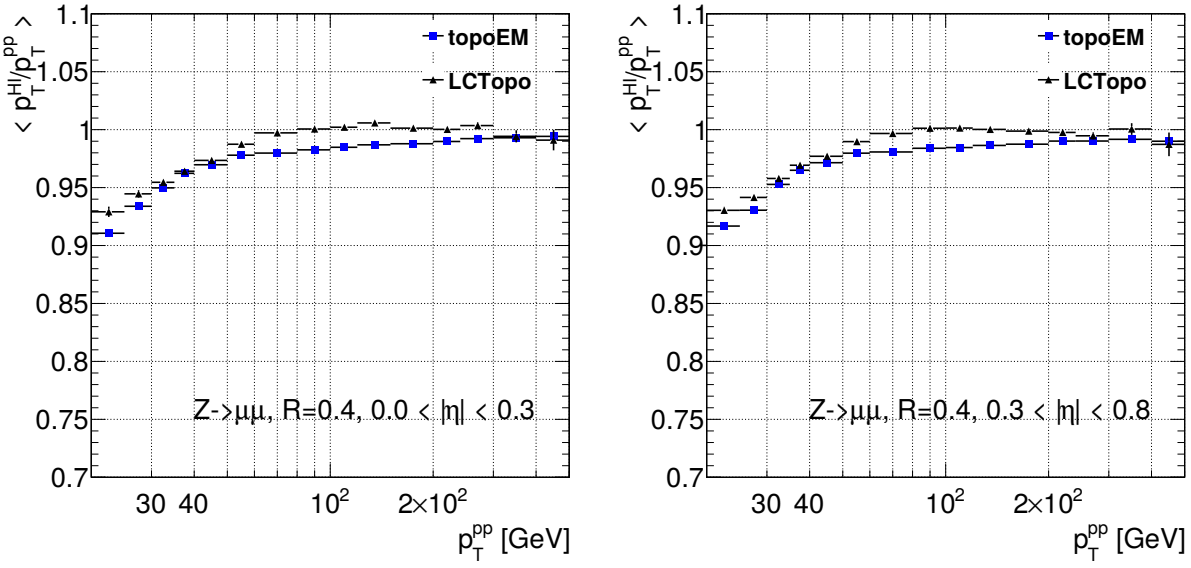

Figure 5.10: Mean response $\mathscr{R}^{\mathrm{jet}}$ as a function of $p_{\mathrm{T}}^{\mathrm{pp}}$ from Z $\rightarrow \mu\mu$ sample for two η bins.

5.4 JES uncertainty

The absolute JES uncertainty of the HI jets has following components [68]:

- baseline component,
- uncertainty of the cross-calibration procedure,
- flavor composition,
- response uncertainties of the HI jets.

Without going into much detail we will briefly discuss them below.

Baseline component is JES uncertainty of the *pp* jets (EM+JES) provided by the ATLAS JetEtMiss group. Uncertainty of the cross-calibration was derived by varying the selection of jets that enter the $\langle p_{\mathrm{T}}^{\mathrm{HI}}/p_{\mathrm{T}}^{\mathrm{EM+JES}}\rangle$ distributions. Uncertainty due to the different flavor composition of the data samples taken at different centre-of-mass energies was estimated by the same procedure that is used in every analysis of *pp* data that uses jets. This uncertainty was derived with the software tool provided by the JetEtMiss group.

The out-of-time pileup affects the shape of channel pulses in the calorimeter. When reconstructing these pulses the optimal filtering coefficients are adjusted to account for this effect. Because the different optimal filtering coefficients were used for the reconstruction of the *pp* data at $\sqrt{s} = 8\,\mathrm{TeV}$ (only sample with significant out-of-time pileup) than for the other data samples the calorimeter response could have been affected. The effect it had on the jet p_{T} was studied and the uncertainty due to that was derived for jets in *pp* at $\sqrt{s} = 2.76\,\mathrm{TeV}$ and p+Pb collisions.

Due to the difference in the calorimeter response between 2011, when Pb+Pb $\sqrt{s_{\mathrm{NN}}} = 2.76\,\mathrm{TeV}$ data were collected, and 2012/2013 data taking periods the data period uncertainty was established for HI jets in Pb+Pb collisions. This was based on the study of the sum of p_{T} of the tracks associated with the jet and jet p_{T} in Pb+Pb and *pp* collisions at $\sqrt{s_{\mathrm{NN}}} = 2.76\,\mathrm{TeV}$ and corresponding MC.

The jet response in Pb+Pb collisions can be affected by the jet quenching which significantly modifies the jet properties. This was studied by comparing the jet response in PYTHIA and Pyquen [70] MC generators. Parameters of the Pyquen generator were tuned to correctly describe the modifications of the jet fragmentation in the Pb+Pb data. No significant deviations of the jet response were found between the PYTHIA and Pyquen MC samples so the conservative constant 1% uncertainty was established for central collisions which linearly decreases as a function of centrality percentile down to 0% for peripheral collisions.

Examples of the derived JES uncertainties and sizes of their components are in Figure 5.11 (2013 *pp* collisions at $\sqrt{s} = 2.76\,\mathrm{TeV}$) and Figure 5.12 (2011 Pb+Pb collisions at $\sqrt{s_{\mathrm{NN}}} = 2.76\,\mathrm{TeV}$). These uncertainties were used to estimate the JES systematic uncertainty of the measurement of jet fragmentation functions presented in the next chapter.

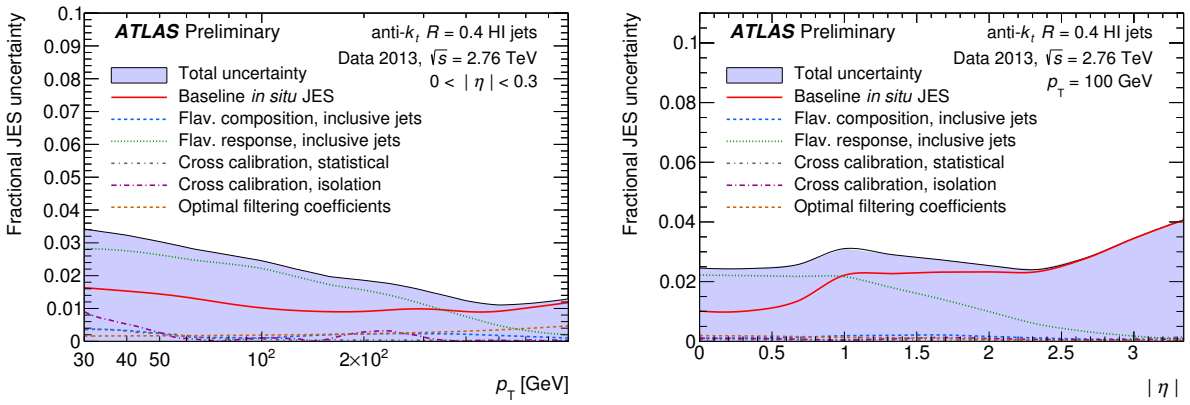

Figure 5.11: The various contributions fractional JES uncertainty as function of p_{T} for $|\eta| < 0.3$ (left) and as a function of $|\eta|$ for ($p_{\mathrm{T}} = 100\,\mathrm{GeV}$) for HI jets in $\sqrt{s} = 2.76\,\mathrm{TeV}$ pp data [68].

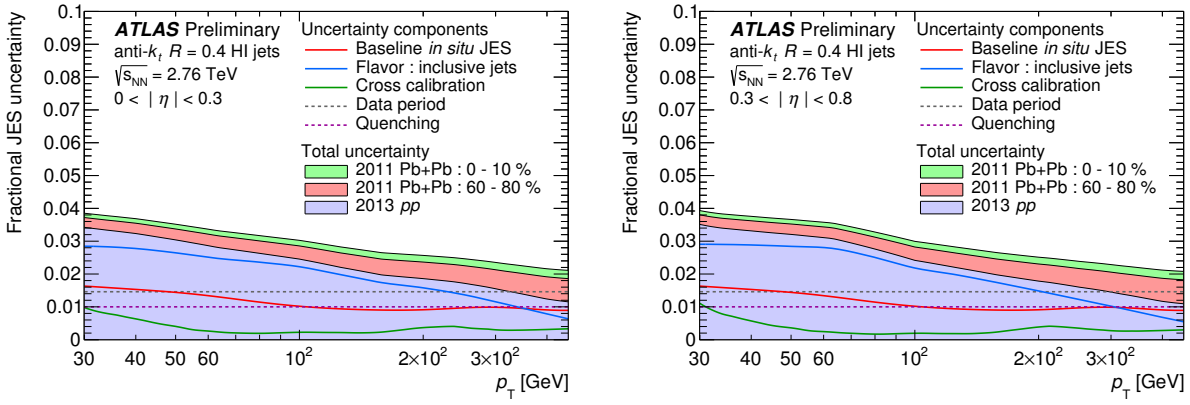

Figure 5.12: The total JES uncertainty on the 2013 $\sqrt{s} = 2.76\,\mathrm{TeV}$ pp data (filled blue), with the total uncertainty in 2011 $\sqrt{s_{\mathrm{NN}}} = 2.76\,\mathrm{TeV}$ Pb+Pb data in the 60–80% (filled blue plus red) and 0–10% (filled blue plus red plus green) show for different ranges of $|\eta|$ [68].

6. Measurement of Jet Fragmentation Functions

6.1 Introduction

Modification of jet fragmentation functions (FF) in HI collisions is one of the predicted effects due to the jet quenching, see section 3.4. ATLAS published first measurement of jet fragmentation functions in 2014 [62] utilizing Pb+Pb data collected in 2011 at centre-of-mass energy $\sqrt{s_{\mathrm{NN}}} = 2.76\,\mathrm{TeV}$. The significant modification of the fragmentation functions was revealed through the comparison between the FF in central and peripheral collisions. The motivation for the analysis presented in this chapter was to extend and improve the first ATLAS measurement. The main improvements compared to the old measurement is the usage of pp data collected in 2013 at the same CMS energy as Pb+Pb as a reference and extending the measurement in the charged tracks phase space down to 1 GeV. To explore the jet modification in more detail presented measurement is also more differential, measuring FF in four bins in jet rapidity and in four bins in $p_{\mathrm{T}}^{\mathrm{jet}}$. Last but not least the reduction of the systematic uncertainties due to the unfolding was achieved with the help of the 2-dimensional Bayesian unfolding.

The same variables used in the first ATLAS measurement [62] are used in this analysis, namely the distributions of charged particle transverse momentum inside the jet $D(p_{\mathrm{T}})$

$$D(p_{\mathrm{T}}) \equiv \frac{1}{N_{\mathrm{jet}}} \frac{\mathrm{d}N_{\mathrm{ch}}(p_{\mathrm{T}})}{\mathrm{d}p_{\mathrm{T}}} \tag{6.1}$$

and jet fragmentation functions $D(z)$

$$D(z) \equiv \frac{1}{N_{\mathrm{jet}}} \frac{\mathrm{d}N_{\mathrm{ch}}}{\mathrm{d}z}. \tag{6.2}$$

where N_{jet} is the total number of jets, N_{ch} is number of charged particles associated with a jet, and the longitudinal momentum fraction z is defined as

$$z \equiv \frac{p_{\mathrm{T}}}{p_{\mathrm{T}}^{\mathrm{jet}}} \cos \Delta R = \frac{p_{\mathrm{T}}}{p_{\mathrm{T}}^{\mathrm{jet}}} \cos \sqrt{\Delta y^2 + \Delta \phi^2}. \tag{6.3}$$

The Δy resp. $\Delta \phi$ are the distance between the jet axis and the charged particle position in rapidity resp. azimuth. The charged particles are required to be within $\Delta R < 0.4$ to jet. Jets were clustered with the anti-k_t algorithm with the radius parameter $R = 0.4$.

6.2 Event selection and MC

6.2.1 Heavy ion data

The Pb+Pb data used in this study were collected during the 2011 Heavy Ion run with the centre-of-mass energy $\sqrt{s_{\mathrm{NN}}} = 2.76\,\mathrm{TeV}$. The full sample of events reconstructed in the Hard Probe stream has been used giving the total collected

luminosity of $158\,\mu\text{b}^{-1}$. It was reduced to $140\,\mu\text{b}^{-1}$ due to the requirement that all the subdetector systems, namely tracking, calorimeter, and muon spectrometers, were fully functional.

The default jet finding algorithm used in high-level-trigger (HLT) for heavy-ion collisions is anti-k_t algorithm with the distance parameter $R = 0.2$. The primary HLT trigger this analysis used required at least one HLT anti-k_t $R = 0.2$ jet with $E_{\text{T}} > 20\,\text{GeV}$ present in the event. The HLT trigger jets are not calibrated to the hadronic scale, i.e. they are at the electromagnetic scale. For $R = 0.4$ offline jets the trigger reaches full efficiency at $p_{\text{T}} \approx 90\,\text{GeV}$, which is sufficiently below the p_{T} cut of 100 GeV used in this study. Beside the HLT trigger requirement the events have to obey the requirement of at least one good primary vertex and good timing measured by the Minimum-Bias Trigger Scintillator.

For this analysis the HI data have been divided into seven centrality classes, 0-10%, 10-20%, 20-30%, 30-40%, 40-50%, 50-60%, and 60-80% (for details on the centrality see section 2.2).

6.2.2 Proton-proton data

The *pp* data used in this analysis were recorded during the 2013 data taking period at the centre-of-mass energy $\sqrt{s} = 2.76\,\text{TeV}$. It consists of six runs comprising a total integrated luminosity of 4.1 pb^{-1}. The pileup during this period was $\mu \sim 0.3 - 0.6$. Events were selected using the HLT jet trigger running the anti-k_t clustering algorithm with $R = 0.4$ with minimum jet p_{T} cut set to $p_{\text{T}} = 75\,\text{GeV}$. For $R = 0.4$ offline jets the trigger is fully efficient at $p_{\text{T}} \approx 80\,\text{GeV}$, which is again sufficient for the p_{T} cut of 100 GeV used in this study. The events were required to contain reconstructed primary vertex and be in the lumi blocks with good quality flag.

6.2.3 Monte Carlo Samples

As a Pb+Pb Monte Carlo (MC) reference, the studies in this note utilize a sample of minimum bias heavy ion data events with embedded MC11 PYTHIA *pp* di-jet events at $\sqrt{s} = 2.76\,\text{TeV}$. PYTHIA simulation uses PYTHIA version 6.423 [65] and the AUET2B tune. The minimum bias heavy ion data were collected for this overlay MC during the 2011 run. The events were triggered by a minimum bias trigger. The signal from this trigger was combined with the signal from PYTHIA at the digitization stage, and then reconstructed as a combined event. The datasets of heavy ion MC are summarized in Tab. 6.1.

The MC sample used for the simulation of *pp* data utilizes the same generator and tune but was simulated with detector conditions corresponding to 2013 data taking.

6.3 Track and jet selections

The charged particles are reconstructed in the inner detector that covers the $|\eta| < 2.5$. Thus the analysis can only be performed for jets within the rapidity interval of $|y| < 2.1$. Jets within the region $0.8 < y < 1.2$ were excluded from the analysis due to the worse performance of the tracking reconstruction nearby

J sample	Dataset	Events
1	mc11_2TeV.105010.J1_pythia_jetjet. recon.NTUP_HI.e1296_d724_r4789	4.54M
2	mc11_2TeV.105011.J2_pythia_jetjet. recon.NTUP_HI.e1296_d724_r4789	4.53M
3	mc11_2TeV.105012.J3_pythia_jetjet. recon.NTUP_HI.e1296_d724_r4789	4.53M
4	mc11_2TeV.105013.J4_pythia_jetjet. recon.NTUP_HI.e1296_d724_r4789	4.52M
5	mc11_2TeV.105014.J5_pythia_jetjet. recon.NTUP_HI.e1296_d724_r4789	4.49M

Table 6.1: MC datasets used. All samples use the PYTHIA to minimum bias data embedding procedure.

this region. In the default configuration of this analysis reconstructed jets are selected to have $p_{\mathrm{T}} > 100\,\mathrm{GeV}$ which ensures a fully efficient HLT and offline jet reconstruction.

Track-quality selection requirements consist of cuts on number of hits in different subdetectors of ID and cuts on the pointing of tracks to the primary vertex. The longitudinal (z_0) and transverse (d_0) impact parameter of the track measured with respect to the primary vertex are scaled by their errors (d_0^{cov}, z_0^{cov}, $\sin\theta^{cov}$, and $\mathrm{cov}(d_0, \theta)$) which defines a significance of the impact parameter (σ_{z_0} and σ_{d_0}).

For the Pb+Pb data and MC, the list of track-quality selection requirements is the following [71]

- at least two hits in the Pixel ID
- at least seven hits in the Semiconductor Tracker (SCT)
- at least one hit in the first layer of the Pixel ID (BLayer) if expected
- $\sigma_{d_0} \equiv \frac{d_0}{\sqrt{d_0^{cov}}} < 3$
- $\sigma_{z_0} \equiv \frac{z_0 \sin\theta}{\sqrt{z_0^{cov}\sin^2\theta + \sin\theta^{cov}(z_0\cos\theta)^2}} < 3$

For pp data and MC, the last two cuts on pointing were relaxed and on top of the requirements on hits, requirements on d_0 and $z_0\sin(\theta)$ were imposed on tracks. To conclude, the track-quality selection requirements in pp are the following

- at least one hits in the Pixel ID
- at least six hits in the Semiconductor Tracker (SCT)
- at least one hit in the first layer of the Pixel ID (BLayer) if expected
- $|d_0|$ impact parameter was parametrized in the region of $p_{\mathrm{T}}^{\mathrm{trk}}$ 1–100 GeV using

$$d_0(p_{\mathrm{T}}^{\mathrm{trk}}) = a_0 e^{a_1 p_{\mathrm{T}}} + a_3 e^{a_4 p_{\mathrm{T}}} \tag{6.4}$$

where a_i represent free parameters of the fit. Recommendation values are $|d_0| < 1.5$ mm for tracks with $p_{\mathrm{T}} < 10$ GeV and $|d_0| < 0.2\,\mathrm{mm}$ for tracks with $p_{\mathrm{T}} > 10\,\mathrm{GeV}$.

This was chosen to guarantee a smooth behaviour of the d_0 parameter as a function of track momentum.

- $|z_0 \sin(\theta)| < 1.5\,\mathrm{mm}$

6.4 Underlying event subtraction

Charged particles from the UE not originating from the jet constitute a background that needs to be subtracted. The size of the background contribution depends on $p_{\mathrm{T}}^{\mathrm{ch}}$, y^{jet}, and the centrality of the collision. In certain regions of the phase space the background contribution to the unsubtracted distributions can be dominant.

The size of the background contribution was evaluated for each measured jet using a grid of $R = 0.4$ cones that spanned the full coverage of the inner detector. The cones had a fixed distance between their centroids chosen such that the coverage of the inner detector was maximized while the cones do not overlap each other. Any cone that was likely associated with the real jet was excluded from the UE background estimation. Specifically cones having a charged particle with $p_{\mathrm{T}}^{\mathrm{ch}} > 6\,\mathrm{GeV}$ or having a distance between its centroid and the nearest jet with $p_{\mathrm{T}} > 90\,\mathrm{GeV}$ smaller then 0.4 were considered as a real jets and were excluded [71].

The resulting UE charged particle yields in given centrality bin were evaluated over $1 < p_{\mathrm{T}}^{\mathrm{ch}} < 6$ GeV as a function of charged particle $p_{\mathrm{T}}^{\mathrm{ch}}$, $p_{\mathrm{T}}^{\mathrm{jet}}$, and y^{jet} and averaged over all cones. The estimation of UE contribution was corrected for the difference in the average UE particle yield at a given $p_{\mathrm{T}}^{\mathrm{ch}}$ between the η position of the cone and η^{jet}. It was corrected also for the difference in the elliptic flow modulation at the ϕ position of the UE cone and ϕ^{jet}. That correction was based on a parametrization of the $p_{\mathrm{T}}^{\mathrm{ch}}$ and centrality dependence of previously measured elliptic flow coefficients, v_2 [7]. The independent check of the UE background estimation was done by measuring the charged track spectra in the MB data which are correct UE background estimation by definition. The UE yields obtained by the cone method are in good agreement with the estimation from MB data.

6.5 Corrections

6.5.1 Tracking efficiency correction

To correct for the inefficiency of the charged particle track reconstruction the tracking efficiency correction has been derived using the MC PYTHIA di-jet events. The simple idea behind this correction is that if there is efficiency of track reconstruction $\varepsilon < 1$ in given point of phase space then every track reconstructed at this point of phase space is given weight $c = 1/\varepsilon$.

The efficiency depends on the track p_{T} y, and centrality. Thus the efficiency as a function of p_{T} was determined separately for four rapidity bins (same as the FF

analysis uses) and seven centralities (and separately for pp collisions). To estimate the reconstruction efficiency, matching of the tracks and truth particles in MC has been performed. To select the tracks in MC analogical to analysis only tracks and truth particles associated to $R = 0.4$ truth jets were used as the input to the efficiency correction. Jets were required to have $p_{\mathrm{T}} > 100\,\mathrm{GeV}$. To guarantee a smooth behaviour of the correction factors as a function of track momentum, the tracking efficiency has been parametrized in the region of $p_{\mathrm{T}}^{\mathrm{trk}} = 1 - 90\,\mathrm{GeV}$ using [71]

$$\varepsilon(p_{\mathrm{T}}^{\mathrm{trk}}) = \sum_{i=0}^{4} a_i \log^i(p_{\mathrm{T}}) \tag{6.5}$$

where constants a_i represent free parameters of the fit. To suppress the fluctuations at high-p_{T} caused by the lower statistics the linear dependency was used at $p_{\mathrm{T}} > 90\,\mathrm{GeV}$. The slope was determined by the difference of the fit in $p_{\mathrm{T}} = 70\,\mathrm{GeV}$ and $p_{\mathrm{T}} = 90\,\mathrm{GeV}$.

Correction for correlation of underlying event and jet energy resolution

The jet produced in region where UE background contribution is larger (smaller) has on average larger (smaller) $\Delta p_{\mathrm{T}}^{\mathrm{jet}} = p_{\mathrm{T}}^{\mathrm{rec}} - p_{\mathrm{T}}^{\mathrm{truth}}$. If cut on reconstructed $p_{\mathrm{T}}^{\mathrm{jet}}$ is applied then the average UE contribution to jets is larger then UE estimated by the cone method because jets with larger UE contribution are (unwelcomely) selected. The size of this effect depends on the η and centrality and has also minor $p_{\mathrm{T}}^{\mathrm{jet}}$ and $p_{\mathrm{T}}^{\mathrm{ch}}$ (z) dependence.

To correct for this effect, the centrality-, y-, $p_{\mathrm{T}}^{\mathrm{jet}}$- and $p_{\mathrm{T}}^{\mathrm{ch}}$-dependent (or z-dependent) multiplicative correction factors were applied to UE distributions. These multiplicative factors were estimated as a ratio of UE distributions calculated from tracks within the area of a jet which do not have an associated truth particle and the original UE distributions. The example of those factors is plotted as a function of $p_{\mathrm{T}}^{\mathrm{jet}}$ and $p_{\mathrm{T}}^{\mathrm{trk}}$ for 0-10% bin and for jets with $|y| < 2.1$ in Figure 6.1. These factors are applied to estimated UE contribution prior to the subtraction.

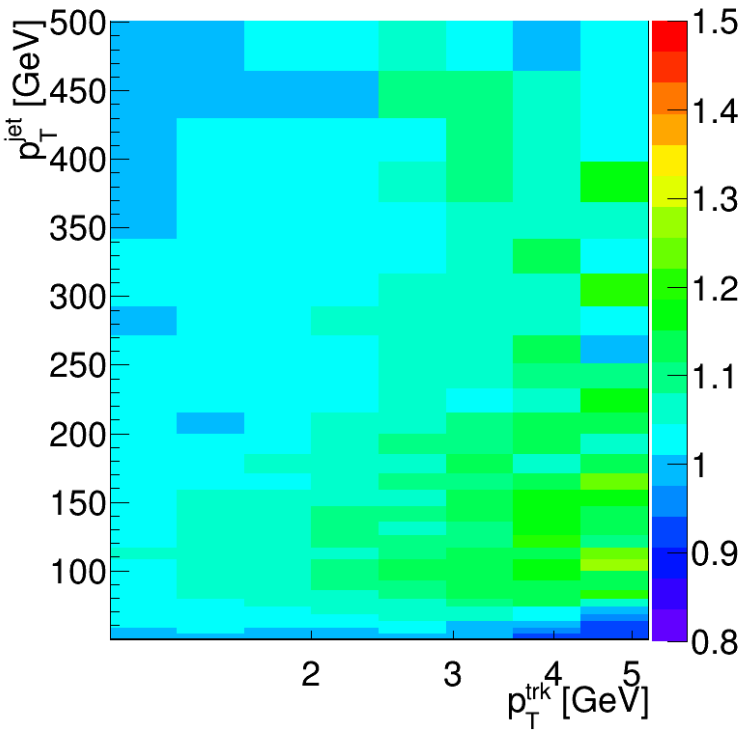

Figure 6.1: The multiplicative correction factors that correct for the correlation between the UE and the JER (for more details see the text).

6.6 Unfolding

To extract the physical distributions smeared by the finite resolution of the detector the unfolding procedure was used[1]. The necessity to unfold in both track p_{T} or z and jet p_{T} in parallel lead to the selection of the 2-dimensional Bayesian unfolding which is implemented in the RooUnfold package [72]. The implementation of the algorithm which we shortly summarize below, is based on the papers [73, 74]. Since the FF distributions are normalized by the number of jets it was necessary to unfold jet spectra as well. To correct for the jet resolution 1D Bayesian unfolding was applied to jet spectra independently of the unfolding of the FF.

The goal for the unfolding procedure is to obtain the physical (or "true") spectra that caused the observation. In other words we want to obtain numbers $\hat{n}(C_i)$ of causes that caused the spectrum we observed $n(E_j)$ (numbers of effects). From Monte Carlo simulation we can obtain the probabilities $\lambda_{ji} \equiv P(E_j|C_i)$ - this is usually called the response matrix. To get the probabilities $P(C_i|E_j)$ that we need the Bayes formula is used

$$P(C_i|E_j) = \frac{P(E_j|C_i)P_0(C_i)}{\sum_{l=1}^{n_C} P(E_j|C_l)P_0(C_l)} \tag{6.6}$$

where $P_0(C_i)$ is the so called prior which expresses the initial probabilities of the causes based on the a priori knowledge. In the case of complete ignorance the

[1] This procedure is outside the HEP community usually called deconvolution

$P_0(C_i)$ will be the uniformly distributed $P_0(C_i) = 1/n_i$. The algorithm implemented in RooUnfold however uses the truth projection of the response matrix as a prior. Once the probabilities $P(C_i|E_j)$ are calculated the true spectrum can be calculated

$$\hat{n}(C_i) = \sum_{j=1}^{n_E} n(E_j)P(C_i|E_j) \tag{6.7}$$

as well as the final probabilities of the causes

$$\hat{P}(C_i) \equiv P(C_i|\mathbf{n}(E)) = \frac{\hat{n}(C_i)}{\hat{N}_{\text{true}}}. \tag{6.8}$$

If the initial distribution does not agree with the real distribution (it rarely does), it will not agree with the calculated distribution $\hat{P}(C_i)$. Then it is possible to proceed iteratively - replace in the equation (6.6) $P_0(C_i)$ by $\hat{P}(C_i)$, calculate new $\hat{n}(C_i)$ and $\hat{P}(C_i)$ and proceed until the agreement is good (the distribution does not change after the iteration). This algorithm can be easily extended to more dimensions. The calculation of the uncertainties is possible but it is not trivial and its description is beyond the scope of this work so we will not describe it here.

The response matrix (RM) for the 2D unfolding is the 4D object. Each entry in the response matrix is the tuple of the $p_{\text{T}}^{\text{jet,truth}}$, $p_{\text{T}}^{\text{jet,reco}}$, $p_{\text{T}}^{\text{truth}}$ (z_{truth}), $p_{\text{T}}^{\text{reco}}$ (z_{reco}) where truth and reconstructed objects were matched. The response matrices were "filled" separately for each centrality, rapidity (or jet p_{T}) bin and distribution.

The important thing in the unfolding procedure is the binning of the response matrix and corresponding raw (= before unfolding) and unfolded distributions. Binning of this analysis was selected to ensure that:

1. The kinematic range of unfolded distribution is a subset of kinematic range of truth axis of the response matrix.

2. There is more bins along the reconstructed axis then along the truth axis.

3. The range of the bins along the reconstructed axis is larger than the range of bins along the truth axis.

Moreover the binning of the truth jet axis was selected to match with the binning of the jet R_{AA} measurement. The three examples of the response matrices are in Figure 6.2. These are in fact projections of the 4D response matrices. Response matrices are approximately diagonal which eases the unfolding procedure.

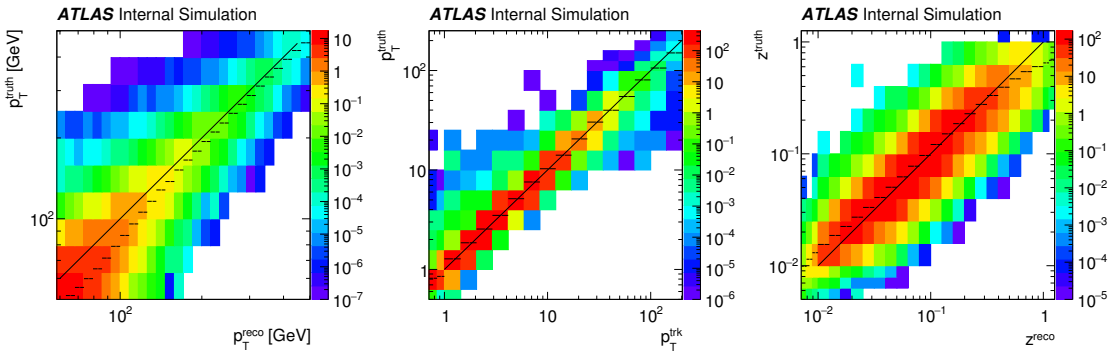

Figure 6.2: Three examples of the response matrices: response matrix for jet p_{T} (left), track p_{T} (middle) and z (right). These are in fact projections from the 4D response matrix.

To test the performance of the unfolding and the whole analysis chain the closure tests were performed - the unfolded distributions were compared with the truth distributions in the MC simulations. This was done in both the pp and Pb+Pb simulations with satisfying results - no systematic disagreement between unfolded and true distributions was found. Two examples of closure tests for $D(p_{\mathrm{T}})$ distributions are in Figure 6.3. The closure test for the jet spectra was also done - see Figure 6.4. The good agreement was found.

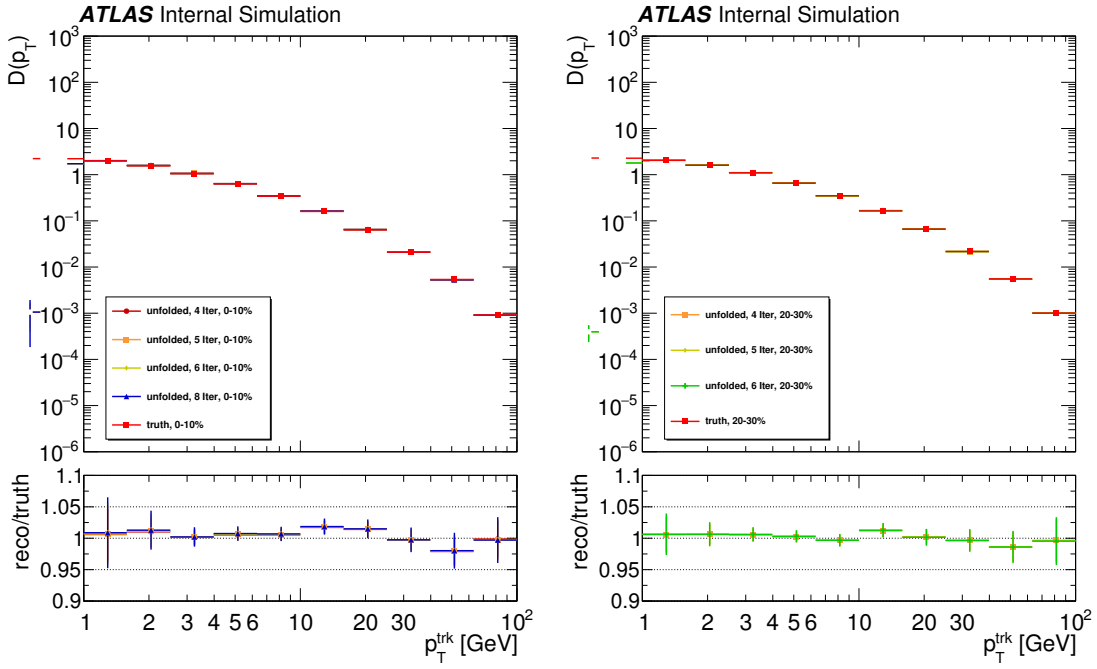

Figure 6.3: Two examples of the closure test for $D(p_{\mathrm{T}})$ distributions performed in MC. Left: central collisions. Right: semicentral (20-30%) collisions.

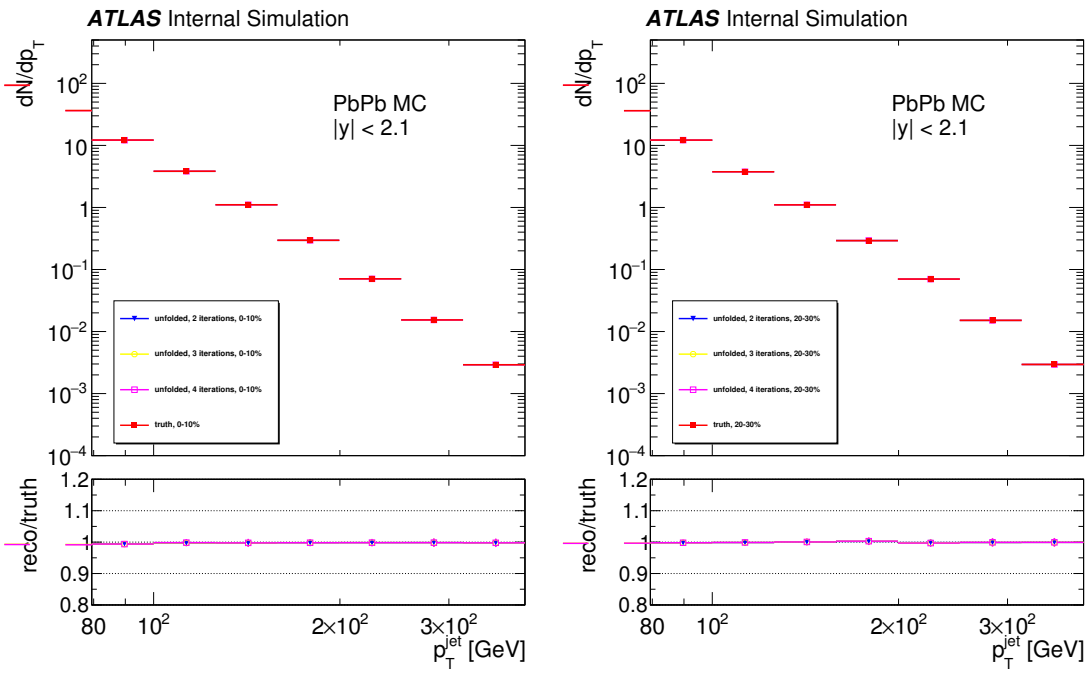

Figure 6.4: Two examples of the closure test for jet spectra performed in MC. Left: central collisions. Right: semicentral (20-30%) collisions.

The stability of the unfolding with the number of iterations was carefully studied in data. In Figure 6.5 the two examples of the plots we made are depicted. The unfolding was found to be stable after 5 iterations so it was chosen as a default choice except in the central Pb+Pb collisions where 8 iterations was chosen to be the optimum choice. This is probably caused by the larger jet energy resolution in central Pb+Pb collisions.

The so called refolding was done in the data to check the consistency of the unfolding. In this test one first unfolds the distributions with given response matrix and then multiplies unfolded distributions with this matrix back into the raw distribution. If the resulting distribution wouldn't agree with original raw distribution that would mean there is some inconsistency in the procedure. Results of our refolding tests didn't show up any signs of problems as can reader check in Figure 6.6 where two example plots are depicted.

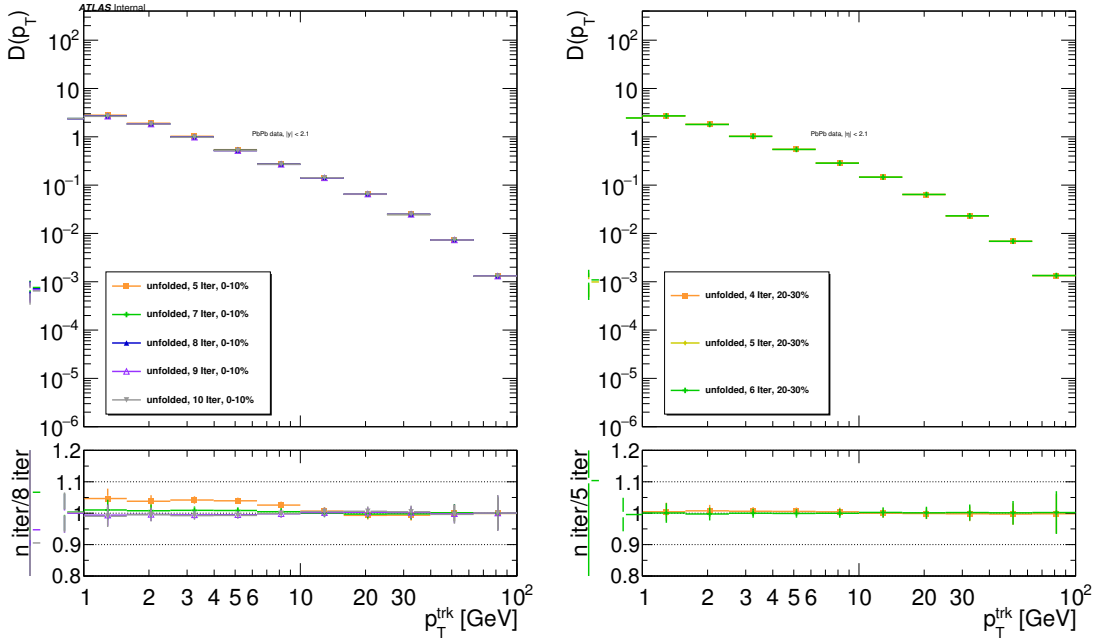

Figure 6.5: Two examples of the stability test for $D(p_{\mathrm{T}})$ distributions performed in Pb+Pb data. Left: central collisions. Right: semicentral (20-30%) collisions.

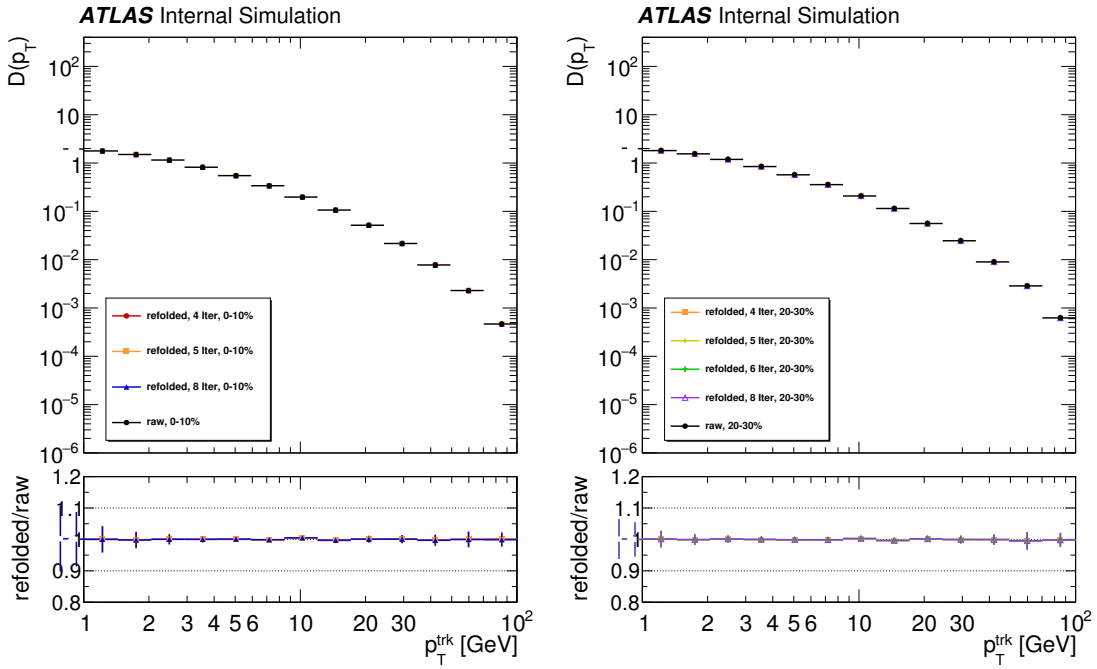

Figure 6.6: Two examples of the refolding test for $D(p_{\mathrm{T}})$ distributions performed in Pb+Pb data. Left: central collisions. Right: semicentral (20-30%) collisions.

6.7 Systematic uncertainties

In this section, the systematic uncertainties of the FF measurement are discussed. The systematic uncertainties were evaluated for distributions independently for each centrality and for each rapidity or jet p_{T} bin. To evaluate the systematic uncertainties for ratios the new ratios were calculated from the shifted distributions. These ratios were then used for the estimation of the uncertainty. There are following sources of systematic uncertainties identified for this measurement:

- Jet energy scale
- Jet energy resolution
- Reconstruction of tracks
- Unfolding

The positive relative uncertainty has been used to calculate the upper bound of the systematic uncertainty on the measured distribution, whereas the negative relative uncertainty has been used to calculate the lower bound. The systematic uncertainties were combined together assuming they are independent.

6.7.1 Jet energy scale

The systematic uncertainty due to the jet energy scale (JES) and its derivation is described in section 5.4. The impact of the absolute JES uncertainty on the measured distributions was determined by shifting the transverse momentum of reconstructed jets as follows

$$p_{\mathrm{T}}{}' = p_{\mathrm{T}} \cdot (1 \pm U^{\mathrm{JES}}(p_{\mathrm{T}}, y)) \tag{6.9}$$

where $U^{\mathrm{JES}}(p_{\mathrm{T}}, y)$ is the fractional JES uncertainty. The distributions with shifted p_{T} were unfolded and compared to original distributions. The difference has been used as an estimate of the systematic uncertainty.

6.7.2 Jet energy resolution

The difference between jet energy resolution in data and MC can cause that MC does not describe reality correctly which influences the response matrix and consequently unfolding procedure. To estimate the effect it can have at the fragmentation functions new response matrices were generated with modifications to the $\Delta p_{\mathrm{T}} = p_{\mathrm{T}}^{\mathrm{truth}} - p_{\mathrm{T}}^{\mathrm{rec}}$ for each matched truth-reconstructed jet pair.

The procedure to generate modified response matrices follows the standard procedure applied in pp jet measurements. The matrix was generated by repeating the MC study with modifications to the $\Delta p_{\mathrm{T}} = p_{\mathrm{T}}^{\mathrm{truth}} - p_{\mathrm{T}}^{\mathrm{rec}}$ for each matched truth-reconstructed jet pair. The jet ${p_{\mathrm{T}}}^{\mathrm{reco}}$ was then smeared by

$${p_{\mathrm{T}}}^{\star,\mathrm{reco}} = {p_{\mathrm{T}}}^{\mathrm{reco}} \times \mathcal{N}(1, \sigma_{\mathrm{JER}}^{\mathrm{eff}}) \,, \tag{6.10}$$

where $\mathcal{N}(1, \sigma_{\mathrm{JER}}^{\mathrm{eff}})$ is the normal distribution with the effective resolution $\sigma_{\mathrm{JER}}^{\mathrm{eff}} = \sqrt{(\sigma_{\mathrm{JER}} + \sigma_{\mathrm{JER}}^{\mathrm{syst}})^2 - \sigma_{\mathrm{JER}}^2}$. As this smearing is random the procedure is repeated 10 times.

6.7.3 Reconstruction of tracks

The estimation of the systematic uncertainty due to track reconstruction was based on the systematic uncertainty in the determination of the tracking efficiency correction. This systematic uncertainty was estimated by performing the analysis with three different sets of selection criteria imposed on tracks: "loose", "standard", and "tight". Standard selection criteria were the default criteria used in the analysis. The estimation of the systematic uncertainty due to tracking was done by repeating the analysis with the "loose" and "tight" selection criteria including the derivation of the new efficiencies, response matrices and the rest of the analysis. The differences in the results between the default and modified analysis was taken as the systematic uncertainty due to reconstruction of tracks.

6.7.4 Systematic uncertainty due to unfolding

The systematic uncertainty associated with the unfolding is connected with the sensitivity of the unfolding procedure to the choice of the number of iterations and to the difference in the prior between the data and MC. As shown in section 6.6 five iterations were found to be the best choice for all distributions except those evaluated in the 0-10% centrality bin where eight iterations was chosen. The sensitivity of the unfolding on the choice of the number of iterations is evaluated by changing the number of iterations by ± 1.

To estimate the effect that the difference in the shape of the truth distributions in MC and physics distributions in data can have, the unfolding was repeated with the reweighed response matrix. It was reweighed by a factors that change the truth distribution so that it coincide with the measured distribution in 0-10% centrality bin, i.e. the most different distribution. This doesn't change the relation between the truth and reconstructed quantities but it changes the truth projection of the response matrix which is used as a prior in the RooUnfold implementation of the Bayesian unfolding, see section 6.6. Reweighing factors varied from 0.85 to 1.6. The difference between the distribution unfolded with regular matrix and unfolded with the reweighed matrix was taken as the another component of the systematic uncertainty due to the unfolding.

6.7.5 Systematic uncertainties summary

The JES systematic uncertainty was the dominant uncertainty in the most of the covered phase space. The uncertainty due to the JER was usually negligible except the largest p_{T} (z) where it was important component of the total uncertainty. The uncertainty due to the tracking was not negligible in most of the phase space but it was rarely dominant part of the total uncertainty. The remaining components of the uncertainty were usually negligible. The examples of the p_{T} (z) dependence of the total systematic uncertainty and it's components are in Figures 6.7-6.9.

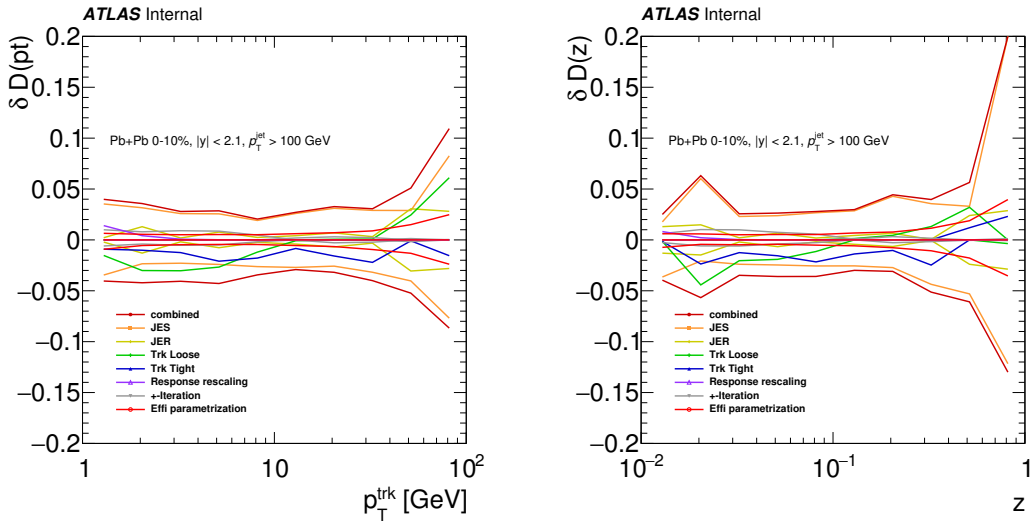

Figure 6.7: The systematic uncertainty and it's components for $D(p_{\mathrm{T}})$ (left) and $D(z)$ (right) distributions in Pb+Pb central collisions.

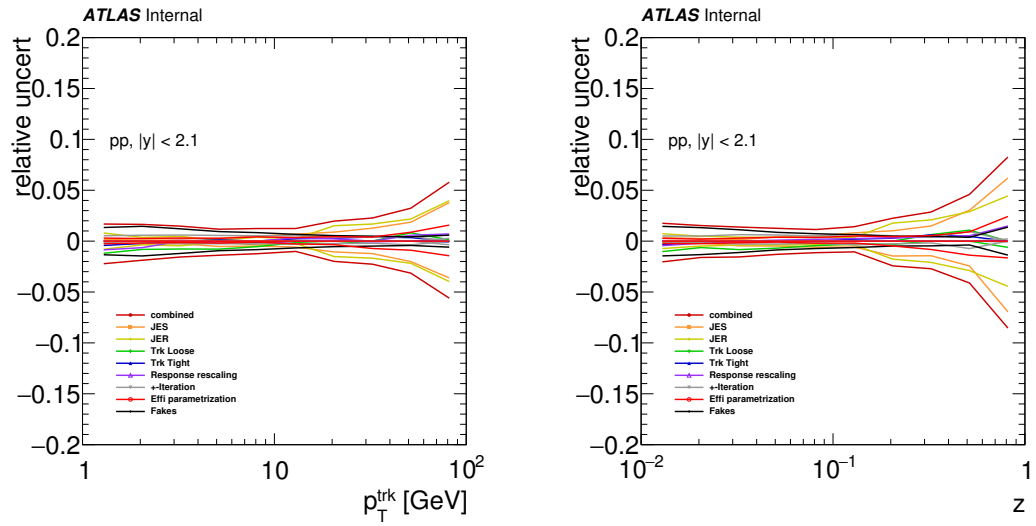

Figure 6.8: The systematic uncertainty and it's components for $D(p_{\mathrm{T}})$ (left) and $D(z)$ (right) distributions in pp collisions.

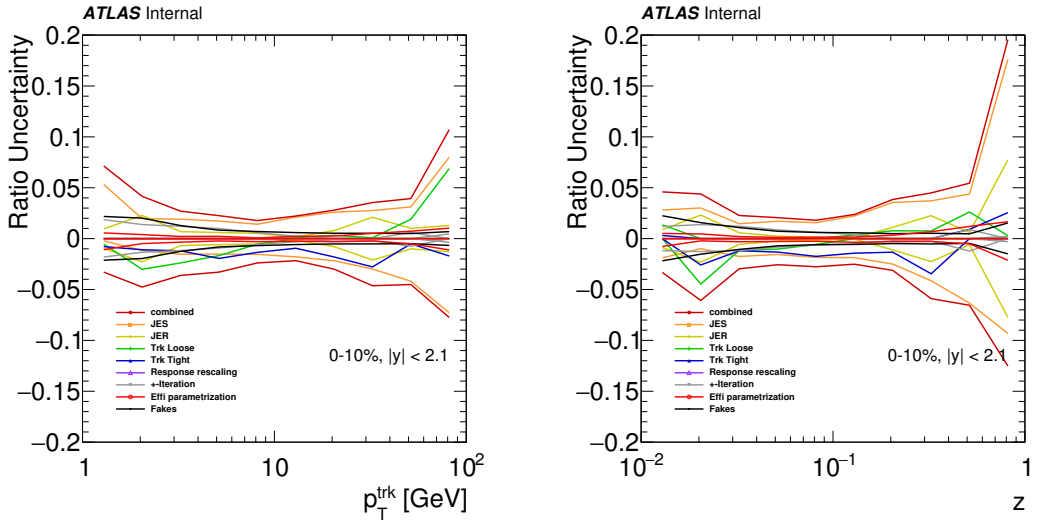

Figure 6.9: The systematic uncertainty and it's components for ratios $R_{D(p_{\mathrm{T}})}$ (left) and $R_{D(z)}$ (right) in the central Pb+Pb collisions.

6.8 Results

Fully unfolded $D(p_{\mathrm{T}})$ and $D(z)$ distributions measured in pp and Pb+Pb collisions (in seven centrality classes) for jets $100 < p_{\mathrm{T}}^{\mathrm{jet}} < 398\,\mathrm{GeV}$ are in Figures 6.10 and 6.11. Each panel is showing different jet rapidity selection. The error bars indicate statistical uncertainties while the shaded bands indicate the systematic uncertainties.

To reveal the size of the modification in Pb+Pb collisions and its centrality and jet rapidity (or jet p_{T} dependence) the ratios $R_{D(p_{\mathrm{T}})}$ and $R_{D(z)}$ of the FF measured in Pb+Pb collisions to those measured in pp collisions were calculated

$$R_{D(p_{\mathrm{T}})} = \frac{D(p_{\mathrm{T}})|_{\mathrm{cent}}}{D(p_{\mathrm{T}})|_{pp}}, \; R_{D(z)} = \frac{D(z)|_{\mathrm{cent}}}{D(z)|_{pp}}. \tag{6.11}$$

In Figures 6.12 and 6.13 the ratios of the $D(p_{\mathrm{T}})$ and $D(z)$ distributions for four different centrality classes (0-10%, 20-30%, 30-40% and 60-80%) and four jet rapidity selections ($|y| < 2.1$, $|y| < 0.3$, $0.3 < |y| < 0.8$ and $1.2 < |y| < 2.1$) are depicted - rows represent different centrality bins, columns represent different rapidity selections. p_{T} of jets was $100 < p_{\mathrm{T}}^{\mathrm{jet}} < 398\,\mathrm{GeV}$. The error bars indicate statistical uncertainties while the shaded bands indicate systematic uncertainties. The ratios have the same pattern as the previous ATLAS measurement [62], i.e. there is an enhancement in the production of the low p_{T} ($p_{\mathrm{T}} \lesssim 4\,\mathrm{GeV}$) particles in jets, suppression of the intermediate p_{T} particles ($4 \lesssim p_{\mathrm{T}} \lesssim 25\,\mathrm{GeV}$) and the small enhancement of the high-p_{T} particles ($p_{\mathrm{T}} \gtrsim 25\,\mathrm{GeV}$). The size of modification decreases for more peripheral collisions. No dependence on the jet rapidity is observed except the highest track p_{T} where a small hint of the y dependence is observed - the enhancement of the high-p_{T} particles in forward jets seems to be smaller than in jets produced in midrapidity region. The same conclusions hold for $R_{D(z)}$ ratios.

In Figures 6.14 and 6.15 the ratios of the $D(p_{\mathrm{T}})$ and $D(z)$ distributions for four different centrality classes (0-10%, 20-30%, 30-40% and 60-80%) and four jet

p_{T} selections ($100 < p_{\mathrm{T}} < 398\,\mathrm{GeV}$, $100 < p_{\mathrm{T}} < 126\,\mathrm{GeV}$, $126 < p_{\mathrm{T}} < 158\,\mathrm{GeV}$ and $158 < p_{\mathrm{T}} < 398\,\mathrm{GeV}$) are depicted - rows represent different centrality bins, columns represent different jet p_{T} selections. Rapidity of jets was $|y| < 2.1$. The same modification pattern as in Figures 6.12 and 6.13 is observed. No significant dependence on the jet p_{T} is observed.

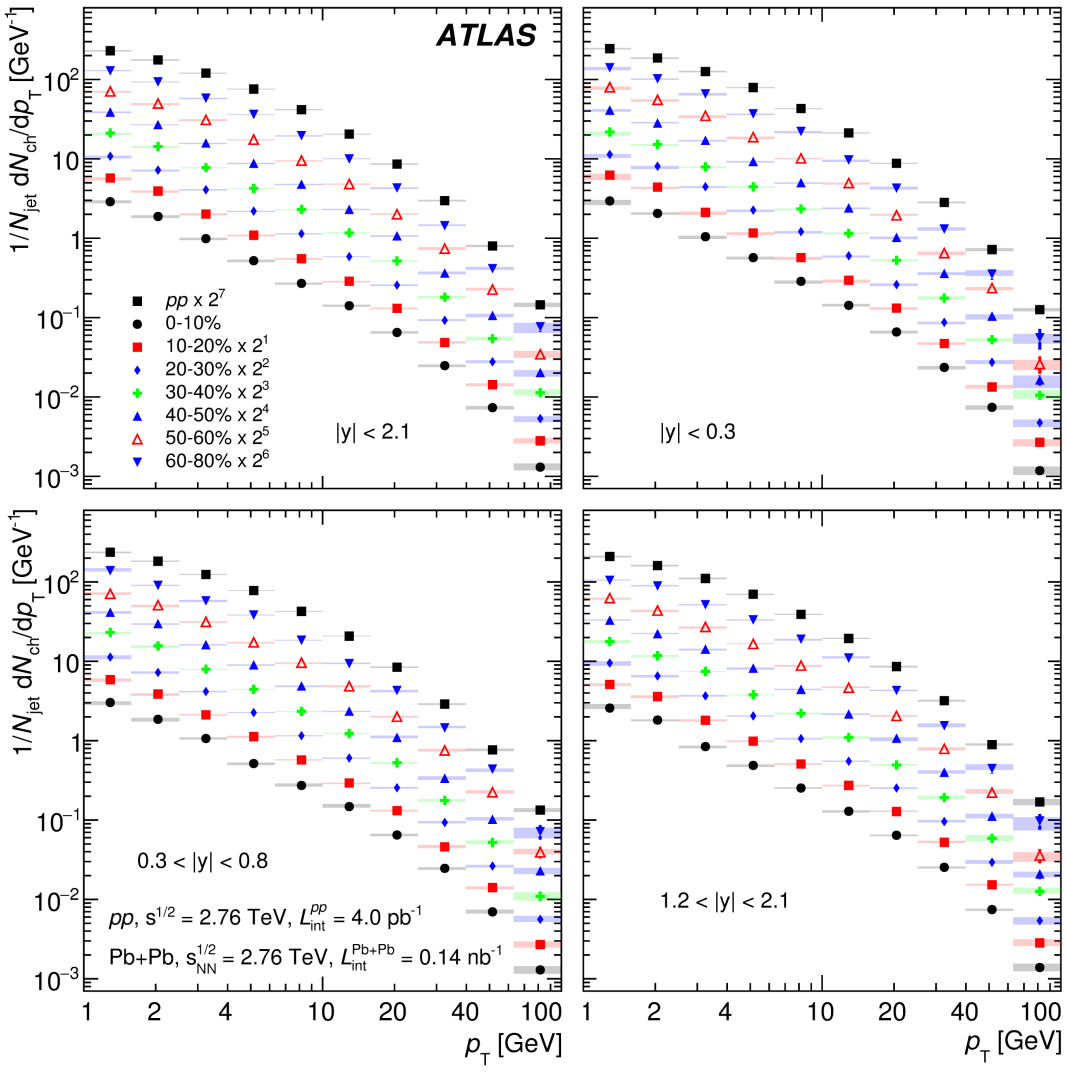

Figure 6.10: Unfolded charged-particle transverse momentum distributions, $D(p_{\mathrm{T}})$, measured in pp collisions and for seven centrality bins measured in Pb+Pb collisions. The four panels show $D(p_{\mathrm{T}})$ distributions with different selections in jet rapidity for jets with p_{T} in the interval of 100–398 GeV. The error bars on the data points indicate statistical uncertainties while the shaded bands indicate systematic uncertainties.

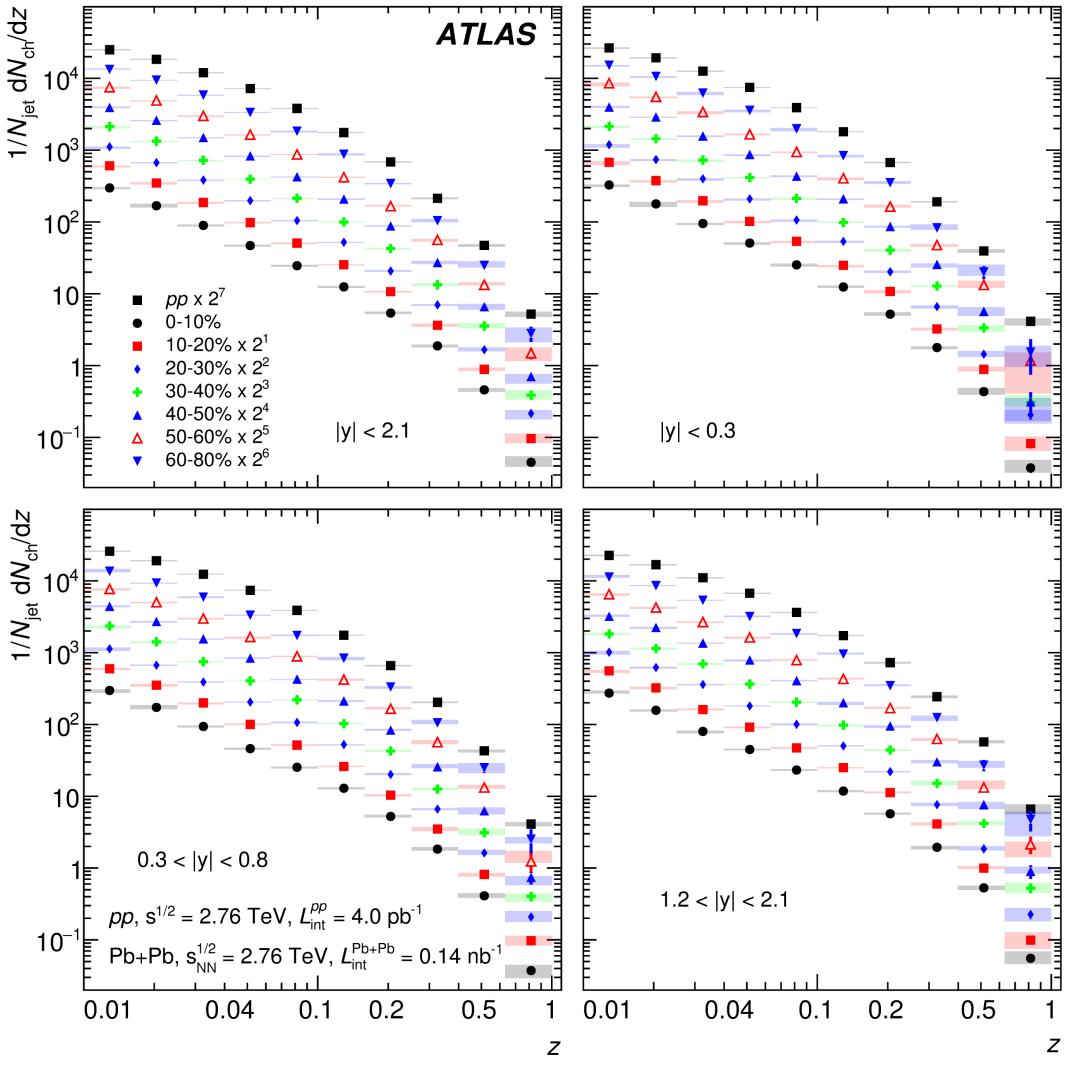

Figure 6.11: Unfolded charged-particle transverse momentum distributions, $D(z)$, measured in pp collisions and for seven centrality bins measured in Pb+Pb collisions. The four panels show $D(z)$ distributions with different selections in jet rapidity for jets with p_{T}in the interval of 100–398 GeV. The error bars on the data points indicate statistical uncertainties while the shaded bands indicate systematic uncertainties.

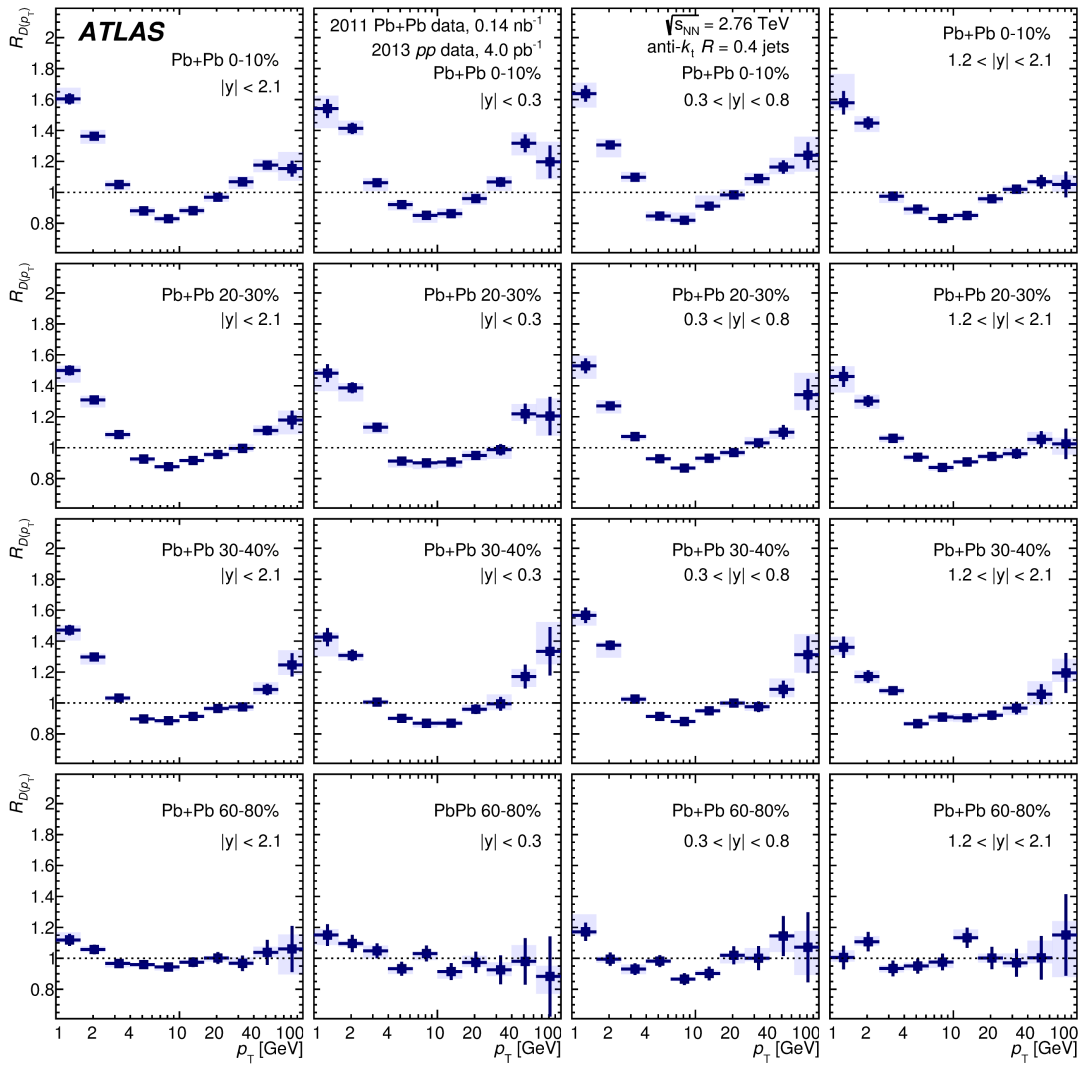

Figure 6.12: The ratio $R_{D(p_{\mathrm{T}})}$ of unfolded $D(p_{\mathrm{T}})$ distributions measured in heavy-ion collisions to unfolded $D(p_{\mathrm{T}})$ distributions measured in pp collisions. The $R_{D(p_{\mathrm{T}})}$ distributions were evaluated in four different centrality bins (rows) and four different selections in jet rapidity of jets (columns) with $100 < p_{\mathrm{T}} < 398$ GeV. The error bars on the data points indicate statistical uncertainties while the shaded bands indicate systematic uncertainties.

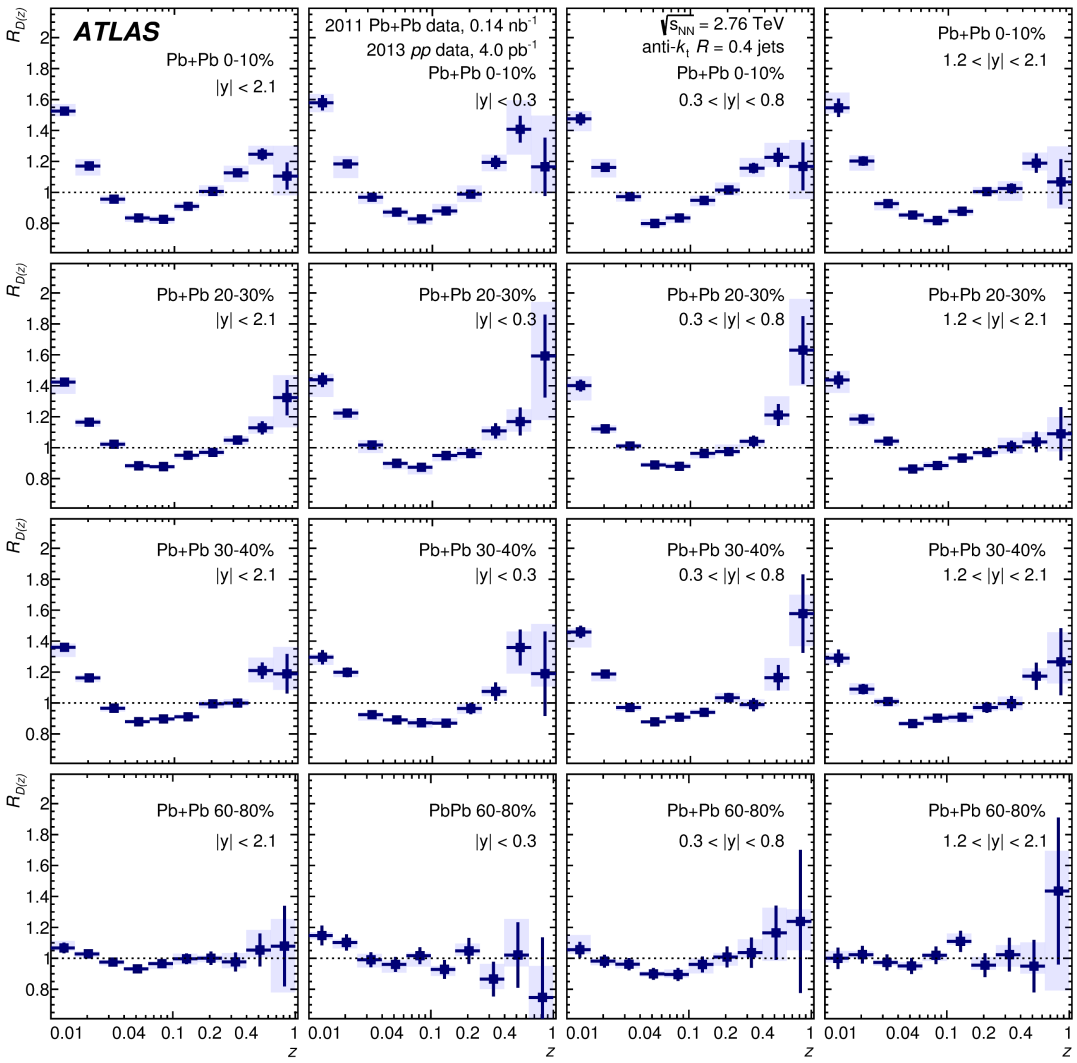

Figure 6.13: The ratio $R_{D(z)}$ of unfolded $D(z)$ distributions measured in heavy-ion collisions to unfolded $D(z)$ distributions measured in pp collisions. The $R_{D(z)}$ distributions were evaluated in four different centrality bins (rows) and four different selections in jet rapidity of jets (columns) with $100 < p_{\mathrm{T}} < 398\,\mathrm{GeV}$. The error bars on the data points indicate statistical uncertainties while the shaded bands indicate systematic uncertainties.

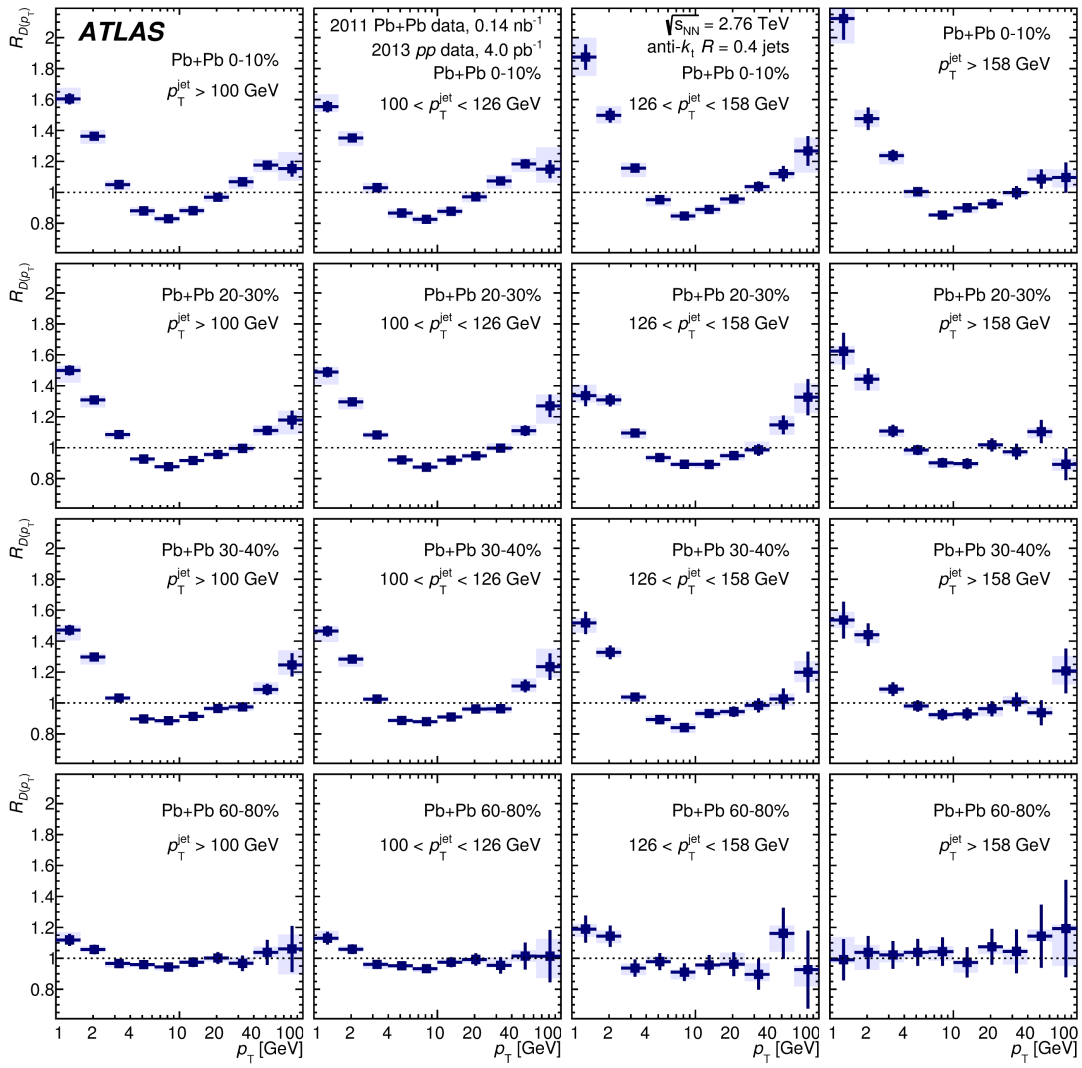

Figure 6.14: The ratio $R_{D(p_{\mathrm{T}})}$ of unfolded $D(p_{\mathrm{T}})$ distributions measured in heavy-ion collisions to unfolded $D(p_{\mathrm{T}})$ distributions measured in pp collisions. The $R_{D(p_{\mathrm{T}})}$ distributions were evaluated in four different centrality bins (rows) and four different selections in p_{T} of jets (columns) with $|y| < 2.1$. The error bars on the data points indicate statistical uncertainties while the shaded bands indicate systematic uncertainties.

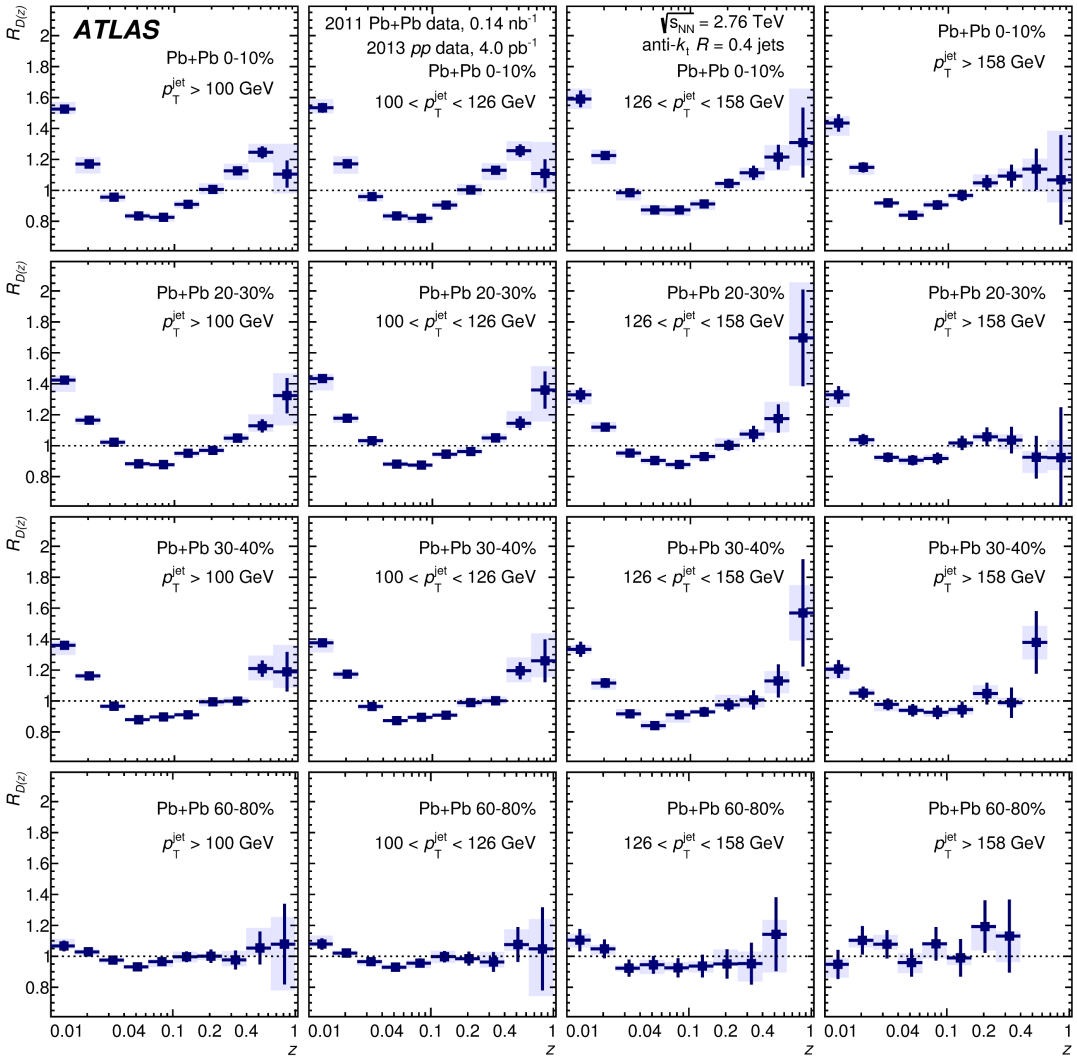

Figure 6.15: The ratio $R_{D(z)}$ of unfolded $D(z)$ distributions measured in heavy-ion collisions to unfolded $D(z)$ distributions measured in pp collisions. The $R_{D(z)}$ distributions were evaluated in four different centrality bins (rows) and four different selections in p_{T} of jets (columns) with $|y| < 2.1$. The error bars on the data points indicate statistical uncertainties while the shaded bands indicate systematic uncertainties.

To quantify the differences in jet fragmentation the difference between integrals of measured $D(p_{\mathrm{T}})$ in Pb+Pb and pp collisions was evaluated in each centrality bin according to:

$$N^{\mathrm{ch}}|_{\mathrm{cent}} \equiv \int_{p_{\mathrm{T,min}}}^{p_{\mathrm{T,max}}} \left(D(p_{\mathrm{T}})|_{\mathrm{cent}} - D(p_{\mathrm{T}})|_{pp} \right) \mathrm{d}p_{\mathrm{T}} \tag{6.12}$$

where ranges ($p_{\mathrm{T,min}}$,$p_{\mathrm{T,max}}$) were chosen to follow borders of the enhancement/suppression regions seen in $R_{D(p_{\mathrm{T}})}$ ratios. Namely enhanced low p_{T} region $1 < p_{\mathrm{T}} < 4\,\mathrm{GeV}$, suppressed intermediate p_{T} region $4 < p_{\mathrm{T}} < 25\,\mathrm{GeV}$ and enhanced high p_{T} region $25 < p_{\mathrm{T}} < 100\,\mathrm{GeV}$. The results of calculations are shown in upper panels of Figure 6.16 where N_{part} dependence of N^{ch} is shown for the most inclusive jet p_{T} and rapidity bins used in the analysis. In all three regions the gradual evolution with centrality is clearly visible and the trends seen in ratios $R_{D(p_{\mathrm{T}})}$ are confirmed and quantified.

To quantify the amount of transverse momentum carried by the extra or missing tracks in Pb+Pb collisions in the characteristic regions, difference of the p_{T} weighed $D(p_{\mathrm{T}})$ integrals were calculated

$$P_{\mathrm{T}}^{\mathrm{ch}}|_{\mathrm{cent}} \equiv \int_{p_{\mathrm{T,min}}}^{p_{\mathrm{T,max}}} \left(D(p_{\mathrm{T}})|_{\mathrm{cent}} - D(p_{\mathrm{T}})|_{pp} \right) p_{\mathrm{T}}\ \mathrm{d}p_{\mathrm{T}} \tag{6.13}$$

in the same intervals as N^{ch}. The N_{part} dependence of the $P_{\mathrm{T}}^{\mathrm{ch}}$ is shown in bottom panels of Figure 6.16. The same conclusions as for integrals N^{ch} holds. To check the consistency the $P_{\mathrm{T}}^{\mathrm{ch}}$ integrals were calculated over the full range of the charged-particle transverse momenta (1-100 GeV). The result were consistent with zero within the uncertainties for all centrality bins.

To investigate the rapidity dependence of the $R_{D(z)}$ ratios, the double ratios of $R_{D(z)}$ were calculated. In Figure 6.17 the ratios of $R_{D(z)}$ in given rapidity interval to $R_{D(z)}$ in $|y| < 2.1$ rapidity interval are shown for three centrality classes. The double ratios suggest the change of the trend at high z between midrapidity and forward region however the size of the statistical and systematical uncertainties does not allow to draw definite conclusions.

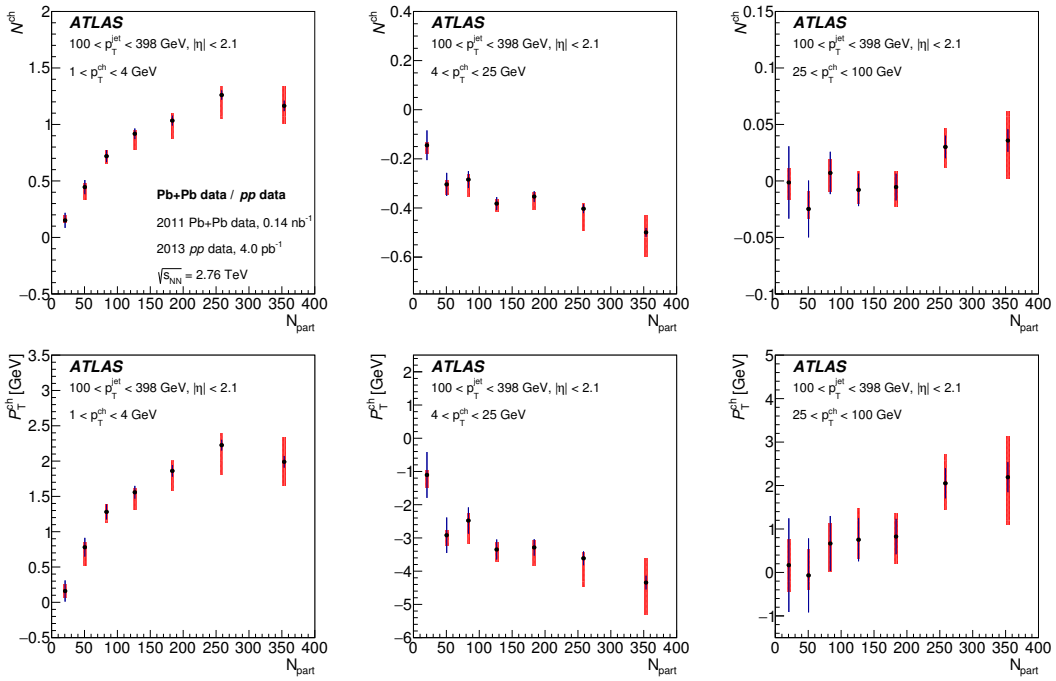

Figure 6.16: (Upper panels) The difference N_{ch} between the total yield of particles in a given $p_{\mathrm{T}}^{\mathrm{ch}}$ interval (indicated in the legend) measured in Pb+Pb collisions and the total yield of particles in the same $p_{\mathrm{T}}^{\mathrm{ch}}$ interval measured in pp collisions. (Lower panels) The difference $P_{\mathrm{T}}^{\mathrm{ch}}$ between the total transverse momentum of particles in a given $p_{\mathrm{T}}^{\mathrm{ch}}$ interval measured in Pb+Pb collisions and the total transverse momentum of particles measured in pp collisions. The differences were evaluated as a function of number of participating nucleons, N_{part}. The error bars on the data points indicate statistical uncertainties while the shaded bands indicate systematic uncertainties.

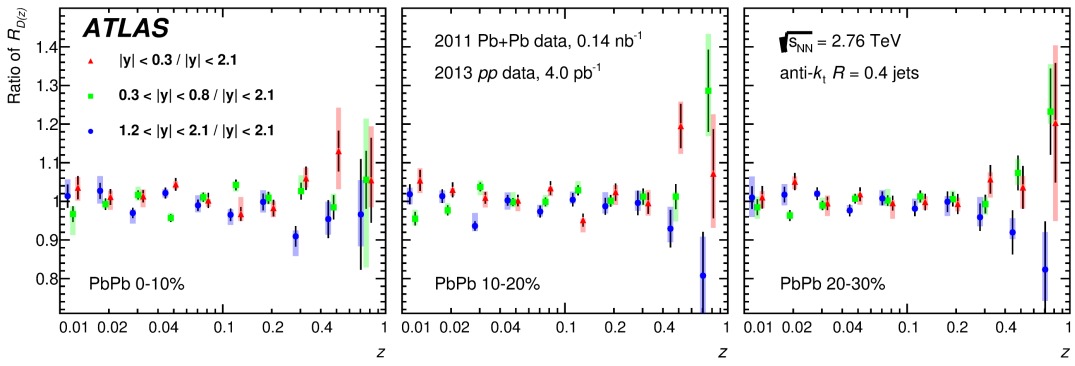

Figure 6.17: The ratio of $R_{D(z)}$ distributions in a given rapidity interval, namely $|y| < 0.3$, $0.3 < |y| < 0.8$, and $1.2 < |y| < 2.1$, to $R_{D(z)}$ in $|y| < 2.1$. The ratio of $R_{D(z)}$ was evaluated for three different collision centralities. The error bars on the data points indicate statistical uncertainties while the shaded bands indicate systematic uncertainties.

7. Summary

In this thesis a short introduction into the field of heavy-ion collisions and motivation for exploration of these collisions were presented. Some general aspects of the heavy-ion collisions were described, the fundamentals of the theory of the strong interaction, quantum chromodynamics, which governs the processes in the HI collisions, was briefly reviewed. The current knowledge of the phase diagram of QCD was presented and the challenges that remain to be addressed were shortly mentioned. These phenomena are the motivation for the physics community to be interested in the QGP and consequently in heavy-ion collisions.

The selected experimental results from RHIC and LHC colliders were presented and discussed - emphasis was put on the results that suggest the creation of the deconfined and strongly interacting matter, QGP. Some measurements that control the production rates of high-p_{T} or high-mass particles were also presented. The jet quenching phenomenon was introduced and briefly explained and experimental results aimed to improve the understanding of this phenomenon were presented with emphasis put on those from LHC and ATLAS experiment.

The Large Hadron Collider in CERN was shortly described. The ATLAS experiment and it's main subdetectors were described in a bit more detail, mainly the parts that are used to study HI collisions.

The jet reconstruction in the HI collisions is challenging by itself due to the large underlying background and fluctuations unavoidably present in the Pb+Pb collisions. The reconstruction chain used by the ATLAS HI jet group to reconstruct and calibrate these jets was described step by step. The subtraction procedure is based on the event-by-event basis. It takes into account azimuthal modulation due to the eliptic flow and subtracts the underlying event energy on the cell level. To better estimate the energy density in given part of the detector the iterative procedure is used to exclude real jets from estimation. The numerical inversion that calibrates jets from electromagnetic scale to the final hadronic scale was derived for four combinations of collision system and centre-of-mass energy. This calibration was used for jet measurements in *pp* and Pb+Pb collisions at $\sqrt{s_{\mathrm{NN}}} = 2.76\,\mathrm{TeV}$ and in p+Pb collisions at $\sqrt{s_{\mathrm{NN}}} = 5.02\,\mathrm{TeV}$. It was used also for the cross calibration of the HI jets by *pp* algorithm reconstructed jets in the *pp* collisions at $\sqrt{s_{\mathrm{NN}}} = 8\,\mathrm{TeV}$. This procedure was used to derive cross calibration factors for the HI algorithm reconstructed jets. Jet energy scale uncertainty was derived for HI jets in *pp*, p+Pb and Pb+Pb collisions.

Last chapter of this thesis presents the measurement of the jet fragmentation functions in *pp* and Pb+Pb collisions at $\sqrt{s_{\mathrm{NN}}} = 2.76\,\mathrm{TeV}$. Two sets of the fragmentation functions, $D(p_{\mathrm{T}})$ and $D(z)$ were measured for $R = 0.4$ anti-k_t jets with $100 < p_{\mathrm{T}} < 398\,\mathrm{GeV}$ in seven centrality classes of Pb+Pb collisions and in *pp* collisions. p_{T} resp. z of the tracks associated with the jets covered the range $1 < p_{\mathrm{T}} < 100\,\mathrm{GeV}$ resp. $0.01 < z < 1.0$. Distributions were corrected to the hadron level by the two dimensional Bayesian unfolding. The ratios of the fragmentation functions from Pb+Pb collisions to those in *pp* collisions were calculated differentially in centrality and jet rapidity resp. jet p_{T}. These show interesting modification where at low track p_{T} (z) ($1 \lesssim p_{\mathrm{T}} \lesssim 4\,\mathrm{GeV}$ resp. $0.01 \lesssim z \lesssim 0.04$) a strong enhancement is observed, at intermediate p_{T} (z)

($4 \lesssim p_{\mathrm{T}} \lesssim 25\,\mathrm{GeV}$ resp. $0.04 \lesssim z \lesssim 0.25$) the jet fragmentation is suppressed and at high p_{T} (z) more jet fragments is observed in Pb+Pb collisions. The size of the modification gradually decreases with increasing centrality. Behavior at high p_{T} seems to be weakly dependent on the jet rapidity where high p_{T} fragments are likely enhanced less for forward jets than for jets in central region. This was studied through the double ratio which confirms this behavior but the significance of this conclusion is limited by the statistical and systematical uncertainties of this result.

Bibliography

[1] ATLAS Collaboration. Measurement of jet fragmentation in Pb+Pb and *pp* collisions at $\sqrt{s_{\mathrm{NN}}} = 2.76$ TeV with the ATLAS detector at the LHC. *Eur. Phys. J.*, C77(6):379, 2017.

[2] Alberica Toia. Participants and spectators at the heavy-ion fireball. *CERN Cour.*, 53:31, 2013.

[3] Berndt Müller. Investigation of Hot QCD Matter: Theoretical Aspects. *Phys. Scripta*, T158:014004, 2013.

[4] Michael L. Miller, Klaus Reygers, Stephen J. Sanders, and Peter Steinberg. Glauber modeling in high energy nuclear collisions. *Ann. Rev. Nucl. Part. Sci.*, 57:205–243, 2007.

[5] H. De Vries, C. W. De Jager, and C. De Vries. Nuclear charge and magnetization density distribution parameters from elastic electron scattering. *Atom. Data Nucl. Data Tabl.*, 36:495–536, 1987.

[6] ATLAS Collaboration. The ATLAS Experiment at the CERN Large Hadron Collider. *JINST*, 3:S08003, 2008.

[7] ATLAS Collaboration. Measurement of the pseudorapidity and transverse momentum dependence of the elliptic flow of charged particles in lead-lead collisions at $\sqrt{s_{NN}} = 2.76$ tev with the atlas detector. *Phys. Lett. B*, 707:330–348, 2012.

[8] Betty Abelev et al. Centrality determination of Pb-Pb collisions at $\sqrt{s_{NN}} =$ 2.76 TeV with ALICE. *Phys. Rev.*, C88(4):044909, 2013.

[9] David J. Gross and Frank Wilczek. Ultraviolet Behavior of Nonabelian Gauge Theories. *Phys. Rev. Lett.*, 30:1343–1346, 1973.

[10] H. David Politzer. Reliable Perturbative Results for Strong Interactions? *Phys. Rev. Lett.*, 30:1346–1349, 1973.

[11] Raymond Brock et al. Handbook of perturbative QCD: Version 1.0. *Rev. Mod. Phys.*, 67:157–248, 1995.

[12] K. A. Olive et al. Review of Particle Physics. *Chin. Phys.*, C38:090001, 2014.

[13] Szabolcs Borsanyi, Zoltan Fodor, Christian Hoelbling, Sandor D Katz, Stefan Krieg, Claudia Ratti, and Kalman K. Szabo. Is there still any T_c mystery in lattice QCD? Results with physical masses in the continuum limit III. *JHEP*, 09:073, 2010.

[14] A. Bazavov et al. The chiral and deconfinement aspects of the QCD transition. *Phys. Rev.*, D85:054503, 2012.

[15] Owe Philipsen. The QCD equation of state from the lattice. *Prog. Part. Nucl. Phys.*, 70:55–107, 2013.

[16] Christian Schmidt. Lattice QCD at finite density. *PoS*, LAT2006:021, 2006.

[17] Heng-Tong Ding, Frithjof Karsch, and Swagato Mukherjee. Thermodynamics of strong-interaction matter from Lattice QCD. *Int. J. Mod. Phys.*, E24(10):1530007, 2015.

[18] Mark G. Alford, Andreas Schmitt, Krishna Rajagopal, and Thomas Schäfer. Color superconductivity in dense quark matter. *Rev. Mod. Phys.*, 80:1455–1515, 2008.

[19] Tillmann Boeckel and Jurgen Schaffner-Bielich. A little inflation at the cosmological QCD phase transition. *Phys. Rev.*, D85:103506, 2012.

[20] Arthur M. Poskanzer and S. A. Voloshin. Methods for analyzing anisotropic flow in relativistic nuclear collisions. *Phys. Rev. C*, 58:1671–1678, 1998.

[21] John Adams et al. Experimental and theoretical challenges in the search for the quark gluon plasma: The STAR collaboration's critical assessment of the evidence from RHIC collisions. *Nucl. Phys. A*, 757:102–183, 2005.

[22] K. Adcox et al. Formation of dense partonic matter in relativistic nucleus nucleus collisions at rhic: Experimental evaluation by the phenix collaboration. *Nucl. Phys. A*, 757:184–283, 2005.

[23] ATLAS Collaboration. Measurement of the azimuthal anisotropy for charged particle production in $\sqrt{s_{NN}} = 2.76$ TeV lead-lead collisions with the ATLAS detector. *Phys. Rev.*, C86:014907, 2012.

[24] K Aamodt et al. Elliptic flow of charged particles in Pb-Pb collisions at 2.76 TeV. *Phys. Rev. Lett.*, 105:252302, 2010.

[25] CMS Collaboration. Azimuthal anisotropy of charged particles at high transverse momenta in PbPb collisions at $\sqrt{s_{NN}} = 2.76$ TeV. *Phys. Rev. Lett.*, 109:022301, 2012.

[26] J. Adams et al. Evidence from d + Au measurements for final state suppression of high p(T) hadrons in Au+Au collisions at RHIC. *Phys. Rev. Lett.*, 91:072304, 2003.

[27] S. S. Adler et al. Absence of suppression in particle production at large transverse momentum in $\sqrt{s_{NN}} = 200$ GeV d+Au collisions. *Phys. Rev. Lett.*, 91:072303, 2003.

[28] ATLAS Collaboration. Measurement of charged-particle spectra in Pb+Pb collisions at $\sqrt{s_{\mathrm{NN}}} = 2.76$ TeV with the ATLAS detector at the LHC. *JHEP*, 09:050, 2015.

[29] Petr Balek. *Study of proton-proton and heavy-ion collisions with the ATLAS experiment at the LHC*. PhD thesis, Charles University, 2016.

[30] Betty Bezverkhny Abelev et al. Centrality, rapidity and transverse momentum dependence of J/ψ suppression in Pb-Pb collisions at $\sqrt{s_{\mathrm{NN}}}$=2.76 TeV. *Phys. Lett.*, B734:314–327, 2014.

[31] T. Matsui and H. Satz. J/ψ Suppression by Quark-Gluon Plasma Formation. *Phys. Lett.*, B178:416–422, 1986.

[32] C. Baglin et al. ψ' and J/ψ production in p-W, p-U and S-U interactions at 200 GeV/nucleon. *Phys. Lett.*, B345:617–621, 1995.

[33] A. Adare et al. J/ψ Production vs Centrality, Transverse Momentum, and Rapidity in Au+Au Collisions at $\sqrt{s_{NN}}$ = 200 GeV. *Phys. Rev. Lett.*, 98:232301, 2007.

[34] L. Adamczyk et al. J/ψ production at low p_T in Au+Au and Cu+Cu collisions at $\sqrt{s_{NN}}$ = 200 GeV with the STAR detector. *Phys. Rev.*, C90(2):024906, 2014.

[35] P. Braun-Munzinger and J. Stachel. (Non)thermal aspects of charmonium production and a new look at J/*psi* suppression. *Phys. Lett.*, B490:196–202, 2000.

[36] CMS Collaboration. Observation of sequential Upsilon suppression in PbPb collisions. *Phys. Rev. Lett.*, 109:222301, 2012. [Erratum: Phys. Rev. Lett.120,no.19,199903(2018)].

[37] Jaroslav Adam et al. Direct photon production in Pb-Pb collisions at $\sqrt{s_{\rm NN}}$ = 2.76 TeV. *Phys. Lett.*, B754:235–248, 2016.

[38] ATLAS Collaboration. Centrality, rapidity and transverse momentum dependence of isolated prompt photon production in lead-lead collisions at $\sqrt{s_{\rm NN}}$ = 2.76 TeV measured with the ATLAS detector. *Phys. Rev.*, C93(3):034914, 2016.

[39] CMS Collaboration. Measurement of isolated photon production in *pp* and PbPb collisions at $\sqrt{s_{NN}}$ = 2.76 TeV. *Phys. Lett.*, B710:256–277, 2012.

[40] CMS Collaboration. Study of W boson production in PbPb and *pp* collisions at $\sqrt{s_{NN}}$ = 2.76 TeV. *Phys. Lett.*, B715:66–87, 2012.

[41] ATLAS Collaboration. Measurement of Z boson Production in Pb+Pb Collisions at $\sqrt{s_{NN}}$ = 2.76 TeV with the ATLAS Detector. *Phys. Rev. Lett.*, 110(2):022301, 2013.

[42] J. D. Bjorken. Energy Loss of Energetic Partons in Quark - Gluon Plasma: Possible Extinction of High p(t) Jets in Hadron - Hadron Collisions. 1982.

[43] Miklos Gyulassy and Michael Plumer. Jet Quenching in Dense Matter. *Phys. Lett.*, B243:432–438, 1990.

[44] M. Gyulassy, M. Plumer, M. Thoma, and X. N. Wang. High P(T) probes of nuclear collisions. *Nucl. Phys.*, A538:37C–50C, 1992.

[45] R. Baier, Yuri L. Dokshitzer, S. Peigne, and D. Schiff. Induced gluon radiation in a QCD medium. *Phys. Lett.*, B345:277–286, 1995.

[46] K. Adcox et al. Suppression of hadrons with large transverse momentum in central Au+Au collisions at $\sqrt{s_{NN}}$ = 130-GeV. *Phys. Rev. Lett.*, 88:022301, 2002.

[47] C. Adler et al. Disappearance of back-to-back high p_T hadron correlations in central Au+Au collisions at $\sqrt{s_{NN}}$ = 200-GeV. *Phys. Rev. Lett.*, 90:082302, 2003.

[48] ATLAS Collaboration. Observation of a Centrality-Dependent Dijet Asymmetry in Lead-Lead Collisions at $\sqrt{s_{NN}}$ = 2.76 TeV with the ATLAS Detector at the LHC. *Phys. Rev. Lett.*, 105:252303, 2010.

[49] CMS Collaboration. Observation and studies of jet quenching in PbPb collisions at nucleon-nucleon center-of-mass energy = 2.76 TeV. *Phys. Rev. C*, 84:024906, 2011.

[50] Xin-Nian Wang and Miklos Gyulassy. Gluon shadowing and jet quenching in A + A collisions at $\sqrt{s}$= 200 GeV. *Phys. Rev. Lett.*, 68:1480–1483, 1992.

[51] R. Baier, Yuri L. Dokshitzer, Alfred H. Mueller, S. Peigne, and D. Schiff. Radiative energy loss of high-energy quarks and gluons in a finite volume quark - gluon plasma. *Nucl. Phys.*, B483:291–320, 1997.

[52] R. Baier, Yuri L. Dokshitzer, Alfred H. Mueller, S. Peigne, and D. Schiff. Radiative energy loss and p(T) broadening of high-energy partons in nuclei. *Nucl. Phys.*, B484:265–282, 1997.

[53] ATLAS Collaboration. Measurements of the Nuclear Modification Factor for Jets in Pb+Pb Collisions at $\sqrt{s_{\mathrm{NN}}}$ = 2.76 TeV with the ATLAS Detector. *Phys. Rev. Lett.*, 114:072302, 2015.

[54] CMS Collaboration. Measurement of inclusive jet cross sections in *pp* and PbPb collisions at $\sqrt{s_{NN}}$ = 2.76 TeV. *Phys. Rev.*, C96(1):015202, 2017.

[55] ATLAS Collaboration. Measurement of the production of neighbouring jets in lead–lead collisions at $\sqrt{s_{\mathrm{NN}}}$ = 2.76 TeV with the ATLAS detector. *Phys. Lett.*, B751:376–395, 2015.

[56] Martin Rybář. *Study of jets in p+p and Pb+Pb collisions at LHC.* PhD thesis, Charles University, 2015.

[57] Lyndon Evans and Philip Bryant. LHC Machine. *JINST*, 3:S08001, 2008.

[58] CERN. Lhc report: 100 inverse femtobarns and counting..., 2017. https://home.cern/cern-people/updates/2017/10/lhc-report-100-inverse-femtobarns-and-counting.

[59] Peter Jenni and Marzio Nessi. ATLAS Heavy-ion Physics. Technical Report CERN-LHCC-2004-009. LHCC-I-013, CERN, Geneva, Mar 2004.

[60] Marco A. L. Leite. Performance of the ATLAS Zero Degree Calorimeter. In *Proceedings, 2013 IEEE Nuclear Science Symposium and Medical Imaging Conference (NSS/MIC 2013): Seoul, Korea, October 26-November 2, 2013*, 2013.

[61] Morad Aaboud et al. Measurement of jet p_{T} correlations in Pb+Pb and pp collisions at $\sqrt{s_{\mathrm{NN}}} = 2.76$ TeV with the ATLAS detector. *Phys. Lett.*, B774:379–402, 2017.

[62] ATLAS Collaboration. Measurement of inclusive jet charged-particle fragmentation functions in Pb+Pb collisions at $\sqrt{s_{NN}} = 2.76$ TeV with the ATLAS detector. *Phys. Lett. B*, 739:320–342, 2014.

[63] ATLAS Collaboration. Centrality and rapidity dependence of inclusive jet production in $\sqrt{s_{\mathrm{NN}}} = 5.02$ TeV proton-lead collisions with the ATLAS detector. *Phys. Lett.*, B748:392–413, 2015.

[64] ATLAS Collaboration. Measurement of the Azimuthal Angle Dependence of Inclusive Jet Yields in Pb+Pb Collisions at $\sqrt{s_{NN}} = 2.76$ TeV with the ATLAS detector. *Phys. Rev. Lett.*, 111(15):152301, 2013.

[65] Torbjorn Sjostrand, Stephen Mrenna, and Peter Z. Skands. PYTHIA 6.4 Physics and Manual. *JHEP*, 05:026, 2006.

[66] ATLAS Collaboration. Jet energy measurement with the ATLAS detector in proton-proton collisions at $\sqrt{s} = 7$ TeV. *Eur. Phys. J. C*, 73:2304, 2013.

[67] ATLAS Collaboration. Jet energy measurement and its systematic uncertainty in proton-proton collisions at $\sqrt{s} = 7$ TeV with the ATLAS detector. *Eur. Phys. J.*, C75:17, 2015.

[68] ATLAS Collaboration. *Jet energy scale and its uncertainty for jets reconstructed using the ATLAS heavy ion jet algorithm.* ATLAS-CONF-2015-016.

[69] ATLAS Collaboration. Measurement of the muon reconstruction performance of the ATLAS detector using 2011 and 2012 LHC proton–proton collision data. *Eur. Phys. J.*, C74(11):3130, 2014.

[70] I. P. Lokhtin and A. M. Snigirev. A Model of jet quenching in ultrarelativistic heavy ion collisions and high-p(T) hadron spectra at RHIC. *Eur. Phys. J.*, C45:211–217, 2006.

[71] Radim Slovák. *Study of jet fragmentation and inclusive jet production in heavy-ion collisions with the ATLAS experiment.* PhD thesis, Charles University, 2017.

[72] Tim Adye. Unfolding algorithms and tests using RooUnfold. pages 313–318, 2011.

[73] G. D'Agostini. A Multidimensional unfolding method based on Bayes' theorem. *Nucl. Instrum. Meth. A*, 362:487–498, 1995.

[74] G. D'Agostini. Improved iterative Bayesian unfolding. In *Alliance Workshop on Unfolding and Data Correction Hamburg, Germany, May 27-28, 2010*, 2010.

List of Figures

List of Tables